Departamento de Física Teórica

Universidad Autónoma de Madrid

SIMULATING COSMOLOGIES BEYOND THE STANDARD MODEL

Memoria de Tesis Doctoral presentada por

Edoardo Carlesi

para optar al título de Doctor en Ciencias Físicas

Trabajo supervisado por el Doctor

Alexander Knebe, Departamento de Física Teórica, UAM

13/05/2014

Statement

This dissertation is presented as a collection of articles published during the years of my PhD, from November 2010 to March 2014. These works have been written in collaboration with researchers from many other institutions, to whom I am thankful for their contribution. The details of these publications are reported below for convenience.

Edoardo Carlesi
Madrid, 11th February, 2014

1. **High-z massive clusters and Vector Dark Energy.**
   E. Carlesi, A. Knebe, G. Yepes, S. Gottlöber, A. Maroto, J. Beltran.
   MNRAS 418, 2715, (2011) arXiv:1108.4173

2. **N-body simulations of a Vector Dark Energy model.**
   E. Carlesi, A. Knebe, G. Yepes, S. Gottlöber, A. Maroto, J. Beltran.
   MNRAS 425, 669, (2012) arXiv:1205.1695

3. **Hydrodynamical simulations of coupled and uncoupled quintessence models I: Halo properties and the cosmic web.**
   E. Carlesi, A. Knebe, G.F. Lewis, S. Wales, G. Yepes.
   Accepted for publication in MNRAS, (2014) arXiv:1401.5005

4. **Hydrodynamical simulations of coupled and uncoupled quintessence models II: Galaxy clusters.**
   E. Carlesi, A. Knebe, G.F. Lewis, G. Yepes.
   Accepted for publication in MNRAS, (2014) arXiv:1401.5326

STATEMENT

Contents

Resumen y Conclusiones

Motivación

En los últimos quince años, ha habido un cambio de paradigma en la cosmología debido a la influencia de un conjunto de nuevas observaciones. El mejoramiento radical de la calidad de los datos ha permitido medir numerosas propiedades del Universo con una precisión sin precedentes, llevando a la formulación del modelo cosmológico estándar. Este puede explicar con éxito la geometria plana y la aceleración en la velocidad de expansión del Universo. Sin embargo, para hacerlo, se requiere que $\approx 95\%$ de la densidad de materia y energía sea debido a dos sustancias desconocidas, llamadas *Energ ía Oscura* (EO) y *Materia Oscura* (MO). En particular, la EO es responsable de la aceleración de la tasa de expansión del Universo: para hacerlo, tiene que ser caracterizada por una ecuación de estado no estándar $P = \omega\rho$, donde el parámetro tiene un valor negativo.

La forma más simple de explicar este fenómeno consiste en asumir que todo el espacio esté permeado con una *constante cosmológica* Λ, una forma de energía de presión negativa que contrarresta la atracción gravitatoria. Actualmente, es este el ingrediente clave del modelo estandár, que por esta razón se llama también Λ Cold Dark Matter (ΛCDM, Λ Materia Oscura Fra). A pesar de poder explicar un gran número de observaciones distintas, ΛCDM está afectado por un conjunto de problemas. Si hipotetizamos que Λ sea la energía de punto cero de un campo cuántico fundamental, necesitamos un ajuste de unas decenas de ordenes de magnitud para asegurar que la teória sea consistente con los datos observacionales. Otra dificultad de ΛCDMes el llamado *problema de la coincidencia cósmica*, que se refiere a la dificultad de explicar de forma natural el hecho que en el tiempo presente las densidades de materia y energía oscura tienen aproximadamente el mismo valor, aunque su evolución has sido completamente distinta durante la mayor parte de la historia del Universo. Encima de estos problemas teóricos, que ponen en duda la *naturalidad* de ΛCDM, hay también un conjunto de observaciones que parecen contradecir a sus predicciones. En particular, ΛCDM predice un número demasiado pequeño de cúmulos de galaxias de alto desplazamiento al rojo z y un número demasiado grande de satélites en galaxias del tipo *Vía Láctea*. Aunque estos problemas podrían resolverse revisando el paradigma ΛCDM (por ejemplo cambiando algunos parámetros del modelo), es igualmente importante no subestimarlos ni ignorar que sean unas posibles señales de nueva física. Por lo tanto, es fundamental estudiar alternativas a ΛCDM y obtener predicciones que puedan falsar o eventualmente favorecer estos modelos. Esta es la motivación principal del trabajo que voy a presentar aquí, donde estudié el impacto de formas distintas de EO y MO sobre la formación de estructuras en el Universo. Mi objetivo ha sido de comparar un conjunto de posibles alternativas a ΛCDMutilizando simulaciones

hidrodinámicas de N cuerpos y identificar así varias pruebas que podrían excluir los modelos no estándar. En las secciones siguientes presentaré brevemente las técnicas utilizadas, los modelos investigados y los resultados más importantes que obtuve.

El desafío numérico

Las simulaciones cosmológicas son un instrumento muy poderoso que permite la obtención de resultados en el régimen profundamente no lineal, que no es accesible utilizando los métodos analíticos estandár. Sin embargo, siendo la mayoría de los códigos públicos diseñados para ΛCDM, necesitamos implementar un conjunto de modificaciones especiales para el caso de un modelo no estandár. Así, la primera tarea que tuve que llevar a cabo fue la de adaptar y extender los códigos existentes para simular los efectos no lineales que surgen en estas cosmologías.

Para ejecutar una simulación cosmológica de N cuerpos normalmente se siguen los siguientes pasos:

I) generar condiciones iniciales (CI) adecuadas, es decir asignar a cada partícula su posición y una velocidad utilizando el espectro de potencia y el factor de crecimiento correctos

II) evolucionar las partículas con un código de N cuerpos y hidrodínamica (en los casos en los que se incluyan bariones)

III) analizar el resultado de la simulación con un halo finder (buscador de halos)

IV) utilizar herramienta de post-procesamiento para computar las cantidades observacionales relevantes a partir de los catálogos de halos y de las instantáneas de los resultados de la simulación

En muchos casos, para los puntos I, II y IV la modificación necesaria no depende de los detalles del modelo, así que por ejemplo el generador de CI puede utilizar cualquier espectro de potencia y factor de crecimiento. Sin embargo, el caso de los códigos de N cuerpos es mas complicado porque suele depender del modelo especifico que hay que simular. En el caso de Energía Oscura Vectorial y Quintesencia no interactuante este procedimiento se puede cumplir de forma relativamente simple, tan sólo modificando a la tasa de expansión del Universo. Para modelos de EO-MO interactuantes, hay que tener en cuenta más características que afectan los algoritmos de computación de la fuerza gravitacional, que están en el corazón del código.

En mi trabajo he implementado el procedimiento de Baldi et al. (2010) en dos librerías añadidas al código público `Gadget-2`, que utiliza un algoritmo Tree-PM para computar la gravedad y un esquema de Smoothed Particle Hydrodynamics para las fuerzas hidrodínamicas (Springel, 2005). La primera librería se ocupa de computar el factor de expansión $a(t)$ para todo tipo de cosmología. La segunda lee e interpola las variables relacionadas a la fuerza adicional como la variación de masa para las partículas de MO $m(z)$, el campo escalar de quintesencia ϕ y su derivada $\dot{\phi}$.

Energía Oscura Vectorial

El modelo de Energía Oscura Vectorial (EOV) que estudié fue propuesto por Jiménez & Maroto (2008), ahí la componente temporal A_0 de un 4-vector A_μ juega el papel de EO. Sus ventajas están debidas a que no requiere ningún potencial, ningún parámetro adicional ni ningún ajuste fino de las condiciones iniciales del campo vectorial, que explica naturalmente la aceleración del Universo. Además, este modelo de EOV es compatible con los datos observacionales de Supernovae de tipo Ia y de la Radiación de Fondo (Jiménez & Maroto, 2008; Beltrán Jiménez et al., 2009), aunque los valores de best-fit de los parámetros cosmológicos se diferencian mucho de los de ΛCDM, siendo la ecuación de estado $\omega(z = 0) = -3.53$, el $\sigma_8 = 0.83$ y el $\Omega_m = 0.388$. Diseñé las simulaciones de tal forma que permitían un estudio adecuado de las propriedades de las estructuras a grande escala y de los halos de MO, y poder así obtener unas predicciones precisas para la EOV en estos regímenes. Adicionalmente, para poder separar los efectos de los parámetros del impacto de la expansión cósmica $a(t)$, ejecuté unas simulaciones adicionales llamadas ΛCDM-eov, es decir un modelo ΛCDM estándar con los parametros Ω_m y σ_8 del EOV.

Las simulaciones las ejecuté utilizando la misma semilla aleatoria para el generador de CI, para poder comparar de forma consistente los tres modelos (ΛCDM, ΛCDM-eov y EOV) en dos cajas distintas (de $500h^{-1}$ Mpc y $1h^{-1}$Gpc) con un total de 512^3 partículas de MO en cada simulación, para permitir el estudio de las propiedades de los halos en la primera y las de los cúmulos más masivos en la segunda.

Gracias a estas simulaciones, pude obtener los siguientes resultados:

I) Calculé la probabilidad de hallar un cúmulo masivo para $z > 1$, demostrando que ese tipo de objectos son hasta diez veces más probables en EOV que en ΛCDM. Esto es debido sobre todo al parámetro Ω_m y permite reducir el desacuerdo del modelo estandár con los datos observacionales.

II) Pude caracterizar el modelo EOV por su factor de crecimiento $\gamma(z)$, que resulta ser muy distinto de los casos ΛCDM y ΛCDM-vde. Esta cantidad entonces es un trazador optimo del modelo cosmológico y puede ser una prueba poderosa a la hora de falsarlo.

III) Demonstré como las funciones de masa de los halos son mayores en EOV a todo z, debido a los incrementos en σ_8 y Ω_m. De un lado, este resultado favorece la probabilidad de hallar cúmulos de alto z, pero de otro lado podría chocar con las observaciones de $z \approx 0$, para las cuales se observa un número menor de estructuras masivas de lo previsto por EOV.

IV) Los halos de MO en EOV tienen a una concentración media mayor que ΛCDM, un efecto que confirma los resultados de (Dolag et al., 2004; Bartelmann et al., 2006) para otros modelos de EO. Este efecto se debe a la época de formación de las estructuras, que en EO dinámica empieza antes que en ΛCDM.

V) Otras propiedades de los halos, como el parámetro de spin λ, los perfiles de densidad, la triaxialidad y la forma quedan prácticamente no afectados por EOV. La razón es que, una vez que las estructuras empiecen a colapsar ya no están afectadas por la expansión cósmica y siguen las mismas leyes de la gravedad.

Todos estos resultados fueron publicados en dos artículos (Carlesi et al., 2011, 2012), que están incluidos en esta tesis.

Energá Oscura de Campo Escalar

Los modelos de campo escalar de EO, también llamados modelos de Quintesencia, fueron elaborados como una posible alternativa al ΛCDM (Wetterich, 1995; Zlatev et al., 1999; Amendola, 2000). Los campos escalares aparecen en muchas teorías de física de partículas y por esto es interesante investigar su papel a escala cósmica, como un candidato viable para la EO. El enfoque de mi análisis fue centrado en dos modelos de Quintesencia, acoplada y no acoplada, los dos con un potencial de auto-interacción de tipo Ratra-Peebels (Ratra & Peebles, 1988), cuyos parámetros libres fueron elegidos para asegurar la compatibilidad con las observaciones de WMAP7 (**?**). En la simulaciones incluí también bariones, que están afectados por fuerzas de tipo hidrodinámico. Para todos los modelos tomé los mismos valores σ_8 y Ω_m obtenidos para ΛCDM utilizando los datos de WMAP7 a $z = 0$, de esta forma es posible conectar las propriedades observacionales con la dinámica subyacente minimizando el impacto de los parámetros cosmológicos. En total, ejecuté cinco simulaciones, con la misma fase para las fluctuaciones de las perturbaciones iniciales en las CI, el mismo tamaño de la caja $L = 250h^{-1}\,\mathrm{Mpc}$ y un total de 2×1024^3 particulas de gas y MO. Esta configuración me permitió estudiar las propriedades de gran escala al mismo tiempo que la estructura interior de los halos de MO y el impacto de la interacción en el sector oscuro sobre las propriedades de la componente barionica. Entre los resultados más importantes que obtuve hay que mencionar:

I) El descubrimiento de una relación entre el parámetro λ de spin de los halos de MO y la interacción MO-EO. Analizando una serie de conjuntos de halos, pude determinar que una quinta fuerza está relacionada con un valor medio de λ hasta un 10% más alto.

II) La cuantificación de la relación entre masa y concentración para halos de masa entre $10^{12} - 10^{14}h^{-1}\mathrm{M}_\odot$, en cada cosmología.

III) Luego de un análisis detallado de la estructura de la red cósmica, el primer resultado fue que la estructura de la red misma no está relacionada con la cosmología, siendo muy parecida en cada modelo. A pesar de esto, hallé que hay una importante correlación entre el contenido de los vacíos y Quintesencia acoplada. De hecho, comparando con ΛCDM se observa que los modelos de EO acoplados poseen un número substancialmente menor (alrededor de un 20% menos) de halos de MO en las regiones de baja densidad.

IV) Al analizar los perfiles de densidad de gas en cúmulos de galaxias, encontré una reducción importante ($\approx 7\%$(de las fracciones de bariones en las regiones centrales de los cúmulos, debida al tiempo relativamente mayor en el cual las partículas de gas caen hacia el centro respecto a las de MO, que están afectadas por una interacción adicional. Los perfiles de presión muestran una dependencia aún mayor del modelo cosmológico, como su valor en las regiones exteriores de los cúmulos desvía hasta un 20% de ΛCDM. Sin embargo, el modelo para los perfiles de densidad de gas de Mroczkowski et al. (2009) y el de Leccardi & Molendi (2008) para los perfiles de temperatura siguen valiendo para todo modelo.

V) A través de la correlación cruzada de estructuras individuales en cosmologías pude comprobar los resultados teóricos de Abdalla et al. (2010) sobre la conexión entre equilibrio viral ordinario y una fuerza adicional en el sector oscuro.

VI) Los perfiles de densidad de MO en los cúmulos pueden ser adecuadamente descritos por un perfil NFW, de acuerdo con los resultados de Baldi & Pettorino (2011) y Li & Barrow (2011). Las relaciónes usuales de masa-temperatura tampoco se ven afectadas por la cosmología.

Todos estos resultados aparecieron recientemente en dos artículos (Carlesi et al., 2014, I & II), que están incluidos en esta tesis.

Conclusiones

En este trabajo estudié el impacto de distintas formas de EO en la formación de estructuras, utilizando la técnica de simulaciones de N-cuerpos. Para conseguirlo, tuve que modificar, extender y desarrollar una serie de herramientas numéricas que me permitieron efectuar un análisis detallado de cada cosmología, para definir posibles pruebas observacionales que puedan falsarlas o favorecerlas. Después de haber diseñado y ejecutado un conjunto de simulaciones pude obtener una serie de nuevos resultados que caracterizan las propriedades de las estructuras y su formación en unos modelos cosmológicos no estándar. En particular, demonstré como estos pueden ser distinguidos por ΛCDM gracias a un conjunto de rasgos, proporcionando también estimaciones numéricas para cuantificar el tamaño de diferencias con él. Cabe recalcar que estos resultados será útil en la próxima década, cuando una grande cantidad de observaciones de alta precisión comprobará los fundamentos de las teórias cosmológicas en un nivel más profundo. Entonces, necesitaremos un conocimiento mejor de las alternativas al ΛCDM, para saber si los nuevos datos nos llevarán hacia una revisión o un relevo del paradigma estándar.

References

Abdalla E., Abramo L. R., de Souza J. C. C., 2010, Phys. Rev. D, 82, 023508

Amendola L., 2000, Phys. Rev. D, 62, 043511

Baldi M., Pettorino V., 2011, MNRAS, 412, L1

Baldi M., Pettorino V., Robbers G., Springel V., 2010, MNRAS, 403, 1684

Bartelmann M., Doran M., Wetterich C., 2006, A&A, 454, 27

Beltrán Jiménez J., Lazkoz R., Maroto A. L., 2009, Phys. Rev. D, 80, 023004

Carlesi E., Knebe A., Lewis G. F., Wales S., Yepes G., 2014

Carlesi E., Knebe A., Yepes G., Gottlöber S., Jiménez J. B., Maroto A. L., 2011, MNRAS, 418, 2715

References

Carlesi E., Knebe A., Yepes G., Gottlöber S., Jiménez J. B., Maroto A. L., 2012, MNRAS, 424, 699

Dolag K., Bartelmann M., Moscardini L., Perrotta F., Baccigalupi C., Meneghetti M., Tormen G., 2004, Modern Physics Letters A, 19, 1079

Jiménez J. B., Maroto A. L., 2008, Phys. Rev. D, 78, 063005

Leccardi A., Molendi S., 2008, A&A, 486, 359

Li B., Barrow J. D., 2011, MNRAS, 413, 262

Macciò A. V., Quercellini C., Mainini R., Amendola L., Bonometto S. A., 2004, Phys. Rev. D, 69, 123516

Mroczkowski T., et al., 2009, ApJ, 694, 1034

Navarro J. F., Frenk C. S., White S. D. M., 1996, ApJ, 462, 563

Pettorino V., Amendola L., Baccigalupi C., Quercellini C., 2012, Phys. Rev. D, 86, 103507

Ratra B., Peebles P. J. E., 1988, Phys. Rev. D, 37, 3406

Springel V., 2005, MNRAS, 364, 1105

Wetterich C., 1995, A&A, 301, 321

Zlatev I., Wang L., Steinhardt P. J., 1999, Physical Review Letters, 82, 896

Summary and Conclusions

Motivation

In the last fifteen years, cosmology has gone through a major paradigm shift under the influence of a broad ensemble of new observations. The dramatic improvement of the quality of the data taken has allowed to measure several properties of the universe (such as its spatial geometry and its matter content) with an unprecedented degree of accuracy, leading to the formulation of the so-called standard cosmological model. This successfully accounts for the fact that the Universe we live in is spatially flat and expanding at an accelerating speed. However, to do this, it requires that 95% of its matter-energy content must be due to two mysterious substances called *Dark Energy* (DE) and *Dark Matter* (DM).

In particular, the former type of energy is the main driver of the observed acceleration in the expansion of the Universe: To do so, it must be characterized by a non standard equation of state $P = \omega\rho$ with a negative value for the ω parameter. The simplest way to explain this is assuming that the space is permeated by a *cosmological constant* Λ, an ubiquitous form of energy which exerts a negative pressure counteracting the gravitational pull. This is a key ingredient to what is today regarded as the standard model, the Λ Cold Dark Matter (ΛCDM) model. While on the one hand the ΛCDM framework accounts for a very large number of diverse observations, it is nonetheless plagued by a series of problems. In fact, if we believe the cosmological constant to be the zero point energy of some fundamental quantum field, we end up requiring a fine-tuning of several tens of orders of magnitude (depending on the energy scale we choose to be fundamental in our theory) to ensure consistency with the observational data. Another issue we encounter is the so called *coincidence problem*, that is, the difficulty to explain in a natural way the fact that today's matter and DE densities are of roughly the same order of magnitude, although they are characterized by a completely different evolution throughout most of the history of the Universe.

On top of these theoretical issues, that challenge the *naturalness* of ΛCDM, there is also a series of observational data which seems to be at odds with its predictions. In particular, ΛCDM seems to under-predict the abundances of massive galaxy clusters at high redshift and over-predict the number of satellite galaxies in Milky Way-sized haloes. On the one hand, while it is true that these issues might be solved by minor revisions to the ΛCDM paradigm (e.g. using different values for the cosmological parameters or improving the simulation techniques for baryonic processes) it is also important not to overlook them and hence neglect possible signs of new physics.

It is thus of primary importance to study alternatives to ΛCDM and obtain predictions for observables which may rule them out or provide evidence in their support. This is the

main motive behind the work that I am presenting here, in which I have studied the impact of different forms of DE and DM on the formation of structures in the Universe. My goal has been to compare a series of viable alternatives to ΛCDM via N-body and hydrodynamical simulations, and identify in this way a series of observational probes which might provide evidence or disprove those non-standard scenarios. In the following subsections I will present the techniques I have used, the models I have investigated and the main results that I have obtained.

The numerical implementation

Cosmological simulations are a very powerful tool that allow to draw results from the deeply non-linear regime, unaccessible to standard analytical tools. However, as most of the publicly available codes are tailored for ΛCDM simulations, for alternative cosmologies we need ad-hoc modifications that require a careful implementation and testing to avoid spurious numerical influences on the output. Hence, the first task of my work has been to adapt and devise new codes and numerical techniques in order to properly account for the non-linear scale effects arising in these cosmologies.

The standard simulation pipeline goes as follows:

I) generate proper initial conditions (IC), i.e. assign the particles' positions and velocities (and temperatures for baryons) according to the matter power spectrum and growth factors

II) evolve the particles with an N-body (and hydro) code

III) analyze the output with an halo finder

IV) use post processing tools on the halo catalogs and the simulation's snapshots to compute physical quantities and observables

In many cases, steps I, III and IV require the same kind of modifications regardless of the details of the model, so for example the IC generator should be able to use arbitrary power spectra and growth factors and the halo finder should take into account any $\rho_c(z)$, the critical density of the universe, which is needed to consistently define the halo edges. However, N-body codes' modifications are generally dependent on the kind of model which needs to be simulated. While in the case of Vector Dark Energy and non-interacting Quintessence this can be relatively easily done modifying the background expansion rate, interacting DE-DM models introduce additional layers of complexity that affect the gravitational solver of the code, which constitutes its very heart.

Following closely the recipe of Baldi et al. (2010), I have implemented the required modifications into two libraries added to the publicly available `GADGET-2` software, which uses a Tree-PM algorithm to compute Newtonian gravity and an Smoothed Particle Hydrodynamics (SPH) entropy conserving scheme for the gas particles (Springel, 2005).

The first one, which is responsible for the computation of $a(t)$ (the expansion factor), is common to all the non-standard implementations. The second one reads and interpolates the additional coupling-related quantities $m(z)$ (the DM particles' mass), ϕ (the quintessence scalar field) and $\dot{\phi}$ while it is also responsible for integrating the cosmic friction term of that

enters the modified Euler equation. Below I will discuss some details of my implementation of the non-standard features.

Background expansion

The expansion history of the universe directly affects the growth of structures counteracting the otherwise dominant gravitational pull. Therefore, different cosmological models may lead to substantial modifications and leave large imprints via their Hubble expansion.

While in the vanilla version of `GADGET2` $H(z)$ is computed on-the-fly solving the Friedmann equations, the computation of the Hubble parameter for alternative models is not as straightforward. Thus, for a better performance, I have separately pre-computed the expansion history for each non-standard model and then loaded the results into a spline which can be interpolated at every step to obtain the appropriate $a(t)$.

Fifth force

I have previously mentioned how DE interactions introduce a series of important modifications that need to be taken into account in the Newtonian regime relevant when dealing with N-body simulations.

As long as the mass of the scalar field m_ϕ is negligible (as in our case), it is possible to approximate the effect of DE as a gravitational-like, long range fifth force acting on cold DM particles only. This requires the code to be modified as follows:

Mass variation The variation of the DM particles' mass is obtained at every timestep interpolating from a pre-computed table. Taking m_0 as a reference mass at $z = 0$, where it takes exactly the same value as in ΛCDM, the redshift-dependence is calculated taking the ratio $\Delta m(z) = \frac{\rho_{cDE}(z)}{\rho_{\Lambda CDM}(z)} - 1$, which gives the deviation from the standard scaling of matter energy density. Of course, $\rho_{\Lambda CDM}$ and ρ_{cDE} need to be normalized to the same value at $z = 0$. The effective mass of DM particles is then given by $m(z) = m_0(1 + \Delta m(z))$,, so that every z we can get the correct m for cDE simply interpolating $\Delta(z)$.

Particle momenta The momenta of the particles have to be modified according to the new Euler equation, since this term introduces a velocity dependent force. Thus, it is necessary to add to the `GADGET-2` canonical momentum a *friction term* which must also depend on the particle type. Interestingly, this term adds to the particle velocity, as it acts like an additional source of acceleration.

Enhanced gravitational attraction To take the enhanced gravitational attraction into account – which affects cold dark matter only – I hadto modify the usual force computation procedure, that normally involves *all* matter types. For the tree part of the algorithm, this means that the nodes must now store additional information on DM particles only, i.e. center of mass, velocity and total mass. In our particular implementation, where the additional DE mediated interaction is much smaller than the gravitational one, it was not necessary to modify the standard opening criteria for the tree nodes.

When considering the PM part, *only* DM particles have to be assigned to the mesh before solving the Green function for the DE potential via FFT. In our case, this potential has the

same functional form of the gravitational one, while the effective Newtonian constant on DM particles is given by $\tilde{G}_N = G_N(1+\beta^2)$, where β is the coupling parameter.

Vector Dark Energy

The Vector Dark Energy (VDE) model I have studied was proposed by Jiménez & Maroto (2008). There, the role of DE is played by the time component A_0 of a 4-vector A_μ whose A_i components rapidly decay in the early universe and are thus negligible on cosmological scales. The advantage of this model is that it requires no potential, no additional parameters and no fine tuning of the initial conditions, as the evolution of such a field naturally accounts for the late time acceleration of the Universe. The model can account for Cosmic Microwave Background (CMB) and Type Ia Supernovae data (Jiménez & Maroto, 2008; Beltrán Jiménez et al., 2009), however predicting best fit values very different from ΛCDM, such as an equation of state $\omega(z=0) = -3.53$, a $\sigma_8 = 0.83$ and an $\Omega_m = 0.388$.

I have designed the simulations for this model in order to be able to study the properties of Large Scale Structures (LSS) and DM haloes and hence devise predictions for VDE in these regimes. To disentangle the effects of the different parameters from the impact of the cosmological expansion rate $a(t)$, I have ran an additional simulation labeled ΛCDM-vde, i.e. a standard ΛCDM model implementing VDE values for Ω_m and σ_8. The simulations were run using the same initial random seed for the IC generation, to allow for a consistent cross comparison of the three models (ΛCDM, VDE and ΛCDM-vde); using two different boxes (of $500h^{-1}$ Mpc and $1h^{-1}$Gpc) and a total of 512^3 DM particles in each simulation, so that we could study halo properties using the former box and extreme object statistics with the latter.

Using these simulation, I have been able to deliver the following series of results:

I) I have computed the probabilities of finding massive clusters at $z > 1$, finding that in the VDE these kind of objects are up to ten times more likely than in ΛCDM. This is mostly due to the larger Ω_m, and reduces the discrepancy with observational data.

II) I have been able to characterize VDE by its peculiar growth index $\gamma(z)$, which differs substantially from both ΛCDM and ΛCDM-vde. This makes of this particular observable a very good tracer of the underlying cosmological model and a powerful probe for model selection.

III) I have shown how halo mass functions are strongly enhanced in VDE at all redshifts, mainly as a result of the cosmological parameters. While this enhances the probability of finding massive clusters at high redshift, it may be at odds with current observations of the $z \approx 0$ Universe, for which it predicts a much higher number of large structures.

IV) Dark matter haloes in VDE are characterized by larger concentrations, as known already for other DE models (Dolag et al., 2004; Bartelmann et al., 2006). This is due to the time of structure formation, that in dynamical DE cosmologies usually takes place before ΛCDM.

V) Other internal properties of DM haloes, such as spin parameter λ, density profiles, triaxiality and shape remain largely unaffected by VDE. In particular, DM densities inside

VDE haloes can be accurately fitted by a Navarro-Frenk-White (NFW) profile Navarro et al. (1996). This can be explained by the fact that, as structures collapse and detach from the background expansion, they are governed by gravitational processes only, which are the same in all the cosmological models.

All of these results have been published in two papers (Carlesi et al., 2011, 2012) that are included in the present dissertation.

Scalar Field Dark Energy

Scalar Field Dark Energy models, or Quintessence models, have long been proposed as a viable alternative to ΛCDM (Wetterich, 1995; Zlatev et al., 1999; Amendola, 2000). Scalar fields appear in many fundamental particle physics theories and thus it is justified to explore their role on a cosmic scale, as natural candidates for DE. In my analysis I have taken into account two classes of Quintessence models, coupled (cDE) and uncoupled (uDE) DE, both based on a Ratra-Peebles self interaction potential (Ratra & Peebles, 1988), whose free parameters have been chosen according to ensure compatibility with WMAP7 CMB observations (Pettorino et al., 2012). The simulations have been run also including also baryonic particles, which are affected by hydrodynamical forces. I have normalized the models at the same WMAP7 ΛCDM $z = 0$ best fit values for σ_8 and Ω_m to be able to link their observational properties to the underlying dynamics, minimizing the impact of the cosmological parameters. I have set up a total of five simulations, with the same initial phase of the density fluctuations in the IC, same box size of $L = 250h^{-1}\,\mathrm{Mpc}$ and 2×1024^3 gas and DM particles. These settings allowed me to study LSS properties, the internal structure of DM haloes and the impact of an interacting dark sector on the gas component. Among the most important results I have obtained I mention the following:

I) The discovery of a relation between the DM halo spin parameter λ and DE-DM interaction. Analyzing different halo samples, I have determined that a dark fifth force is positively correlated with an average larger value of λ, up to 10%.

II) Determining the values of the concentration-mass relation in the range $10^{12} - 10^{14} h^{-1}\mathrm{M}_\odot$ for the different cosmologies.

III) A detailed analysis of the structure of the cosmic web. The first result is that the web in itself is not correlated to the cosmology, since volume and mass filling fractions for the different kinds of environments are approximately the same for all the models. However, I discovered a strong, positive correlation between the content of voids and coupled quintessence. In fact, compared to ΛCDM and uncoupled quintessence, cDE models have a substantially smaller ($\approx 20\%$) number of DM haloes in underdense regions. This is due to the draining of matter from voids and sheets towards overdensities, which is enhanced by the fifth force.

IV) Computation of gas profiles in galaxy clusters. I have found a significant reduction ($\approx 7\%$) of baryon fractions towards the center of the cluster, associated to a slower relative infalling time of gas particles with respect to the DM ones, which are subject to an additional gravitation-like pull. Pressure profiles show an even larger dependence

on the cosmological model, as their value in the outskirts of the cluster deviates up to 20% from ΛCDM in the strongest coupled case. On the other hand, the Mroczkowski et al. (2009) model for gas density profiles and the Leccardi & Molendi (2008) model for temperature profiles can be both accurately fitted by all models.

V) Cross-correlating individual structures across different cosmologies I have been able to prove the analytical results of Abdalla et al. (2010) on the link between the deviation from ordinary virial equilibrium and fifth force interactions in the dark sector. Moreover, I have been able to confirm the results for the correlation of spin parameter, showing that also galaxy clusters in cDE models are expected to have, on the average, an higher λ than uncoupled models.

VI) Dark matter profiles in clusters can be accurately fitted by an NFW profile, in line with the results of Baldi & Pettorino (2011) and Li & Barrow (2011), but in contrast with the early findings of Macciò et al. (2004). Also the usual mass-temperature relations (regardless of the temperature definition) are not affected by the cosmology.

These results have recently appeared in two publications (Carlesi et al., 2014, I & II) which are also part of this dissertation.

Conclusions

In this work I have studied the impact of different DE models on structure formation using N-body simulations. To do this, I modified, extended and developed a series of numerical tools that enabled me to carry a detailed analysis of these cosmologies, with the aim of identifying experimental observables that may disprove or provide evidence in favour of a given model. I have extensively worked on how to set up a simulation pipeline and how to extract relevant informations from the output. In the end, I have been able to deliver a series of new results which characterize the pattern and properties of structures and structures formation in various non-standard cosmological models. I have shown how these can be characterized by a series of features which might distinguish them from the standard paradigm, providing numerical estimates that relate the size of the discrepancies to each particular model. Indeed, this knowledge will prove useful in the next decade, when a large number of high-precision observations will probe the foundations of cosmological theories to a deeper level. Then, a better understanding of alternatives to ΛCDM will be required, to see whether the new data will be pointing at a revision or a replacement of the standard paradigm.

References

Abdalla E., Abramo L. R., de Souza J. C. C., 2010, Phys. Rev. D, 82, 023508

Amendola L., 2000, Phys. Rev. D, 62, 043511

Baldi M., Pettorino V., 2011, MNRAS, 412, L1

Baldi M., Pettorino V., Robbers G., Springel V., 2010, MNRAS, 403, 1684

Bartelmann M., Doran M., Wetterich C., 2006, A&A, 454, 27

Beltrán Jiménez J., Lazkoz R., Maroto A. L., 2009, Phys. Rev. D, 80, 023004

Carlesi E., Knebe A., Lewis G. F., Wales S., Yepes G., 2014

Carlesi E., Knebe A., Yepes G., Gottlöber S., Jiménez J. B., Maroto A. L., 2011, MNRAS, 418, 2715

Carlesi E., Knebe A., Yepes G., Gottlöber S., Jiménez J. B., Maroto A. L., 2012, MNRAS, 424, 699

Dolag K., Bartelmann M., Moscardini L., Perrotta F., Baccigalupi C., Meneghetti M., Tormen G., 2004, Modern Physics Letters A, 19, 1079

Jiménez J. B., Maroto A. L., 2008, Phys. Rev. D, 78, 063005

Leccardi A., Molendi S., 2008, A&A, 486, 359

Li B., Barrow J. D., 2011, MNRAS, 413, 262

Macciò A. V., Quercellini C., Mainini R., Amendola L., Bonometto S. A., 2004, Phys. Rev. D, 69, 123516

Mroczkowski T., et al., 2009, ApJ, 694, 1034

Navarro J. F., Frenk C. S., White S. D. M., 1996, ApJ, 462, 563

Pettorino V., Amendola L., Baccigalupi C., Quercellini C., 2012, Phys. Rev. D, 86, 103507

Ratra B., Peebles P. J. E., 1988, Phys. Rev. D, 37, 3406

Springel V., 2005, MNRAS, 364, 1105

Wetterich C., 1995, A&A, 301, 321

Zlatev I., Wang L., Steinhardt P. J., 1999, Physical Review Letters, 82, 896

References

Monthly Notices of the ROYAL ASTRONOMICAL SOCIETY

Mon. Not. R. Astron. Soc. **418,** 2715–2719 (2011) doi:10.1111/j.1365-2966.2011.19660.x

Vector dark energy and high-z massive clusters

Edoardo Carlesi,[1⋆] Alexander Knebe,[1] Gustavo Yepes,[1] Stefan Gottlöber,[2] Jose Beltrán Jiménez[3,4] and Antonio L. Maroto[5]

[1]*Departamento de Física Teórica, Universidad Autónoma de Madrid, 28049 Cantoblanco, Madrid, Spain*
[2]*Leibniz Institut für Astrophysik, An der Sternwarte 16, 14482 Potsdam, Germany*
[3]*Institute de Physique Théorique and Center for Astroparticle Physics, Université de Genève, 24 quai E. Ansermet, 1211 Genève, Switzerland*
[4]*Institute of Theoretical Astrophysics, University of Oslo, 0315 Oslo, Norway*
[5]*Departamento de Física Teórica, Universidad Complutense de Madrid, 28040 Madrid, Spain*

Accepted 2011 August 18. Received 2011 July 7

ABSTRACT

The detection of extremely massive clusters at $z > 1$ such as SPT-CL J0546−5345, SPT-CL J2106−5844 and XMMU J2235.3−2557 has been considered by some authors as a challenge to the standard Λ cold dark matter cosmology. In fact, assuming Gaussian initial conditions, the theoretical expectation of detecting such objects is as low as $\leq$1 per cent. In this paper we discuss the probability of the existence of such objects in the light of the vector dark energy paradigm, showing by means of a series of N-body simulations that chances of detection are substantially enhanced in this non-standard framework.

Key words: methods: numerical – galaxies: haloes – cosmology: theory – dark matter.

1 INTRODUCTION

Present day cosmology is still failing to explain satisfactorily the nature of dark energy, which is supposed to dominate the energetic content of the Universe today and to be responsible for the current accelerated expansion. In the standard Λ cold dark matter (ΛCDM) model, this cosmic acceleration is generated by the presence of a cosmological constant. However, the required value for that constant turns out to be tiny when compared to the natural scale of gravity, namely the Planck scale. Thus, the gravitational interaction would hence be described by two-dimensional constants differing by many orders of magnitude, and this poses a problem of naturalness. This is the so-called 'cosmological constant problem' and it motivated to consider alternative explanations for the current acceleration of the universe by either modifying the gravitational interaction at large distances or introducing a new dynamical field.

Indeed, one of the main challenges of observational cosmology is exactly to devise new tests which could help discriminating between the constant or dynamic nature of dark energy. In this regard, several authors have recently pointed out that the observation of extremely massive clusters at high redshift, such as SPT-CL J2106−5844 (Foley et al. 2011; $z \simeq 1.18, M_{200} = (1.27 \pm 0.21) \times 10^{15}\,\mathrm{M}_{\odot}$), SPT-CL J0546−5346 (Brodwin et al. 2010; $z \simeq 1.07$, $M_{200} = (7.95 \pm 0.92) \times 10^{14}\,\mathrm{M}_{\odot}$) and XMMU J2235.3−2557 (Jee et al. 2009; $z \simeq 1.4$, $M_{200} = (7.3 \pm 1.3) \times 10^{14}\,\mathrm{M}_{\odot}$) may represent a major shortcoming of the ΛCDM paradigm, where the presence of such objects should be in principle strongly disfavoured (see e.g. Baldi & Pettorino 2011; Mortonson, Hu & Huterer 2011).

While, on the one hand, this tension could be solved keeping the standard scenario and relaxing the assumption of Gaussianity in the initial conditions (as proposed in Enqvist, Hotchkiss & Taanila 2011; Hoyle, Jimenez & Verde 2011), it could be as well possible to use this observations as a constraint for different cosmological models. In this work we look at the vector dark energy (VDE) model, where the role of the dark energy is played by a cosmic vector field (Beltrán Jiménez & Maroto 2008). By means of a series of N-body simulations, we study the large-scale clustering properties of this cosmology, computing the cumulative halo mass functions at different redshifts and comparing them to the predictions of the standard model. In this way, we are able to show that the VDE cosmology does indeed predict a higher abundance of massive haloes at all redshifts, thus enhancing the probability of observing such objects with respect to ΛCDM.

2 VECTOR DARK ENERGY

The action of the VDE model (see Beltrán Jiménez & Maroto 2008) can be written as

$$S = \int \mathrm{d}^4x\sqrt{-g}\left[-\frac{R}{16\pi G} - \frac{1}{4}F_{\mu\nu}F^{\mu\nu} - \frac{1}{2}\left(\nabla_\mu A^\mu\right)^2 + R_{\mu\nu}A^\mu A^\nu\right], \quad (1)$$

where $R_{\mu\nu}$ is the Ricci tensor, $R = g^{\mu\nu}R_{\mu\nu}$ the scalar curvature and $F_{\mu\nu} = \partial_\mu A_\nu - \partial_\nu A_\mu$. This action can be interpreted as the Maxwell term for a vector field supplemented with a gauge-fixing term and an effective mass provided by the Ricci tensor. It is interesting to note that the vector sector has no free parameters nor potential terms, being G the only dimensional constant of the theory.

⋆E-mail: edoardo.carlesi@uam.es

For a homogeneous and isotropic universe described by the flat Friedmann–Lemaître–Robertson–Walker metric :

$$ds^2 = dt^2 - a(t)^2\, \boldsymbol{dx}^2, \tag{2}$$

we have $A_\mu = (A_0(t), 0, 0, 0)$ so that the corresponding equations read

$$\ddot{A}_0 + 3H\dot{A}_0 - 3[2H^2 + \dot{H}]A_0 = 0, \tag{3}$$

$$H^2 = \frac{8\pi G}{3}\left[\rho_{\rm R} + \rho_{\rm M} + \rho_A\right], \tag{4}$$

with $H = \dot{a}/a$ the Hubble parameter and

$$\rho_A = \frac{3}{2}H^2A_0^2 + 3HA_0\dot{A}_0 - \frac{1}{2}\dot{A}_0^2, \tag{5}$$

the energy density associated to the vector field, while $\rho_{\rm M}$ and $\rho_{\rm R}$ are the matter and radiation densities, respectively. During the radiation and matter eras in which the dark energy contribution was negligible, we can solve equation (3) with $H = p/t$, where $p = 1/2$ for radiation and $p = 2/3$ for matter eras, respectively, that is equivalent to assume that $a \propto t^p$. In that case, the general solution is

$$A_0(t) = A_0^+ t^{\alpha_+} + A_0^- t^{\alpha_-}, \tag{6}$$

with $A_0^\pm$ constants of integration, $\alpha_\pm = -(1 \pm 1)/4$ in the radiation era and $\alpha_\pm = (-3 \pm \sqrt{33})/6$ in the matter era. After dark energy starts dominating, the equation of state abruptly falls towards $w_{\rm DE} \to -\infty$ as the Universe approaches $t_{\rm end}$, and the equation of state can cross the so-called phantom divide line (Nesseris & Perivolaropoulos 2007), so that we can have $w_{\rm DE}(z = 0) < -1$.

Using the growing mode solution in equation (6) we can obtain the evolution for the energy density as

$$\rho_A = \rho_{A_0}(1 + z)^\kappa, \tag{7}$$

with $\kappa = 4$ in the radiation era and $\kappa = (9-\sqrt{33})/2 \simeq -1.63$ in the matter era. Thus, the energy density of the vector field scales like radiation at early times so that the ratio $\rho_A/\rho_{\rm R}$ is constant during such a period. Moreover, the value of the vector field A_0 during that era is also constant hence making the cosmological evolution insensitive to the time at which we impose the initial conditions (as long as they are set well inside the radiation dominated epoch). Also, the required constant values of such quantities in order to fit observations are $\rho_A/\rho_{\rm R}|_{\rm early} \simeq 10^{-6}$ and $A_0^{\rm early} \simeq 10^{-4}M_{\rm p}$ which can arise naturally during the early universe, for instance, as quantum fluctuations. Furthermore, they do not need the introduction of any unnatural scale, thus, alleviating the naturalness or coincidence problem. On the other hand, when the Universe enters the era of matter domination, ρ_A starts growing relative to $\rho_{\rm M}$ eventually overcoming it at some point so that the dark energy vector field becomes the dominant component.

Once the present value of the Hubble parameter H_0 and the constant $A_0^{\rm early}$ during radiation (which fixes the total amount of matter $\Omega_{\rm M}$) are specified, the model is completely determined. In other words, this model contains the same number of parameters as ΛCDM, i.e. the minimum number of parameters of any cosmological model with dark energy. Notice, however, that in the VDE model the present value of the equation of state parameter $w_0 = -3.53$ is radically different from that of a cosmological constant [cf. Fig. 1, where the redshift evolution of $\omega(z)$ is shown the range of our simulations]. Despite this fact, VDE is able to simultaneously fit supernovae (SNe) and cosmic microwave background (CMB) data with comparable goodness to ΛCDM (Beltrán Jiménez & Maroto 2008; Beltrán Jiménez, Lazkoz & Maroto 2009).

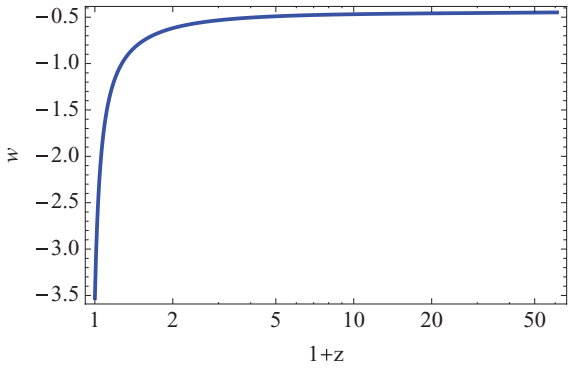

Figure 1. Equation of state of the VDE model for the best fit to SNIa data, shown in the range of our simulations.

3 THE DATA

3.1 Simulations

We wanted to estimate the probability of finding massive clusters at $z > 1$ in the VDE scenario compared to the ΛCDM one by means of CDM only N-body simulations. For this purpose, we chose to use a suitably modified version of the publicly available GADGET-2 code (Springel 2005), which had to take into account the different expansion history that characterizes the two cosmologies. In Table 1 we show the cosmological parameters used in the different simulations. For the VDE model, we have used the value of $\Omega_{\rm M}$ provided by the best fit to Type Ia SN (SNIa) data; the remaining cosmological parameters have been obtained by a fit to the *Wilkinson Microwave Anisotropy Probe* 7-year (*WMAP*7) CMB data of the model. w_0 denotes the present value of the equation of state parameter of dark energy. For ΛCDM we used the MultiDark simulation (Prada et al. 2011) cosmological parameters with a *WMAP*7 σ_8 normalization (Larson et al. 2011). In addition, we also simulated a ΛCDM-vde model, which implements the VDE values for $\Omega_{\rm M}$ and σ_8 in an otherwise standard ΛCDM picture. Although this model is certainly ruled out by current cosmological constraints, it provides none the less an interesting case study that allows us to disentangle the effects of these two cosmological parameters on structure formation in the VDE model.

We chose to run a total of eight 512^3 particles simulations summarized in Table 2 and explained below:

(i) a VDE (and a ΛCDM started with the same seed for the phases of the initial conditions) simulation in a $500\,h^{-1}$ Mpc box;

(ii) a second VDE (and again corresponding ΛCDM) simulation in a $1\,h^{-1}$ Gpc box;

(iii) two more VDE simulations with a different random seed, one in a $500\,h^{-1}$ Mpc and one in a $1\,h^{-1}$ Gpc box, as a check for the influence of cosmic variance;

(iv) two ΛCDM-vde simulations in a 500 and a $1000\,h^{-1}$ Mpc box.

Table 1. Cosmological parameters for ΛCDM, ΛCDM-vde and VDE.

Model	$\Omega_{\rm m}$	$\Omega_{\rm de}$	w_0	σ_8	h
ΛCDM	0.27	0.73	−1	0.8	0.7
ΛCDM-vde	0.388	0.612	−1	0.83	0.7
VDE	0.388	0.612	−3.53	0.83	0.62

Table 2. *N*-body settings used for the GADGET-2 simulations, the two $500\,h^{-1}$ Mpc and the two $1\,h^{-1}$ Gpc have the same initial random seed and starting redshift $z_{\rm start} = 60$ in order to allow for a direct comparison of the halo properties. The number of particles in each was fixed at 512^3. The box size B is given in h^{-1} Mpc and the particle mass in $h^{-1}\,{\rm M}_\odot$.

Simulation	B	$m_{\rm p}$
2 VDE-0.5	500	1.00×10^{11}
2 VDE-1	1000	8.02×10^{11}
ΛCDM-0.5	500	6.95×10^{10}
ΛCDM-1	1000	5.55×10^{11}
ΛCDM-0.5vde	500	1.00×10^{11}
ΛCDM-1vde	1000	8.02×10^{11}

The full set of simulations will be presented and analysed in more detail in an upcoming companion paper; in this paper, instead, we chose to focus on some of them only in order to gather information on large-scale structures and massive cluster at high redshift, respectively, in the two cosmologies. To this extent, the use of the same initial seed for generating the initial conditions in the coupled ΛCDM versus VDE simulations allows us to directly compare the structures identified by the halo finder.

As a final remark, we underline here that the choice of the boxes was made in order to allow the study of clustering on larger scales, without particular emphasis on low-mass objects, e.g. dark matter haloes with $M < 10^{14}\,h^{-1}\,{\rm M}_\odot$. This means that even though our halo finder has been able to identify objects down to $\sim 10^{12}\,h^{-1}\,{\rm M}_\odot$ in the $500\,h^{-1}$ Mpc box and $\sim 10^{13}\,h^{-1}\,{\rm M}_\odot$ in the $1\,h^{-1}$ Gpc one (which corresponds to a lower limit of 20 particles, see below), we are not comparing the mass spectrum at this far end. Therefore, since we are only interested in studying the behaviour of the mass function of these models at the very high mass end, in the following sections we will mostly refer to the ΛCDM-1, ΛCDM-vde and VDE-1 simulations, where we have a larger statistics for the supercluster scales.

3.2 Halo finding

In order to identify haloes in our simulation we have run the MPI+OpenMP hybrid halo finder AHF described in detail in Knollmann & Knebe (2009). AHF is an improvement of the MHF halo finder (Gill, Knebe & Gibson 2004), which locates local overdensities in an adaptively smoothed density field as prospective halo centres. The local potential minima are computed for each of these density peaks and the gravitationally bound particles are determined. Only peaks with at least 20 bound particles are considered as haloes and retained for further analysis, even though here we focus on the most massive objects only.

The mass of each halo is then computed via the equation $M(r) = \Delta\rho_{\rm c} 4\pi r^3/3$, where we applied $\Delta = 200$ as the overdensity threshold. Using this relation, particular care has to be taken when considering the definition of the critical density $\rho_{\rm c} = 3H^2/8\pi G$ because it involves the Hubble parameter, that differs substantially at all redshifts in the two models. This means that, identifying the halo masses, we have to take into account the fact that the value of $\rho_{\rm c}$ changes from ΛCDM to VDE. This has been incorporated into and taken care of in the latest version of AHF where $H_{\rm VDE}(z)$ is being read in from a pre-computed table.

We would like to mention that we checked that the objects obtained by this (virial) definition are in fact in equilibrium. To this extent we studied the ratio between two times kinetic over potential energy $2T/|U|$ confirming that at each redshift under investigation here this relation is equally well fulfilled for the ΛCDM and – more importantly – the VDE simulations (not presented here though). We therefore conclude that our adopted method to define halo mass in the VDE model leads to unbiased results and yields objects in equilibrium – as is the case for the ΛCDM haloes.

4 THE RESULTS

4.1 Mass function

With the halo catalogues at our disposal, we computed the cumulative mass functions $n(>M)$ at various redshifts. We show in Fig. 2 the results for the $1\,h^{-1}$ Gpc simulations at redshifts $z = 1.4$, 1.2, 1.1 and 0. This plot is accompanied by Table 3 where we list the masses of the most massive haloes found in each model and the redshifts under consideration.

We notice that the mass function for objects with $M > 10^{14}\,h^{-1}\,{\rm M}_\odot$ is several times larger in VDE than in ΛCDM at all redshifts, i.e. the number of high-mass haloes in this non-standard cosmological model is significantly increased. In particular, at this mass scale the VDE mass function is about three times larger at the relevant redshifts $z = 1.4, 1.2$ and 1.1 – and even larger at today's time.

In order to verify that this feature of the VDE model is not a simple reflection of cosmic variance (which should affect in particular the high-mass end, where the statistics is small) we compared the results presented in Fig. 2 to the mass functions of the set of two additional simulations started from a different random seed for the initial conditions confirming aforementioned results.

An interesting remark we would like to add here is that the physical mass (obtained dividing by the corresponding h values the values quoted in $h^{-1}\,{\rm M}_\odot$ units) of the largest haloes in the VDE-1 simulation at $z = 1.4$, 1.2 and 1.1 are perfectly compatible with the ones of the above clusters referred to in the Introduction, whereas the corresponding ΛCDM candidates are outside the 2σ compatibility level. And again, similar massive clusters have also been found in the duplicate VDE-1 simulation with a different initial seed.

Comparing the ΛCDM-1vde to the VDE-1 simulation at different redshifts, we note that while the two mass functions are almost indistinguishable for $M < 10^{14}\,h^{-1}\,{\rm M}_\odot$, on the higher mass end the former even outnumbers the latter by approximately ∼3. In the hierarchical picture of structure formation, we can attribute this relative difference to dynamical effects caused by the different expansion histories [based upon different $H(z)$] at later times $z \approx 1$, when the most massive structures actually start to form. In general, however, the ΛCDM-vde analysis shows that the enhancement seen in the VDE mass function with respect to ΛCDM is clearly driven by the higher values of $\Omega_{\rm M}$ and σ_8, a result expected since the abundance of clusters sensitively depends on the product of these two parameters (cf. Huterer & White 2002). On the one hand, this complicates the issue of model selection, since (although disfavoured by the *WMAP*7 data) we could invoke a (slightly) larger $\Omega_{\rm M}$ or a higher σ_8 normalization at $z = 0$ for ΛCDM trying to alleviate the current tension with the high-z massive clusters observations. On the other hand, the distinct expansion history that characterizes and differentiates between the two ΛCDM and VDE models would still leave a

Table 3. The most massive halo found in the three $1\,h^{-1}$ Gpc simulations (in units of $10^{14}\,h^{-1}\,\mathrm{M}_{\odot}$) as a function of redshift.

z	ΛCDM-1	VDE-1	ΛCDM-1vde
1.4	4.16	5.63	6.47
1.2	5.13	6.51	8.16
1.1	6.01	7.63	10.2
0	18.1	31.6	35.1

clear imprint on structure formation, which could be detected by, for instance, measuring σ_8's dependence on redshift. Such a test would indeed provide invaluable information for the study of ΛCDM and for any cosmological model beyond it such as VDE.

4.2 Probability

In order to provide a more quantitative estimate of the relative probability of observationally detecting such massive clusters at the indicated redshifts we used $n(>M, z)$ – the expected cumulative number density of objects above a threshold mass M as a function of redshift as given by our simulations – and integrated it over the comoving volume V_c of the survey:

$$N(>M) = \int_{\Delta z, \Omega_{\mathrm{survey}}} n(>M, z)\, \mathrm{d}V_c(z), \tag{8}$$

where Δz and Ω_{survey} are the redshift interval and the fraction of the sky covered by the survey to which we want to compare our theoretical expectations.

While $n(>M, z)$ can be readily calculated in ΛCDM cosmologies (e.g. Press & Schechter 1974; Sheth & Tormen 1999; Jenkins et al. 2001; Tinker et al. 2008), in VDE we have to devise a strategy to compute it based upon our numerical results only. We chose to adjust the formula of Sheth & Tormen (1999) as follows:

(i) we calculated the cumulative number densities in the desired redshift intervals Δz based upon our simulation data;

(ii) we adjusted the parameters of the Sheth–Tormen mass function fitting the numerical cumulative number densities derived from the VDE-1 and VDE-0.5 simulations;

(iii) we used these best-fitting estimates to analytically compute $n(>M, z)$ now having access to masses even outside our numerically limited range to be used with equation (8).

The results of the numerical integration over the comoving volumes (obtained using the limits quoted in the observational papers by Jee et al. 2009; Brodwin et al. 2010; Foley et al. 2011) are listed in Table 4 for the VDE, ΛCDM-vde and ΛCDM model. We can clearly see that the chances are substantially larger in the VDE model to find such massive objects than in ΛCDM; the numbers for VDE is in fact comparable to our fiducial ΛCDM-vde model confirming their relation to the enhanced values of Ω_{M} and σ_8. However, note that while the VDE model is compliant with both SNIa and CMB data the ΛCDM-vde is obviously ruled out

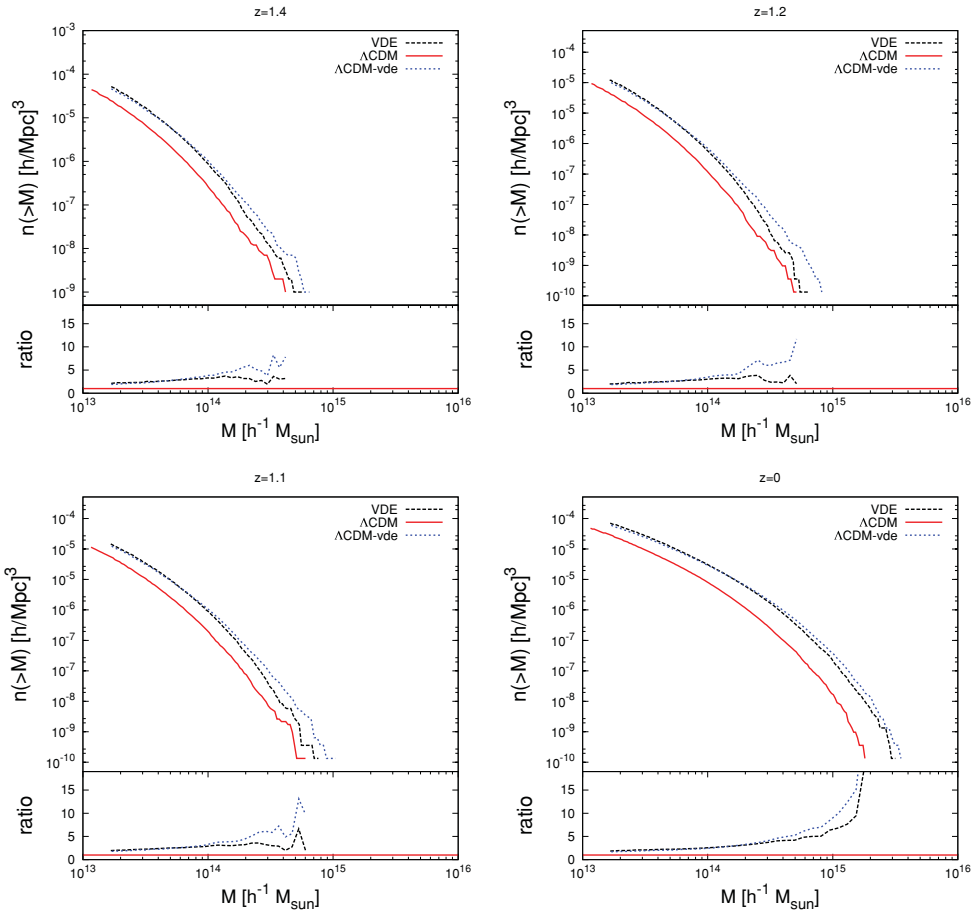

Figure 2. Mass functions (and their ratios) as computed for the VDE-1, ΛCDM-1 and ΛCDM-1vde simulations at $z = 1.4, 1.2, 1.1$ and 0. These redshifts have been chosen in order to overlap with the aforementioned observed massive clusters.

Table 4. Expected number of objects $N(>M)$ in excess of mass M and inside a certain (comoving) volume in the ΛCDM and VDE for different mass thresholds and survey volumes. Solid angles Ω are measured in deg^2 and masses are measured in $10^{14}\,h^{-1}\,\mathrm{M}_\odot$.

M	Δz	$\Omega_{\rm survey}$	$N_{\Lambda\rm CDM}$	$N_{\rm VDE}$	$N_{\Lambda\rm CDM-vde}$
>10	>1	2500	0.007	0.02	0.04
>7	>1	2500	0.03	0.31	0.56
>5	1.38–2.2	11	0.005	0.06	0.07

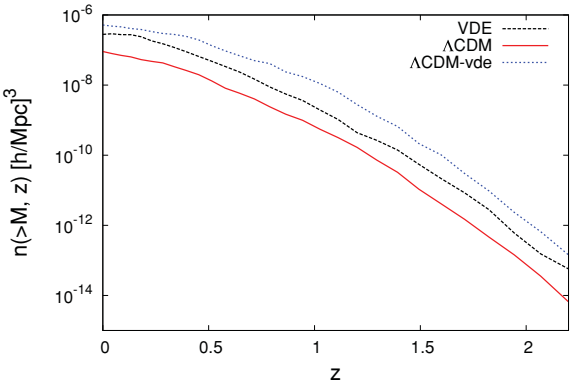

Figure 3. Numerical cumulative number densities of objects with $M > 5 \times 10^{14}\,h^{-1}\,\mathrm{M}_\odot$ for VDE, ΛCDM and ΛCDM-vde.

observationally. We complement these results with Fig. 3 where we plot the abundance evolution of clusters with mass $M > 5 \times 10^{14}\,h^{-1}\,\mathrm{M}_\odot$ computed utilizing above described procedure again. This plot confirms our previous analysis of the mass functions and shows that the expectation of massive objects is amplified in VDE by a factor of ∼3 to ∼10 over the considered redshift range, a factor which is even higher for the discretionary ΛCDM-vde. We would like to remark here that while our ΛCDM estimate for XMMU J2235.3−2557 is in agreement with the result quoted by Jee et al. (2009) (obtained using the same approach as here), the calculation done for SPT-CL J2106−5844 leads to an estimate substantially smaller than the one quoted by Foley et al. (2011), calculated using a Monte Carlo technique. However, this does not affect our conclusions, which are based on the comparison of results obtained in a consistent manner for the two models.

5 CONCLUSIONS

The observation of massive clusters at $z > 1$ provides an additional, useful test for the ΛCDM and other cosmological models beyond the standard paradigm. In this paper we have shown that the VDE scenario (Beltrán Jiménez & Maroto 2008) might account for such observations better than the ΛCDM concordance model, since the relative abundance of extremely massive clusters with $M > 5 \times 10^{14}\,h^{-1}\,\mathrm{M}_\odot$ is at all redshifts higher in this non-standard cosmology: the expected number of massive clusters is enhanced in VDE by at least a factor of ∼3 to find an object such as SPT-CL J2106−5844 at redshift $z \approx 1.2$ (Foley et al. 2011) and a factor of ∼10 for the other two observed clusters SPT-CL J0546−5346 (Brodwin et al. 2010) and XMMU J2235.3−2557 (Jee et al. 2009). Of course, these results might as well simply point in the direction of modifying the standard paradigm, for example including non-Gaussianities in the initial conditions or either using a higher σ_8 or $\Omega_{\rm M}$ value for the ΛCDM as the comparison to the ΛCDM-vde model seems to suggest.

None the less, this first results on the large-scale clustering in the case of VDE cosmology point in the right direction, significantly enhancing the probability of producing extremely massive clusters at high redshift as recent observations seem to require. For a more elaborate discussion and comparison of the VDE to the ΛCDM model (not solely focusing on massive clusters) we though refer the reader to the companion paper (Carlesi et al., in preparation).

ACKNOWLEDGMENTS

EC is supported by the MareNostrum project funded by the Spanish Ministerio de Ciencia e Innovacion (MICINN) under grant no. AYA2009-13875-C03-02 and MultiDark Consolider project under grant CSD2009-00064. AK acknowledges support by the MICINN's Ramon y Cajal programme as well as the grants AYA 2009-13875-C03-02, AYA2009-12792-C03-03, CSD2009-00064, and CAM S2009/ESP-1496. GY acknowledges support from MICINN's grants AYA2009-13875-C03-02 and FPA2009-08958. JBJ is supported by the Ministerio de Educación under the post-doctoral contract EX2009-0305 and also wishes to acknowledge support from the Norwegian Research Council under the YGGDRASIL programme 2009-2010 and the NILS mobility project grant UCM-EEA-ABEL-03-2010. We also acknowledge support from MICINN (Spain) project numbers FIS 2008-01323, FPA 2008-00592 and CAM/UCM 910309.

REFERENCES

Baldi M., Pettorino V., 2011, MNRAS, 412, L1
Beltrán Jiménez J., Maroto A. L., 2008, Phys. Rev. D, 78, 063005
Beltrán Jiménez J., Lazkoz R., Maroto A. L., 2009, Phys. Rev. D, 80, 023004
Brodwin M. et al., 2010, ApJ, 721, 90
Enqvist K., Hotchkiss S., Taanila O., 2011, J. Cosmol. Astropart. Phys., 4, 17
Foley R. et al., 2011, ApJ, 731, 86
Gill S. P. D., Knebe A., Gibson B. K., 2004, MNRAS, 351, 399
Hoyle B., Jimenez R., Verde L., 2011, Phys. Rev. D, 83, 103502
Huterer D., White M., 2002, ApJ, 578, L95
Jee M. et al., 2009, ApJ, 704, 672
Jenkins A., Frenk C. S., White S. D. M., Colberg J. M., Cole S., Evrard A. E., Couchman H. M. P., Yoshida N., 2001, MNRAS, 321, 372
Knollmann S. R., Knebe A., 2009, ApJS, 182, 608
Larson D. et al., 2011, ApJS, 192, 16
Mortonson M. J., Hu W., Huterer D., 2011, Phys. Rev. D, 83, 023015
Nesseris S., Perivolaropoulos L., 2007, J. Cosmol. Astropart. Phys., 0701, 018
Prada F., Klypin A. A., Cuesta A. J., Betancort-Rijo J. E., Primack J., 2011, arXiv e-prints
Press W. H., Schechter P., 1974, ApJ, 187, 425
Sheth R. K., Tormen G., 1999, MNRAS, 308, 119
Springel V., 2005, MNRAS, 364, 1105
Tinker J., Kravtsov A. V., Klypin A., Abazajian K., Warren M., Yepes G., Gottlöber S., Holz D. E., 2008, ApJ, 688, 709

This paper has been typeset from a TEX/LATEX file prepared by the author.

Monthly Notices
of the
ROYAL ASTRONOMICAL SOCIETY

Mon. Not. R. Astron. Soc. **424,** 699–715 (2012) doi:10.1111/j.1365-2966.2012.21258.x

N-body simulations with a cosmic vector for dark energy

Edoardo Carlesi,[1⋆] Alexander Knebe,[1] Gustavo Yepes,[1] Stefan Gottlöber,[2] Jose Beltrán Jiménez[3,4] and Antonio L. Maroto[5]

[1]*Departamento de Física Teórica, Universidad Autónoma de Madrid, 28049 Cantoblanco, Madrid, Spain*
[2]*Leibniz Institut für Astrophysik, An der Sternwarte 16, 14482 Potsdam, Germany*
[3]*Institute de Physique Théorique and Center for Astroparticle Physics, Université de Genève, 24 quai E. Ansermet, 1211 Genève, Switzerland*
[4]*Institute of Theoretical Astrophysics, University of Oslo, 0315 Oslo, Norway*
[5]*Departamento de Física Teórica, Universidad Complutense de Madrid, 28040 Madrid, Spain*

Accepted 2012 May 6. Received 2012 April 16; in original form 2012 January 12

ABSTRACT

We present the results of a series of cosmological *N*-body simulations of a vector dark energy (VDE) model, performed using a suitably modified version of the publicly available GADGET-2 code. The set-ups of our simulations were calibrated pursuing a twofold aim: (1) to analyse the large-scale distribution of massive objects and (2) to determine the properties of halo structure in this different framework. We observe that structure formation is enhanced in VDE, since the mass function at high redshift is boosted up to a factor of 10 with respect to Λ cold dark matter (ΛCDM), possibly alleviating tensions with the observations of massive clusters at high redshifts and early reionization epoch. Significant differences can also be found for the value of the growth factor, which in VDE shows a completely different behaviour, and in the distribution of voids, which in this cosmology are on average smaller and less abundant. We further studied the structure of dark matter haloes more massive than $5 \times 10^{13}\,h^{-1}\,\mathrm{M}_{\odot}$, finding that no substantial difference emerges when comparing spin parameter, shape, triaxiality and profiles of structures evolved under different cosmological pictures. Nevertheless, minor differences can be found in the concentration–mass relation and the two-point correlation function, both showing different amplitudes and steeper slopes. Using an additional series of simulations of a ΛCDM scenario with the same Ω_{M} and σ_8 used in the VDE cosmology, we have been able to establish whether the modifications induced in the new cosmological picture were due to the particular nature of the dynamical dark energy or a straightforward consequence of the cosmological parameters. On large scales, the dynamical effects of the cosmic vector field can be seen in the peculiar evolution of the cluster number density function with redshift, in the shape of the mass function, in the distribution of voids and on the characteristic form of the growth index $\gamma(z)$. On smaller scales, internal properties of haloes are almost unaffected by the change of cosmology, since no statistical difference can be observed in the characteristics of halo profiles, spin parameters, shapes and triaxialities. Only halo masses and concentrations show a substantial increase, which can, however, be attributed to the change in the cosmological parameters.

Key words: galaxies: haloes – cosmology: theory – dark matter.

1 INTRODUCTION

During the last 12 years, a large amount of cosmological high-precision data on Type Ia supernovae (SNeIa; see Riess et al. 1998; Perlmutter et al. 1999; Guy et al. 2010), cosmic microwave background (CMB) anisotropies (Larson et al. 2011; Sherwin et al. 2011), weak lensing (Huterer 2010), baryon acoustic oscillations (Beutler et al. 2011) and large-scale structure surveys (Abazajian et al. 2009) has provided evidence that the Universe we live in is of a flat geometry and undergoing an accelerated expansion. These observations motivate our belief in the existence of a ubiquitous fluid called dark energy (DE) that, by the exertion of a negative pressure, counters and eventually overcomes the gravitational attraction that would otherwise dominate the evolution of our Universe. The simplest explanation to the nature of this fluid is found in the

⋆E-mail: edoardo.carlesi@uam.es

standard model of cosmology Λ cold dark matter (ΛCDM), where the role of the DE is played by a cosmological constant Λ obeying the equation of state $p_\Lambda = -\rho_\Lambda$. Although perfectly consistent with all the aforementioned observations, ΛCDM still lacks an appeal from a purely theoretical point of view. In fact, if we believe the cosmological constant to be the zero-point energy of some fundamental quantum field, its introduction in the Friedmann equations requires a fine tuning of several tens of orders of magnitude (depending on the energy scale we choose to be fundamental in our theory), spoiling the naturalness of the whole ΛCDM picture.

Another issue we encounter when dealing with the standard cosmological model is the so-called *coincidence problem*, i.e. the difficulty to explain in a natural way the fact that today's matter and DE densities have a comparable value although they evolved in a completely different manner throughout most of the history of the universe.

In an attempt to overcome these two difficulties of ΛCDM, Jimenez & Maroto (2009) introduced the vector dark energy (VDE) model, where a cosmic vector field plays the role of a dynamical DE component, replacing the cosmological constant Λ. Besides being compatible with SN observations and CMB precision measurements, this scenario has the same number of free parameters as ΛCDM. Moreover, the initial value of the vector field (which is of the order of $10^{-4}M_{\rm p}$,[1] a scale that could arise naturally in inflation) and its global dynamics ensure the model to overcome the standard model's naturalness problems. In the present work, we study the impact of this VDE model on structure formation and evolution by means of a series of cosmological N-body simulations, analysing the effects of this alternative cosmology in the deeply non-linear regime and highlighting its imprints on cosmic structures, in particular emphasizing the differences emerging with respect to the standard ΛCDM model. To be able to disentangle the effects due to the different parameters from those induced by the different dynamics of the background in VDE cosmology, we have also run a set of simulations for a ΛCDM-vde cosmology, i.e. a model that embeds VDE parameters (presented in Section 2) in a standard ΛCDM picture.

Although ruled out by current cosmological constraints, this model provides none the less an interesting case study that allows us to shed light on the effects of these two cosmological parameters on structure formation in the VDE model.

The paper is organized as follows. In Section 2, we briefly introduce the VDE model, discussing its most important mathematical and physical characteristics. In Section 3, we describe the set-up as well as the modifications to the code and the initial conditions necessary to run the N-body simulation. In Sections 4 and 5, we will present a detailed analysis of the results, focusing on the main differences of the VDE models from the standard ΛCDM cosmology, first analysing the large-scale structure and then (cross-)comparing properties of dark matter haloes. A short summary of the results obtained and a discussion on their implications are then presented in Section 6.

2 THE MODEL

In this section, we will provide the basic mathematical and physical description of the VDE model. For more details and an in-depth discussion on the results obtained and their derivation, we refer the reader to Beltrán Jiménez & Maroto (2008). The action of the proposed VDE model can be written as

$$S = \int \mathrm{d}^4x\sqrt{-g}\left[-\frac{R}{16\pi G} - \frac{1}{4}\boldsymbol{F}_{\mu\nu}\boldsymbol{F}^{\mu\nu} - \frac{1}{2}(\nabla_\mu \boldsymbol{A}^\mu)^2 + \boldsymbol{R}_{\mu\nu}\boldsymbol{A}^\mu\boldsymbol{A}^\nu\right], \quad (1)$$

where $\boldsymbol{R}_{\mu\nu}$ is the Ricci tensor, $R = \boldsymbol{g}^{\mu\nu}\boldsymbol{R}_{\mu\nu}$ the scalar curvature and $\boldsymbol{F}_{\mu\nu} = \partial_\mu \boldsymbol{A}_\nu - \partial_\nu \boldsymbol{A}_\mu$. This action can be interpreted as a Maxwell term for a vector field supplemented with a gauge-fixing term and an effective mass provided by the Ricci tensor. It is interesting to note that the vector sector has neither free parameters nor potential terms, G being the only dimensional constant of the theory. This is one of the main differences of this model with respect to those based on scalar fields, which need the presence of potential terms to be able to lead to late-time accelerated expansion.

The classical equations of motion derived from the action (1) are the Einstein and vector field equations given by

$$\boldsymbol{R}_{\mu\nu} - \frac{1}{2}R\boldsymbol{g}_{\mu\nu} = 8\pi G(\boldsymbol{T}_{\mu\nu} + \boldsymbol{T}^{A}_{\mu\nu}), \quad (2)$$

$$\Box \boldsymbol{A}_\mu + \boldsymbol{R}_{\mu\nu}\boldsymbol{A}^\nu = 0, \quad (3)$$

where $\boldsymbol{T}_{\mu\nu}$ is the conserved energy–momentum tensor for matter and radiation (and/or other possible components present in the Universe) and $\boldsymbol{T}^{A}_{\mu\nu}$ is the energy–momentum tensor coming from the vector field sector (and that is also covariantly conserved). In the following, we shall solve the equations of the vector field during the radiation and matter eras, in which the contribution of DE is supposed to be negligible. In those epochs, the geometry of the universe is well described by the flat Friedmann–Lemaître–Robertson–Walker metric:

$$\mathrm{d}s^2 = \mathrm{d}t^2 - a(t)^2\mathrm{d}\boldsymbol{x}^2. \quad (4)$$

For the homogeneous vector field, we shall assume, without lack of generality, the form $A_\mu = (A_0(t), 0, 0, A_z(t))$, so that the corresponding equations read

$$\ddot{A}_0 + 3H\dot{A}_0 - 3\left(2H^2 + \dot{H}\right)A_0 = 0, \quad (5)$$

$$\ddot{A}_z + H\dot{A}_z - 2\left(\dot{H} + 3H^2\right)A_z = 0, \quad (6)$$

where $H = \dot{a}/a$. These equations can be easily solved for a power-law expansion with $H = p/t$, in which case we obtain the following solutions:

$$A_0(t) = A_0^+ t^{\alpha_+} + A_0^- t^{\alpha_-}, \quad (7)$$

$$A_z(t) = A_z^+ t^{2p} + A_z^- t^{1-3p}, \quad (8)$$

with $\alpha_\pm = \frac{1}{2}(1-3p\pm\sqrt{33p^2-18p+1})$ and $A_0^\pm$ and $A_z^\pm$ constants of integration. Thus, in the radiation-dominated epoch ($p = 1/2$) we have the growing modes $A_0 =$ constant and $A_z \propto t$, whereas for the matter-dominated epoch ($p = 2/3$) we have $A_0 \propto t^{(-3+\sqrt{33})/6}$ and $A_z \propto t^{4/3}$. Concerning the energy densities, the corresponding expressions are given by

$$\rho_{A_0} = \frac{3}{2}H^2A_0^2 + 3HA_0\dot{A}_0 - \frac{1}{2}\dot{A}_0^2, \quad (9)$$

$$\rho_{A_z} = \frac{1}{2a^2}\left(4H^2A_z^2 - 4HA_z\dot{A}_z + \dot{A}_z^2\right). \quad (10)$$

At this point, it is interesting to note that when we insert the full solution for A_z given in (8) in its corresponding energy density, we obtain

$$\rho_{A_z} = \frac{\left(A_z^-\right)^2}{2a^8}(25p^2 - 10p + 1), \quad (11)$$

[1] $M_{\rm p}$ being the Planck mass.

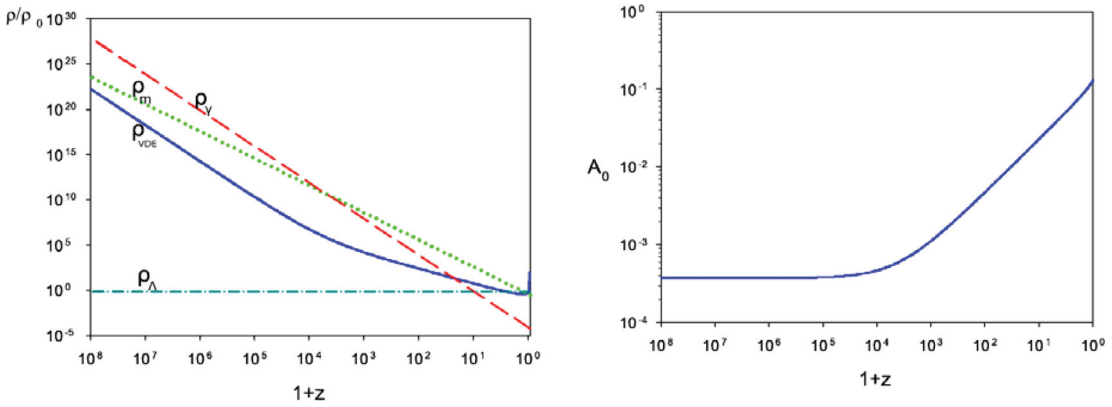

Figure 1. Left-hand plot: evolution of the energy densities. Dashed (red) for radiation, dotted (green) for matter and solid (blue) for VDE. We also show for comparison the cosmological constant energy density in dot–dashed line. We see the scaling behaviour of the cosmic vector in the early universe and the rapid growth of its energy density contribution at late times when approaching the final singularity. Right-hand plot: evolution of the temporal component of the vector field where we see that it takes a constant value at very high redshifts so that the cosmological evolution is insensitive to the precise redshift at which we set the initial value of the cosmic vector.

so that the mode A_z^+ does not contribute to the energy density. That way, even though A_z grows with respect to A_0, the corresponding physical quantity, i.e. its energy density, decays with respect to that of the temporal component. It is easy to check that the ratio ρ_{A_z}/ρ_{A_0} decays as a^{-4} in the radiation era and as $a^{-6.37}$ in the matter era, so that the energy density of the vector field becomes dominated by the contribution of the temporal component. That justifies neglecting the spatial components and dealing uniquely with the temporal one.

On the other hand, the potential large-scale anisotropy generated by the presence of spatial components of the vector field is determined by the relative difference of pressures in different directions $p_\parallel$ and $p_\perp$, which is given by

$$p_\parallel - p_\perp = \frac{3}{a^2}\left(4H^2A_z^2 - 4HA_z\dot{A}_z + \dot{A}_z^2\right). \tag{12}$$

This expression happens to be proportional to ρ_{A_z} so that we have that $(p_\parallel - p_\perp)/\rho_A$ will decay as the universe expands in the same manner as ρ_{A_z} and the large-scale isotropy of the universe suggested by CMB observations is not spoiled. Hence, in the following we shall neglect the spatial components of the vector field and uniquely consider the temporal one, since it gives the dominant contribution to the energy–momentum tensor of the vector field. However, we should emphasize here that this does not result in effectively having a scalar field. As commented before, for a minimally coupled scalar field, one needs to introduce a certain potential (that will depend on some dimensional parameters) to have accelerated expansion, whereas in the VDE model we get accelerated solutions with only kinetic terms and without introducing any new dimensional parameter.

The energy density of the vector field is given by

$$\rho_A = \rho_{A0}(1+z)^\kappa, \tag{13}$$

with $\kappa = 4$ in the radiation era and $\kappa = (9-\sqrt{33})/2 \simeq -1.63$ in the matter era. We can also calculate the effective equation of state for DE as

$$w_{\rm DE} = \frac{p_A}{\rho_A} = \frac{-3\left(\frac{5}{2}H^2 + \frac{4}{3}\dot{H}\right)A_0^2 + HA_0\dot{A}_0 - \frac{3}{2}\dot{A}_0^2}{\frac{3}{2}H^2A_0^2 + 3HA_0\dot{A}_0 - \frac{1}{2}\dot{A}_0^2}. \tag{14}$$

Again, using the approximate solutions in (7), we obtain

$$w_{\rm DE} = \begin{cases} \frac{1}{3} & \text{radiation era} \\ \frac{3\sqrt{33}-13}{\sqrt{33}-15} \simeq -0.457 & \text{matter era.} \end{cases} \tag{15}$$

From the evolution of the energy density of the vector field, we see that it scales as radiation at early times, so that $\rho_A/\rho_{\rm R} =$ constant. However, when the Universe enters its matter era, ρ_A starts growing relative to $\rho_{\rm M}$, eventually overcoming it at some point, at which the DE vector field would become the dominant component. From that point on, we cannot obtain analytic solutions to the field equations and we need to numerically solve the corresponding equations. In Fig. 1, we show such a numerical solution to the exact equations, which confirms our analytical estimates in the radiation and matter eras. Note that, since A_0 is constant during the radiation era, the solutions do not depend on the precise time at which we specify the initial conditions as long as we set them well inside the radiation epoch. Thus, once the present value of the Hubble parameter H_0 and the constant A_0 during radiation (which indirectly fixes the total matter density $\Omega_{\rm M}$) are specified, the model is completely determined. In other words, this model contains the same number of parameters as ΛCDM, i.e. the minimum number of parameters of any cosmological model with DE.

Not only does the VDE model have the minimum required number of parameters, but also it allows us to alleviate the so-called naturalness or coincidence problems that most DE models have. This is so because the required value for the constant value that the vector field takes in the early universe happens to be $\sim 10^{-4}M_{\rm p}$. This value, besides being relatively close to the Planck scale, could naturally arise from quantum fluctuations during inflation, for instance. On the other hand, the fact that the energy density of the vector field scales as radiation in the early universe also goes in the right direction of alleviating the aforementioned problems because the fraction of dark energy during that period remains constant. Moreover, the said fraction is $\Omega_A^{\rm early} \equiv \rho_A/\rho_{\rm R} \simeq 10^{-6}$, which, again, is in agreement with the usual magnitude of the quantum fluctuations produced during inflation.

After DE starts dominating, the equation of state abruptly falls towards $w_{\rm DE} \to -\infty$ as the Universe approaches a finite time $t_{\rm end}$. As shown in Fig. 2, during the cosmological evolution, the equation of state crosses the so-called phantom divide line, so that we have $w_{\rm DE}(z=0) < -1$. The final stage of the universe in this model is a singularity usually called Type III or Big Freeze, in which the scale factor remains finite, but the Hubble expansion rate, the energy density and the pressure diverge. This is a distinct feature of the VDE model as compared to quintessence fields for which the

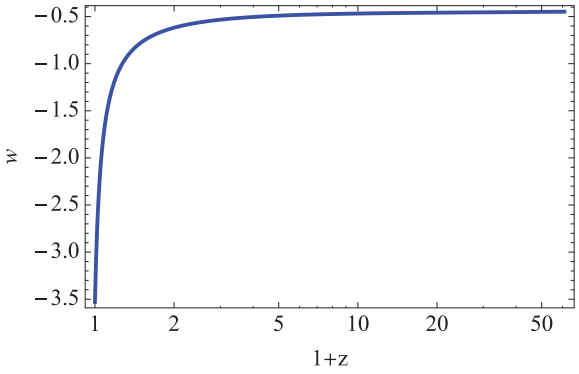

Figure 2. Evolution of DE equation of state where we can see the crossing of the phantom divide line and its evolution towards $-\infty$ as the final singularity is approached.

Table 1. *N*-body settings and cosmological parameters used for the GADGET-2 simulations. The two 500 h^{-1} Mpc and the two 1 h^{-1} Gpc have the same initial random seed (in order to allow for a direct comparison of the halo properties) and starting redshift $z_{\rm start} = 60$. The number of particles in each run was fixed at 512^3. The box size B is given in units of h^{-1} Mpc and the particle mass ($m_{\rm p}$) in $10^{11}\,h^{-1}\,{\rm M}_{\odot}$.

Simulation	$\Omega_{\rm m}$	$\Omega_{\rm DE}$	σ_8	h	B	$m_{\rm p}$
2 ×VDE-0.5	0.388	0.612	0.83	0.62	500	1.00
2 ×VDE-1	0.388	0.612	0.83	0.62	1000	8.02
ΛCDM-0.5	0.27	0.73	0.8	0.7	500	0.69
ΛCDM-1	0.27	0.73	0.8	0.7	1000	5.55
ΛCDM-0.5vde	0.388	0.612	0.83	0.7	500	1.00
ΛCDM-1vde	0.388	0.612	0.83	0.7	1000	8.02

equation of state is restricted to be >-1 so that no crossing of the phantom divide line is possible. In fact, for a DE model based on scalar fields, one needs either non-standard kinetic terms involving higher derivative terms in the action or the presence of several interacting scalar fields to achieve a transition from $w > -1$ to a phantom behaviour ($w < -1$). In either case, non-linear derivative interactions or multiple scalar field scenarios, additional degrees of freedom are introduced, whereas the VDE model is able to obtained the mentioned transition with only the degree of freedom given by the temporal component of the vector field.

Note that in the VDE model the present value of the equation of state parameter $w_0 = -3.53$ is radically different from that of a cosmological constant [cf. Fig. 1, where the redshift evolution of $w(z)$ is shown in the range of our simulations]. The values of other cosmological parameters also differ importantly from those of ΛCDM (see Table 1). Despite this fact, VDE is able to simultaneously fit SNe and CMB data with comparable goodness to ΛCDM (Beltrán Jiménez & Maroto 2008; Beltrán Jiménez, Lazkoz & Maroto 2009).

In particular, for CMB,[2] the χ^2 for the best-fitting parameters for ΛCDM is 48.3, whereas for the VDE model we obtain $\chi^2 = 51.8$ for the parameters used to run our simulations. Thus, even though the equation of state evolution is the one shown in Fig. 2, the VDE model provides good fits to observations, as shown in Fig. 3.

This might seem to be surprising if we note that the present equation of state for the VDE model is $w_0 = -3.53$, which is far from

[2] We use the binned data of *WMAP*7.

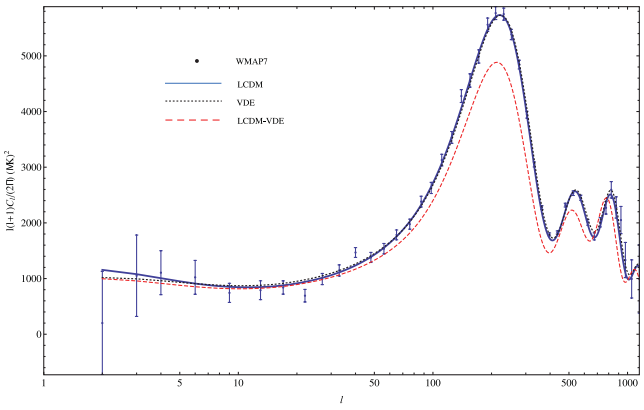

Figure 3. ΛCDM and VDE best-fitting values for the CMB spectrum versus *WMAP*7 data, showing the viability of VDE cosmology. The same curve is also shown for a ΛCDM-vde cosmology, which is clearly ruled out.

the usual constraints on this parameter obtained from cosmological observations. Such constraints are usually obtained by assuming a certain parametrization for the time variation of the DE equation of state. However, the different parametrizations used are normally such that ΛCDM is included in the parameter space. If we look at Fig. 2, we can see that the evolution of the equation of state for the VDE model crucially differs from those of ΛCDM or quintessence models and, indeed, it cannot be properly described by the most popular parametrizations. This means that we cannot directly apply the existing constraints to the VDE model, but a direct comparison of its predictions to observations is required.

As a final remark, in the simulations we will not include inhomogeneous perturbations of the vector field, but only the effects of having a different background expansion will be considered.

In Fig. 4, we show the matter power spectrum for both ΛCDM and VDE models. The differences can be ascribed to the fact of having different cosmological parameters that change the normalization

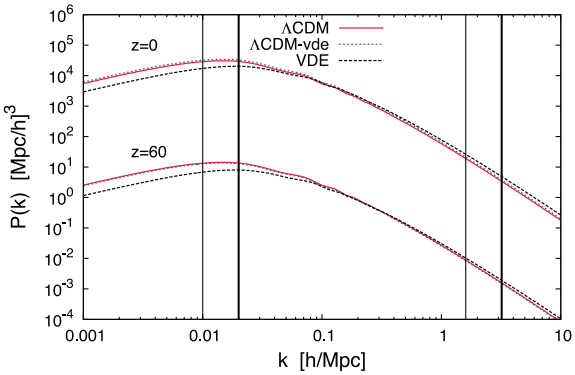

Figure 4. Linear matter overdensity power spectra at $z = 0$ and 60 for VDE, ΛCDM and ΛCDM-vde plotted versus wavenumber k. Vertical solid thick black lines refer to the k-space interval covered by the 500 h^{-1} Mpc simulations, whereas the thin ones refer to the 1 h^{-1} Gpc one. All matter power spectra at $z = 0$ have been normalized to the σ_8 values shown in Table 1 and then rescaled to $z = 60$ via the linear growth factor. We note that for $k < 0.05\,h\,{\rm Mpc}^{-1}$, ΛCDM and ΛCDM-vde have more power than VDE, whereas on smaller scales the opposite is true. We also note that due to the different value of σ_8 normalization the ΛCDM-vde $P(k)$ is slightly larger than the ΛCDM one at $z = 0$, while the different growth factor, which is larger in the ΛCDM-vde cosmology, affects the setting of the initial conditions, where the latter power spectrum lies below the former.

and the matter–radiation equality scale $k_{\rm eq}$, which are the only two differences observed. Note that the transfer function is the same in both cases, since the slopes before and after the $k_{\rm eq}$ are the same, so that we do not expect strong effects at early times which could affect the evolution of density parameters.

3 THE *N*-BODY SIMULATIONS

In this section, we will explain the (numerical) methods used in this work, with a particular emphasis on the necessary modifications of the standard *N*-body and halo-finding algorithms, also describing the procedures followed to test their accuracy and reliability.

3.1 Set-up

The *N*-body simulations presented in this work have been carried out using a suitably modified version of the Tree-PM code GADGET-2 (Springel 2005). It has also been necessary to generate a particular set of initial conditions to consistently account for the VDE-induced modifications to the standard paradigm. In Table 1, we show the most relevant cosmological parameters used in the different simulations. For the VDE model, we have used the value of $\Omega_{\rm M}$ provided by the best fit to SNIa data, whereas the remaining cosmological parameters have been obtained by a fit of the model to the *WMAP*7 data set. For ΛCDM, we used the Multidark Simulation (Prada et al. 2011) cosmological parameters with a *WMAP*7 σ_8 normalization (Larson et al. 2011).

In addition, we also simulated the so-called ΛCDM-vde model, which implements the VDE values for the total matter density $\Omega_{\rm M}$ and fluctuation amplitude σ_8 in an otherwise standard ΛCDM picture.

In particular, we want to be able to determine the impact of the different parameters on cosmological scales, with a particular emphasis on the very large structures and the most massive clusters, where observations are starting to clash with the predictions of the current standard model (see Jee et al. 2009; Baldi & Pettorino 2011; Carlesi et al. 2011; Enqvist, Hotchkiss & Taanila 2011; Hoyle, Jimenez & Verde 2011). Therefore, we need to determine whether the results derived from our VDE simulations can be solely attributed to its extremely different values for the cosmological parameters or actually by the presence of the cosmic vector field. In other words, we want to separate the signatures of the *dynamics*-driven effects from the *parameter*-driven ones, with a focus on large-scale structures, where the imprints are stronger and more clearly connected to the cosmological model. We chose to run a total of eight 512^3 particle simulations summarized in Table 1 and explained below.

(i) Two VDE simulations, i.e. a $500\,h^{-1}$ Mpc and a $1\,h^{-1}$ Gpc box.

(ii) Two ΛCDM simulations with the same box sizes and initial seeds as the VDE runs above.

(iii) Two more VDE simulations with a different random seed, again one in a $500\,h^{-1}$ Mpc and another in a $1\,h^{-1}$ Gpc box (both serving as a check for the influence of cosmic variance).

(iv) Two ΛCDM-vde simulations, one again in a $500\,h^{-1}$ Mpc and another in a $1\,h^{-1}$ Gpc box.

All runs were performed on 64 CPUs using the MareNostrum cluster at the Barcelona Supercomputing Center. Most of the results we will discuss and analyse here are based on the $500\,h^{-1}$ Mpc simulations as they have the better mass resolution. The $1\,h^{-1}$ Gpc runs primarily serve as a confirmation of the results and have already been discussed in Carlesi et al. (2011).

3.2 Code modifications

In the following paragraph, we are going to describe the procedures followed to implement the modifications needed in order to run our *N*-body simulations consistently and reliably. This is in principle a non-trivial issue, since, as described in Section 2, we need to incorporate a large number of different features that affect both the code used for the simulations and the initial conditions.

In particular, we have to handle with care three features that distinguish it from ΛCDM, i.e.

(i) the matter power spectrum $P(k, z)$ (shown in Fig. 4) and its normalization σ_8,
(ii) the expansion history $H(z)$ (see Fig. 5) and
(iii) the linear growth factor $D^+(z)$ (cf. Fig. 6).

Whereas the first and the last points affect the system's initial conditions, the second one enters directly into the *N*-body time integration, and has to be taken into account by a modification of the simulation code.

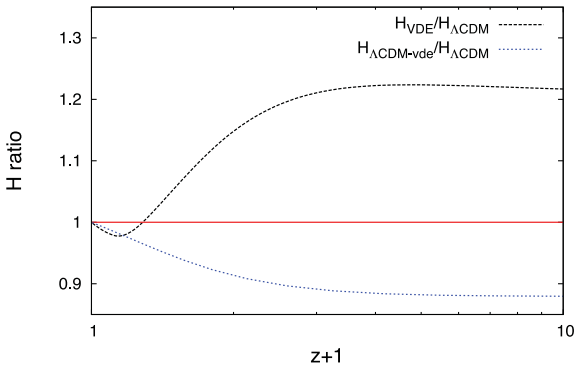

Figure 5. The ratio of the Hubble function $H(a)h^{-1}$ for VDE and ΛCDM-vde to the standard ΛCDM one. At earlier times, VDE undergoes a relatively faster expansion compared to ΛCDM, whereas the opposite is true at smaller z values. On the other hand, ΛCDM-vde cosmology is characterized by a slower relative expansion throughout the whole history of the universe.

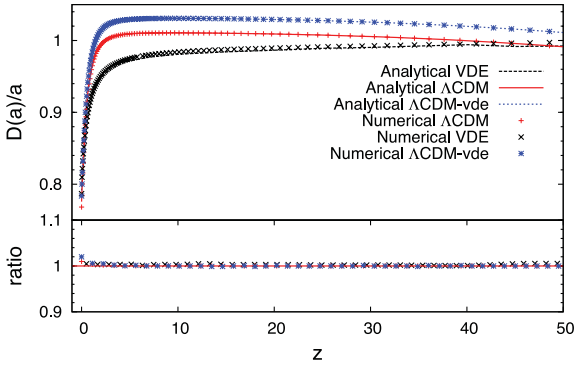

Figure 6. Ratio of the growth function to the expansion factor $D(a)/a$ as obtained from the $500\,h^{-1}$ Mpc box simulations versus the analytical one. The results show an agreement between the theoretical expectation and the numerically computed one within the 2 per cent level. The results from the $1\,h^{-1}$ Gpc box simulations are not shown since they perfectly overlap with the ones presented here.

3.2.1 Initial conditions

To consistently generate the initial conditions for our simulation, first we normalized the perturbation power spectrum depicted in Fig. 4 to the chosen value for σ_8 at $z = 0$. Therefore, we normalized VDE and ΛCDM-vde initial conditions to $\sigma_8 = 0.83$, while for ΛCDM we used the *WMAP*7 value $\sigma_8 = 0.8$. Using the respective linear growth factors, we rescaled the $P(k)$ to the initial redshift $z = 60$, where the particles' initial velocities and positions were computed using the Zeldovich (1970) approximation.

We emphasize here that the main goal of our analysis is to find and highlight the main differences of the VDE picture with respect to the standard one: therefore, the choice of these different normalization parameters has to be understood as unavoidable as long as we want the models under investigation to be *WMAP*7 viable ones. Needless to say, in this regard the ΛCDM-vde cosmology must be considered only as a tool to disentangle parameter-driven effects from the dynamical ones, not being a concurrent cosmological paradigm we want to compare VDE to.

3.2.2 Hubble expansion

As pointed out by Li & Barrow (2011), the expansion history of the universe has a very deep impact on structure formation and in particular the results of an N-body simulation, as it affects directly every single particle through the equations of motion written in comoving coordinates. In Fig. 5, the ratios of the Hubble expansion factors for VDE and ΛCDM-vde to the standard ΛCDM value are shown; we see that different models are characterized by differences up to 20 per cent in the expansion rate. To implement this modification, we replaced the standard computation of $H(a)$ in GADGET-2 with a routine that reads and interpolates from a pre-computed table.

3.3 Code testing

To check the reliability of the modifications introduced into the simulation code and during the generation of the initial conditions, we have confronted the theoretical linear growth factor, computed using the Boltzmann code CAMB (Lewis, Challinor & Lasenby 2000), with the ones derived directly from the simulations.

As shown in Fig. 6, our results yield an agreement within the 1 per cent level, which proves the correctness of our modifications as well as illustrating (again) the differences in structure growth between the models.

We would like to note that for consistency reasons, when calculating both the CAMB and the numerical value for the growth factor, we have used the expression

$$D^{+}(z) = \sqrt{\frac{P(z, k_0)}{P(z_0, k_0)}}\,, \tag{16}$$

where k_0 is a fixed scale within the linear regime and z_0 is the initial redshift of the simulation.

3.4 Halo finding

In order to identify haloes in our simulation, we have run the open source MPI+OpenMP hybrid halo finder AHF[3] described in detail in Knollmann & Knebe (2009). AHF is an improvement of the MHF halo finder (Gill, Knebe & Gibson 2004) and has been extensively compared against practically all other halo-finding methods in Knebe et al. (2011). AHF locates local overdensities in an adaptively smoothed density field as prospective halo centres. For each of these density peaks, the gravitationally bound particles are determined. Only peaks with at least 20 bound particles are considered as haloes and retained for further analysis.

However, the determination of the mass requires a bit more elaboration as it is computed via the equation

$$M(R) = \Delta \times \rho_{\rm c}(z) \times \frac{4\pi}{3} R^3\,, \tag{17}$$

where we applied $\Delta = 200$ as the overdensity threshold and $\rho_{\rm c}(z)$ refers to the critical density of the universe at redshift z. In this way, $M(R)$ is defined as the total mass contained within a radius R, corresponding to the point where the halo matter density $\rho(r)$ is Δ times the critical value $\rho_{\rm c}$. While using this relation particular care has to be taken when considering the definition of the critical density

$$\rho_{\rm c}(z) = \frac{3H^2(z)}{8\pi G} \tag{18}$$

because it involves the Hubble parameter that differs substantially at all redshifts in the two models. This means that, identifying the halo masses, we have to take into account the fact that the value of $\rho_{\rm c}(z)$ changes from ΛCDM to VDE. This has been incorporated into and taken care of in the latest version of AHF where $H_{\rm VDE}(z)$ is being read in from a pre-computed table, too.

We finally need to mention that we checked that the objects obtained by this (virial) definition can be compared across different cosmological models and using different mass definitions. To this extent, we studied the ratio between two times kinetic over potential energy $\eta = 2T/|U|$, confirming that at each redshift under investigation here the distributions of η in ΛCDM and VDE are actually comparable (not presented here though), meaning that the degree of virialization (which should be guaranteed by equation 17) is in fact similar. We therefore conclude that our adopted method to define halo mass (and edge) in the VDE model leads to unbiased results and yields objects in the same state of equilibrium as is the case for the ΛCDM haloes. Please note that this test does not guarantee that all our objects are in fact virialized; it merely assures us that the degree of virialization is equivalent. We will come back to this issue later when selecting only equilibrated objects.

4 LARGE-SCALE STRUCTURE AND GLOBAL PROPERTIES

In the following section, we will discuss the global properties of large-scale structures identified in our simulations. Using all of our sets of simulations for ΛCDM, ΛCDM-vde and VDE, we will disentangle parameter-driven effects from those due to the different dynamics of the background expansion, which uniquely characterize VDE and therefore are worth pointing out in the process of model selection.

4.1 Density distribution

In Fig. 7, we show the colour-coded density field for the particle distribution at redshift $z = 0$, for a $120 \times 120\,h^{-1}$ Mpc^2 slice at the box centre for the three $500\,h^{-1}$ Mpc simulations projected on the x–z plane. As expected, we observe that the most massive structures' spatial positions match in the three simulations, although in the

[3] AHF stands for Amiga Halo Finder, to be downloaded freely from http://www.popia.ft.uam.es/AMIGA

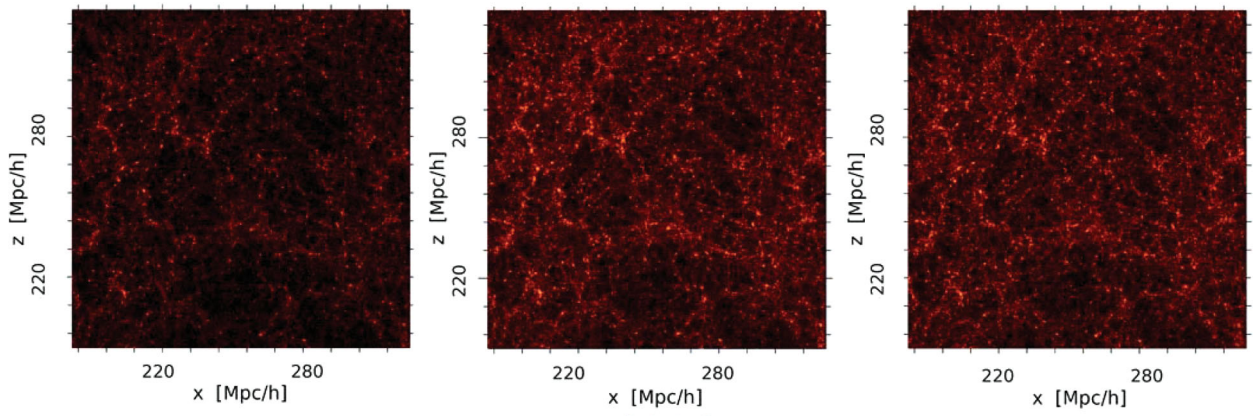

Figure 7. Projected density for ΛCDM, ΛCDM-vde and VDE showing a $120 \times 120\,h^{-2}$ Mpc^2 slice at the box centre in the $500\,h^{-1}$ Mpc box at $z = 0$ projected on the x–z plane. Bright areas are associated with matter, whereas underdense regions are denoted by darker, black spots in the projected box. Results for the VDE-1, ΛCDM-1 and ΛCDM-vde-1 simulations are not shown since the colour coding does not provide useful insights on the different clustering patterns on smaller scales.

ΛCDM-vde and VDE observations we see a large overabundance of objects with respect to ΛCDM, as we could expect due to the higher $\Omega_{\rm M}$. This observation will be confirmed on more quantitative grounds in the analysis carried out in the following sections, especially when referring to the study of the cumulative mass function.

4.2 Matter power spectrum

In Fig. 8, we show the dark matter power spectrum $P(k)$ at redshifts $z = 0$, 1, 3, 4 computed for the VDE-0.5, ΛCDM-0.5 and ΛCDM-vde-0.5 simulations. For clarity, we do not show the $1\,h^{-1}$ Gpc simulations; however, we have checked their consistency with the $500\,h^{-1}$ Mpc runs. We note that at all redshifts the differences already seen in the input power spectra are preserved (cf. Fig. 4), meaning that the VDE model has less power than ΛCDM on the large scales, whereas the opposite is true for small scale. This particular shape of the $P(k)$ is a peculiar feature of VDE cosmology, as other kinds of dynamical quintessence (Alimi et al. 2010) and coupled DE (Baldi et al. 2010) show completely different properties, with less power (in the former case) or a ΛCDM-type of behaviour (in the latter) on small scales. At higher and intermediate redshifts, ΛCDM-vde shows almost no differences from ΛCDM, as expected since the former is normalized to a lower initial value with respect to the latter and therefore needs to equal it before eventually overcoming it at smaller z values, as imposed by the larger σ_8 normalization. The effects of the different growth factor in this model start to become evident only at $z < 1$, where we see that the ratio of the $P(k)$ starts to increase. Whereas the ratio of VDE to ΛCDM for $k < 0.05\,h\,{\rm Mpc}^{-1}$ is substantially unaltered at all redshifts, small scales are affected by non-linear effects, eventually distorting its shape.

4.3 Halo abundance

In the following subsection, we will study the abundance of massive objects at different redshifts. Highlighting the differences arising among the three models in the different mass ranges, we want to study VDE's peculiar predictions for the massive cluster distribution and highlight its distinction from ΛCDM.

To this extent, we compare in Fig. 9 the three different mass functions at $z = 0$ computed for the $1\,h^{-1}$ Gpc simulations versus the ones obtained using the Tinker formula (Tinker et al. 2008). In the ΛCDM and ΛCDM-vde cases, the theoretical values are obtained using the standard parametrization, whereas in the VDE case we performed a non-linear fit of the mass function to the numerical data. We find that in the VDE case the four parameters of the Tinker mass functions take the values (assuming the standard notation) $A = 0.105$, $a = 0.75$, $b = 4.42$ and $c = 1.48$, thus differing substantially from the usual ones (which are $A = 0.187$, $a = 1.47$, $b = 2.57$ and $c = 1.19$). This difference is most likely due to a different value for the linear critical overdensity parameter $\delta_{\rm c}$; however, a complete understanding of this aspect would require a deeper knowledge of the linear perturbation theory in VDE cosmology, which is still under investigation.

In Fig. 10, we show the (cumulative) mass functions for the three models at $z = 0$, 1, 2, 4, as computed from the VDE-0.5, ΛCDM-0.5 and ΛCDM-0.5-vde simulations; the corresponding VDE-1, ΛCDM-1 and ΛCDM-vde-1 results can be found in Carlesi et al. (2011); they are not shown here again as they do not provide any new insights and rather confirm (and extend) the results to be drawn from the $500\,h^{-1}$ Mpc boxes. We note that the VDE cosmology is characterized by a larger number of objects at all the mass scales and redshifts, outnumbering ΛCDM by a factor constantly larger than 2. In particular, this enhancement can be seen for the very large masses, where at low z the VDE/ΛCDM ratio reaches values of $\sim$10. Although this value of the ratio seems to be a mere result of the cosmic variance, due to the low number of haloes found in this mass range, the computation of the mass function for the second $500\,h^{-1}$ Mpc VDE realization and the $1\,h^{-1}$ Gpc simulations makes us believe that the expected enhancement in this region must be at least a factor of 5.

Interestingly enough, ΛCDM-vde has comparable characteristics to VDE, which leads us to the conclusion that the substantial enhancement in structure formation is mainly parameter driven, i.e. due to the overabundance of matter and higher normalization of matter density perturbations. Although this first observation may seem in contrast with what we have found in Section 4.2, where we have noted that VDE has less power on large scales in comparison to ΛCDM, we have to take into account that, in the hierarchical picture of structure formation, objects on small scales form first to subsequently give birth to larger ones. This means, in our case, that more power for large k-values should be regarded as an important

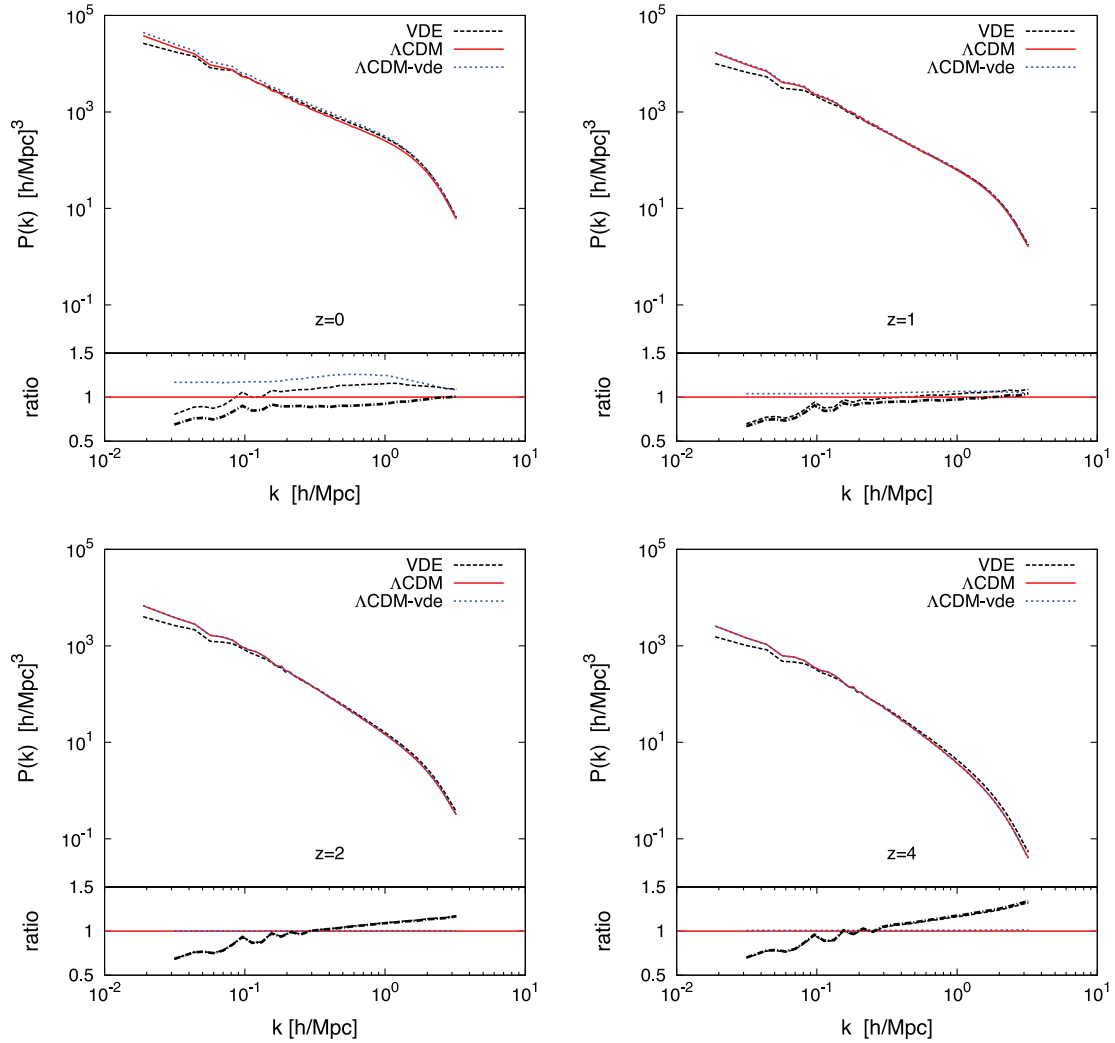

Figure 8. Power spectra at redshifts $z = 0$, 1, 2, 4; solid lines are for ΛCDM-0.5, dotted for ΛCDM-0.5-vde and dashed for VDE-0.5. The results from the $1\,h^{-1}$ Gpc simulations are not shown as they simply overlap with the present ones on the smaller-k end, without providing further insights on the small scales, where we expect non-linear effects to dominate.

source of the overall enhancement together with the overabundance of matter, as already pointed out in the previous discussion. The evolution of the mass functions at different redshift allows us to disentangle the effect of the modified expansion rate; at higher redshift, in fact, both the ΛCDM and ΛCDM-vde mass functions are suppressed with respect to the VDE model, mostly because of the lack of power on small scales. These stronger initial fluctuations eventually trigger the earlier start of structure formation, but – as time passes – the effect of the increased expansion rate shown in Fig. 5 for the VDE cosmology suppresses structure growth, leading to a mass function below the ΛCDM-vde curve at around redshift 1. At this point, the VDE expansion rate starts decreasing with respect to the ΛCDM one, comparatively enhancing very large structure growth and eventually causing the two mass functions to be (nearly) indistinguishable at $z = 0$. In an attempt to disentangle further the effects of the new $\Omega_{\rm M}$ from those due to the higher normalization of the matter power spectrum, we searched for a redshift z_0 at which ΛCDM and VDE have an identical σ_8 value, which would allow us to single out the impact of the different $\Omega_{\rm M}$ parameter alone. Integrating numerically the power spectra of the different simulations' snapshots, we have found $z_0 = 0.18$, where σ_8 is 0.651 for both VDE and ΛCDM. Analysing the power spectra and mass functions at this redshift, we can conclude that the main effects of VDE, such as the overabundance of objects, are only due to the larger $\Omega_{\rm M}$, the impact of the different normalization of the matter fluctuations being practically negligible.

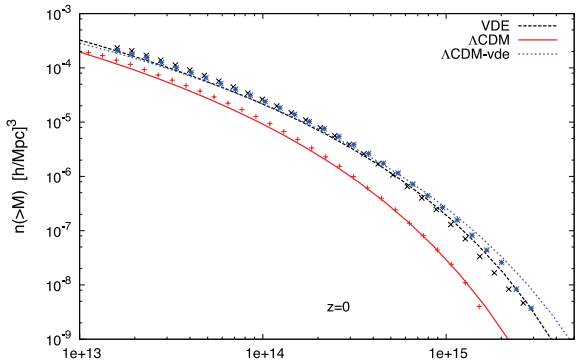

Figure 9. The numerical halo mass function for the three $1\,h^{-1}$ Gpc simulations at $z = 0$, showing the numerical results versus the Tinker theoretical values.

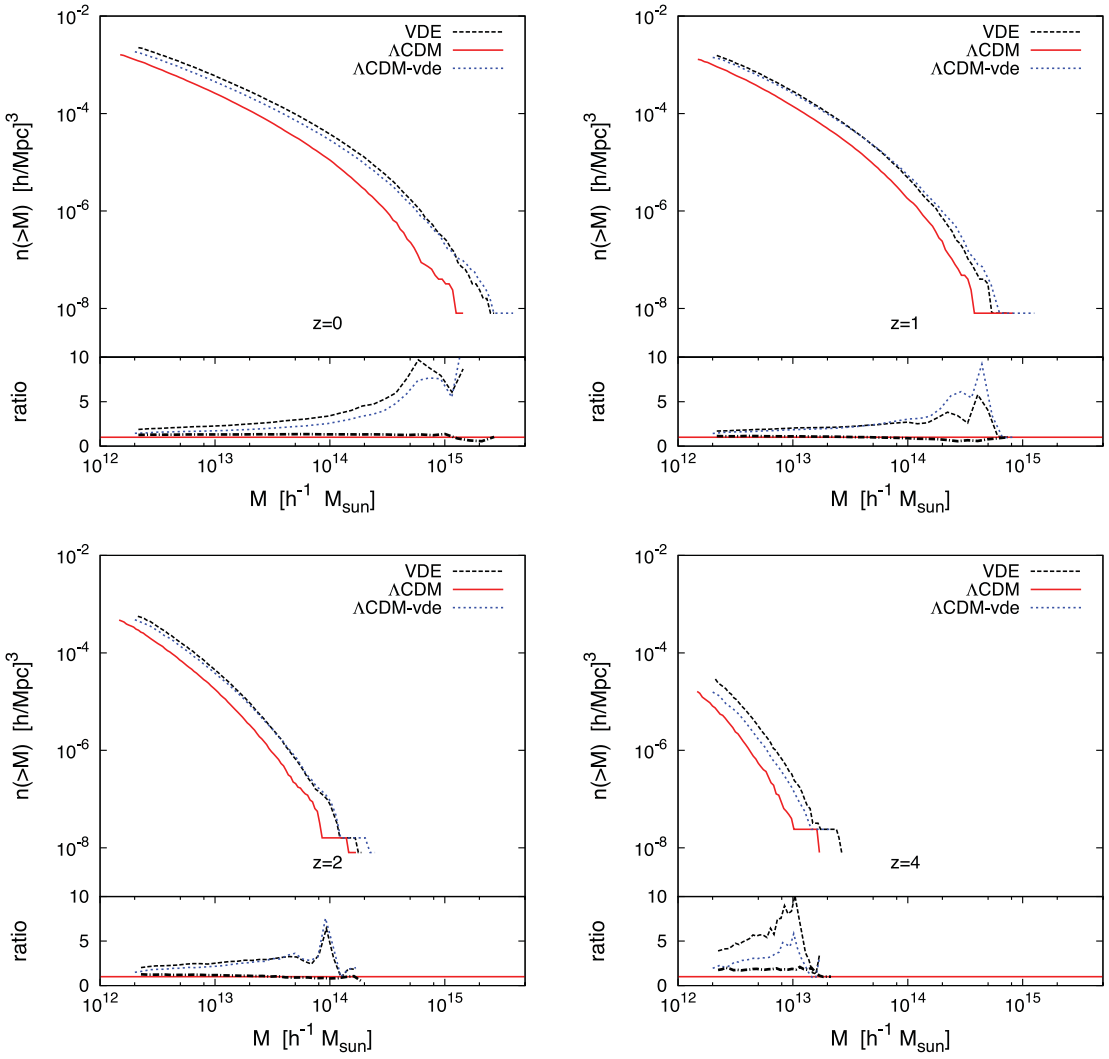

Figure 10. Mass function for ΛCDM(solid lines), VDE (dashed lines) and ΛCDM-vde (dotted lines) models at different redshifts, computed for the $500\,h^{-1}$ Mpc box simulations. We have also verified that the corresponding values computed for the $1\,h^{-1}$ Gpc simulations overlap to the ones shown here for $M > 10^{13}\,h^{-1}\,\mathrm{M}_{\odot}$, except for a smoother high-mass end. In the lower panels of the plots, VDE and ΛCDM-vde to ΛCDM ratios are represented by dotted lines while VDE to ΛCDM-vde are shown using dash-dotted lines.

Furthermore, if we look at Fig. 11, where we show the evolution with redshift of the number density of objects above the $M = 10^{14}\,h^{-1}\,\mathrm{M}_{\odot}$ threshold, we observe that the most massive structures in the two cosmologies form at comparable rates. This seems to suggest that in the VDE picture there is a subtle balance between the formation of new small haloes and their merging into more massive structures. Such an effect comes as no surprise if we again take into account that this model has two main opposite, different features that affect the formation of structures: a strong suppression on all scales induced by the faster expansion of the universe for a large redshift interval and an enhancement due to a higher density of matter and a larger power on the small scales.

An interesting consequence of this kind of behaviour is that the VDE overabundance of massive objects may address some recent observational tensions of ΛCDM, namely the high redshift of reionization and the presence of extremely massive clusters at $z > 1$. Recent microwave background observations seem to prefer a high reionization redshift, around $z \approx 10$ combined with a lower normalization of the matter perturbations, $\sigma_8 \approx 0.8$, whereas

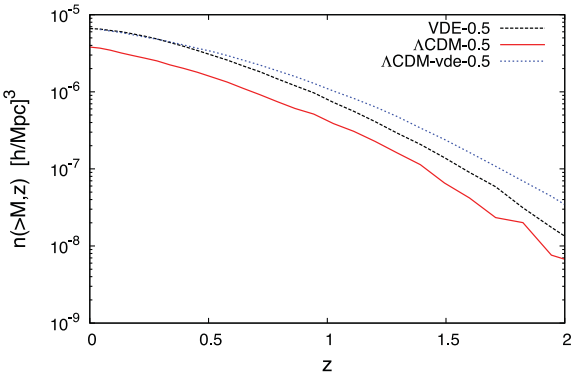

Figure 11. Number density evolution for objects more massive than $10^{14}\,h^{-1}\,\mathrm{M}_{\odot}$ as a function of redshift. The larger amount of massive clusters at higher redshift is a distinctive feature of VDE cosmology.

simulations have shown (see e.g. Raičević, Theuns & Lacey 2011) that early reionization can be achieved only for $\sigma_8 = 0.9$ or larger. In VDE, the appearance of dark matter haloes with masses larger than $10^{12}\,h^{-1}\,\mathrm{M}_\odot$ as early as $z = 7$ (while equivalent structures appear in ΛCDM only for $z > 5$) might imply also a larger $z_{\rm reion}$, provided the hierarchical picture of structure formation holds also in VDE at smaller mass scales. On the other hand, the existence of $M > 5 \times 10^{14}\,h^{-1}\,\mathrm{M}_\odot$ clusters at $z > 1$ (as discussed in Jee et al. 2009; Brodwin et al. 2010; Foley et al. 2011) has also been considered by many authors (e.g. Baldi & Pettorino 2011; Enqvist et al. 2011; Hoyle et al. 2011; Baldi 2012) as a serious challenge to the standard ΛCDM paradigm; for a more thorough discussion of this issue in the context of VDE cosmology, we refer to aforementioned articles as well as Carlesi et al. (2011). However, the comparison to the ΛCDM-vde paradigm, also shown in Fig. 11, shows that VDE indeed acts as a source of suppression of structure growth with respect to the enhancement triggered by the increase in σ_8 and $\Omega_{\rm M}$. This effect is indeed a general result of uncoupled dynamical DE models (Grossi & Springel 2009; Li, Mota & Barrow 2011) as the presence of a larger fraction of DE at high z enhances Hubble expansion (as shown in Fig. 5), preventing a stronger clustering to take place.

In our case, it is also important to point out that the overprediction of objects at $z = 0$ may represent a shortcoming of the model, as observations on the cluster number mass function seem to be in contrast with such a prediction (see Vikhlinin et al. 2009; Wen, Han & Liu 2010; Burenin & Vikhlinin 2012). Furthermore, we have to keep in mind that these results assume a ΛCDM fiducial model, while the use of a different cosmology requires a careful handling of the data and does not allow a straightforward comparison to the observations, as they are affected by model-dependent quantities like comoving volumes and mass–temperature relations.

4.4 Void function

In order to identify voids, our void finder starts with a selection of point-like objects in three dimension. These objects can be haloes above a certain mass or a certain circular velocity or galaxies above a certain luminosity. Thus, the detected voids are characterized by this threshold mass, circular velocity or luminosity. Other void finders use different approaches (Colberg et al. 2008). The void-finding algorithm does not take into account periodic boundary conditions used in numerical simulations. Therefore, we have periodically extended the simulation box by $50\,h^{-1}$ Mpc. In this extended box, we represent all haloes with a mass above the threshold of $5 \times 10^{12}\,h^{-1}\,\mathrm{M}_\odot$ as a point. In this point distribution, we search at first the largest empty sphere which is completely inside the box. To find the other voids, we repeat this procedure, however taking into account the previously found voids. We allow newly detected voids to intersect with previously detected ones up to 25 per cent of the radius.

In Fig. 12, we show the cumulative number of voids with radius larger than $R_{\rm void}$, the centre of which is in the original box. One can clearly see that for a given void radius there exist more voids in the ΛCDM than in the ΛCDM-vde and VDE models. The void distribution reflects the behaviour of the mass function shown in Fig. 10. At redshift $z = 0$, there exist less haloes with $m_{\rm h} > 5 \times 10^{12}\,h^{-1}\,\mathrm{M}_\odot$ in the ΛCDM model than in the other two models. Thus, on average larger voids are expected.

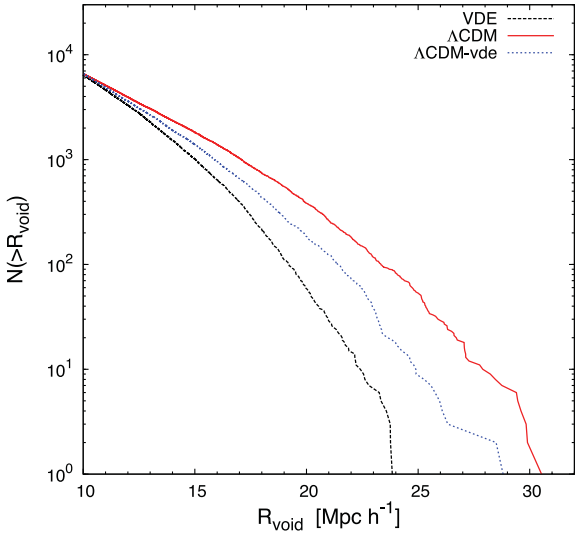

Figure 12. Void function for VDE-0.5, ΛCDM-0.5 and ΛCDM-vde-0.5 at $z = 0$. For the $500\,h^{-1}$ Mpc box, we show the cumulative number of empty spheres of radius R which do not contain any object with mass larger than $5 \times 10^{12}\,h^{-1}\,\mathrm{M}_\odot$.

4.5 Growth index

The growth of the perturbations can be related to the evolution of the matter density parameter by the general relation

$$\Omega_{\rm M}^{\gamma(a)} = \frac{\mathrm{d}\ln(\delta(a))}{\mathrm{d}\ln(a)}\,. \tag{19}$$

In the standard ΛCDM cosmology, the exponent $\gamma(a)$ can be approximated by a constant value $\gamma \sim 0.55$, although a more detailed calculation shows that this number is actually redshift dependent (see Bueno Belloso, García-Bellido & Sapone 2011). In Fig. 13, we show the evolution of this growth index $\gamma(z)$ computed from our VDE-0.5, ΛCDM-vde and ΛCDM-0.5 simulations. As expected, we do observe that in VDE structure formation is generally suppressed with respect to ΛCDM as an effect of the faster expansion rate. This statement is true until $z \approx 1.5$, when the ratio $H_{\rm VDE}/H_{\Lambda\rm CDM}$ starts decreasing, causing the steep increase in the growth index, eventually reducing again as soon as VDE enters into the phantom regime (see Section 2), undergoing an

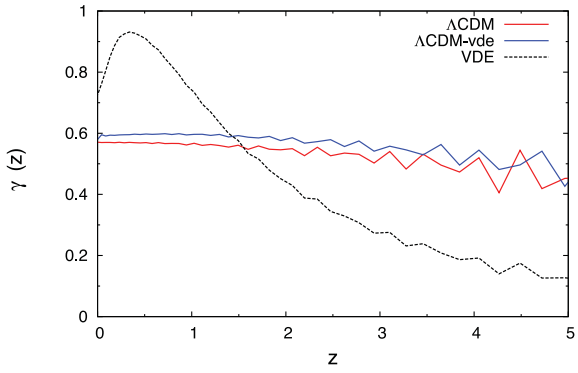

Figure 13. Growth index in the VDE and ΛCDM cosmologies from $z = 5$ to 0. Whereas ΛCDM's growth index has an almost constant behaviour with a mild dependence on the redshift, VDE changes dramatically from a regime where growth is relatively suppressed (until $z \approx 1.5$) to a relative enhancement at earlier times, where γ becomes larger.

accelerated expansion that strongly suppresses structure formation. This latter change, which takes place at $z \approx 0.5$, is reflected by the peak of $\gamma(z)$, which is reached for the same z. Actually, as stressed by different parametrizations (Bueno Belloso et al. 2011), the growth index is extremely sensitive to the value of the equation of state $\omega(z)$, although an explicit form in terms of VDE cosmology still has to be found. Indeed, the extremely different behaviour of this parameter at different redshifts is an interesting feature that clearly distinguishes the two models in a unique way. In fact, parameter-induced modification accounts for an ≈5 per cent change for the value of the growth factor, as the comparison between ΛCDM and ΛCDM-vde suggests. In this case, we observe a slight increase of the value of $\gamma(z)$ at all redshifts, due to the increased growth rate in ΛCDM-vde, also shown in Fig. 6. However, these changes have no impact on the shape of this function, which keeps its mild dependence on z unaltered. Therefore, $\gamma(z)$ can be effectively used as a tool for model selection, embodying effectively VDE's peculiar equation of state $\omega(z)$ and expansion history. Current observational bounds on γ constrain only weakly its value at high z values (see e.g. Nesseris & Perivolaropoulos 2008) or even favour a higher $\gamma(z = 0)$ (Basilakos 2012) in contrast to theoretical calculations based on ΛCDM. In any case, it will surely be something to be looked at in the near future, when deep surveys like *Euclid* (Laureijs et al. 2011) will provide stringent constraints on this quantity (Bueno Belloso et al. 2011).

5 DARK MATTER HALOES

In this section, we will discuss properties of (individual) haloes in VDE and ΛCDM. In particular, we will compare the distributions of masses, shape parameter, spin parameter, concentrations and formation redshifts as well as the shape of dark matter density profiles. In this way, we will determine the most important features that characterize on the average a single cosmological model. In addition, we are also cross-correlating haloes in the two models, studying differences on a one-to-one basis. With this we will be able to determine how the properties of a single given structure change when switching from one cosmological picture to the other.

5.1 General properties

To have a reliable description of the general halo properties, we need to properly select our sample from the catalogues, in order to include only those objects composed of a number of particle sufficient to resolve its internal structure without exceeding statistical uncertainty. Following Muñoz-Cuartas et al. (2011) and Prada et al. (2011), we set this number to approximately 500, even though other authors (see e.g. Bett et al. 2007; Macciò et al. 2007) suggest that lower values can be used, too. However, since we are dealing with different simulation runs with particles of different masses, the application of this criterion is not straightforward. In fact, since our aim is to compare *equivalent* structures (i.e. structures with the same M_{200}) and not structures composed by an identical number of particles, we need to choose our sample imposing a mass threshold $M_{\rm th}$. For the simulations in the $500\,h^{-1}$ Mpc box, we have chosen $M_{\rm th} = 5 \times 10^{13}\,h^{-1}\,{\rm M}_\odot$, which corresponds to haloes formed by at least 500 particles in VDE and ΛCDM-vde and 715 particles in ΛCDM; while for the larger $1000\,h^{-1}$ Mpc runs, we imposed an $M_{\rm th} = 3 \times 10^{14}\,h^{-1}\,{\rm M}_\odot$ limit, i.e. 380 VDE and ΛCDM-vde particles and 545 ΛCDM ones. In the latter set of simulations, we see that we are also including haloes with an ∼20 per cent less than 500 particles in the VDE and ΛCDM-vde cases; this has been done since in the trade-off between resolution and sample size, we have felt more comfortable using a larger number of haloes at the expense of a slight reduction in accuracy, which will be none the less taken into account when analysing the results. The total number of haloes that comply with these conditions in every simulations, as well as the number of haloes that satisfy the relaxation criterion which will be discussed in Section 5.1.3, is shown in Table 2. The state of virialization of haloes will only be taken into account below when investigating the density profiles; for the study of the (distributions of the) two-point correlation functions, the spin and even the shape of haloes, we prefer to include even unrelaxed objects as they should clearly stick out in the distributions (if present in large quantities).

Table 2. Number of haloes above the mass (number) threshold $M_{\rm th}$ ($N_{\rm th}$) per simulation. Also shown is the number of relaxed haloes, defined as those complying with the criterion introduced in Section 5.1.3.

Simulation	$M_{\rm th}$ ($h^{-1}\,{\rm M}_\odot$)	$N_{\rm th}$	$N_{\rm total}$	$N_{\rm relaxed}$
ΛCDM-0.5	5×10^{13}	715	1704	1370
ΛCDM-vde-0.5	5×10^{13}	500	5898	5220
VDE-0.5	5×10^{13}	500	6274	5569
ΛCDM-1	3×10^{14}	545	4045	3533
ΛCDM-vde-1	3×10^{14}	380	9072	8117
VDE-1	3×10^{14}	380	12174	11508

5.1.1 *Correlation function*

To study the clustering properties of the haloes in VDE cosmology, we computed the two-point correlation function using the definition

$$\xi(r) = \frac{V}{N^2} \sum_{i=1}^{N} \frac{n_i(r;\Delta r)}{v(r;\Delta r)} - 1\,, \tag{20}$$

where N is the total number of objects above the given mass threshold in the simulation volume V, and n_i is the total number of objects within a shell of volume v and thickness Δr (of constant logarithmic spacing in r) centred at the ith object. In this case, we have limited our analysis to the $500\,h^{-1}$ Mpc boxes, ignoring the $1\,h^{-1}$ Gpc due to their lack of small-scale resolution. The results are plotted in Fig. 14, where we can see that the $\xi(r)$ is slightly smaller at all scales in VDE. Although in principle we would expect VDE cosmology to have an enhanced clustering pattern due to the increased distribution of massive objects observed in the mass function, the

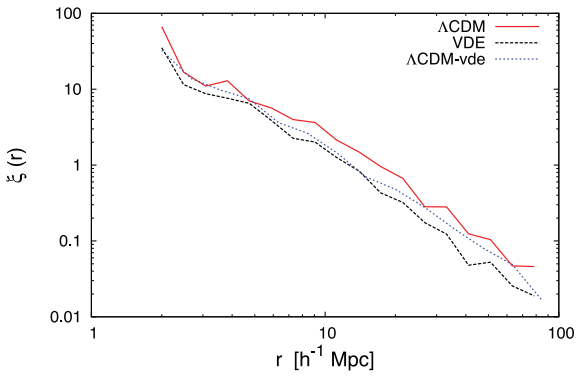

Figure 14. The two-point correlation function for objects more massive than $5 \times 10^{13}\,h^{-1}\,{\rm M}_\odot$ in the $500\,h^{-1}$ Mpc simulations.

Table 3. Best-fitting values for the mass–concentration relation for $z = 0$, obtained by fitting the relation given by equation (30) to the relaxed haloes concentrations and the two-point correlation function to a power law $(r_0/r)^\gamma$ for the ΛCDM, ΛCDM-vde and VDE cosmologies. r_0 values are given in h^{-1} Mpc.

Model	a	b	r_0	γ
ΛCDM	−0.115	2.11	13.4	−1.79
ΛCDM-vde	−0.112	2.21	12.1	−1.91
VDE	−0.098	2.17	10.1	−1.94

N^{-2} dependence of the two-point correlation function drags the total value down, making the final distribution function smaller than in ΛCDM. In fact, a similar behaviour can be observed for ΛCDM-vde, with a two-point correlation function below ΛCDM at practically all scales. In Table 3, we show the results of fitting $\xi(r)$ to a power law $(r_0/r)^\gamma$ from which we see that VDE is characterized by a smaller correlation length r_0 and a steeper slope γ.

5.1.2 Spin parameter, shape and triaxiality

Rotational properties of the haloes can be studied using the so-called spin parameter λ, a dimensionless number that measures the degree of rotational support of the halo. Following Bullock et al. (2001), we define it as

$$\lambda = \frac{L_{200}}{\sqrt{2} M_{200} V_{200} R_{200}}, \tag{21}$$

where the quantities L (the total angular momentum), M (total mass), V (circular velocity) and R (radius) are all taken at the point where the average halo density becomes 200 times the critical density. Different authors have found (e.g. Barnes & Efstathiou 1987; Warren et al. 1992; Cole & Lacey 1996; Bullock et al. 2001; Gardner 2001; Macciò et al. 2007; Macciò, Dutton & van den Bosch 2008; Muñoz-Cuartas et al. 2011) that the distribution of this parameter is of lognormal type:

$$P(\lambda) = \frac{1}{\lambda \sigma_0^2 \sqrt{2\pi}} \exp\left[-\frac{\ln^2(\lambda/\lambda_0)}{2\sigma_0^2}\right], \tag{22}$$

even though there are recent claims that this distribution has to be slightly modified (Bett et al. 2007).

Fitting the above function to our numerical sample by a non-linear Levenberg–Marquardt least-square fit, we find a remarkably good agreement, shown in Fig. 15 for the combined set of haloes of the $500\,h^{-1}$ Mpc and $1\,h^{-1}$ Gpc simulations. It is clear that the three models present no substantial difference in the values of these distributions, meaning that the change of cosmology has no impact on the rotational support of the dark matter structures.

The shape of three-dimensional haloes can be modelled as an ellipsoidal distribution of particles (Jing & Suto 2002; Allgood et al. 2006), characterized by the three axis $a \geq b \geq c$ computed by AHF as the eigenvalues of the inertia tensor

$$I_{i,j} = \sum_n x_{i,n} x_{j,n}, \tag{23}$$

which is in turn obtained by summing over all the coordinates of the particles belonging to the halo.

We define the shape parameter s and the triaxiality parameter T as

$$s = \frac{c}{a}, \qquad T = \frac{a^2 - b^2}{a^2 - c^2}, \tag{24}$$

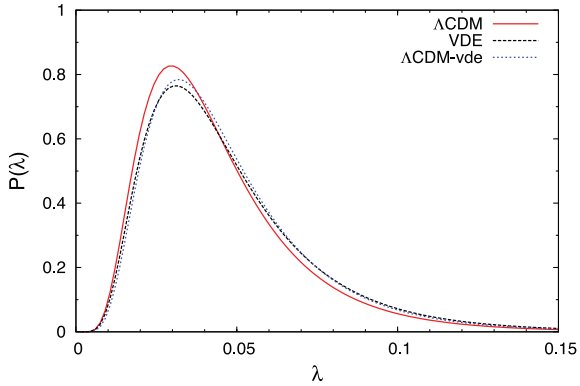

Figure 15. Spin parameter versus the analytical lognormal distribution calculated with the best-fitting parameters. The fit has been performed using the combined sample of haloes above $5 \times 10^{13}\,h^{-1}\,M_\odot$ belonging to the three $500\,h^{-1}$ Mpc boxes, with those above the $3 \times 10^{14}\,h^{-1}\,M_\odot$ limit in the $1\,h^{-1}$ Gpc boxes.

and we calculate the probability distributions $P(T)$ and $P(s)$ of the above parameters for all the objects above the aforementioned mass thresholds in our cosmological simulations to see whether the VDE picture of structure formation induces changes in the average shape and triaxiality. Similar to the previous case, we found again that halo shapes and triaxialities remain practically unaltered by VDE cosmology. This result could be expected, keeping in mind that VDE only affects background evolution. Once that structures start to form, detaching from the background evolution, they become affected by gravitational attraction only. Therefore, the internal structure of dark matter haloes remains generally unaltered by the presence of an uninteracting form of DE and cannot be used to discriminate between alternative cosmological paradigms. We have also verified that these results also hold when taking into account different halo samples separately, i.e. the massive ones of the $1\,h^{-1}$ Gpc simulations and the smaller ones belonging to the $500\,h^{-1}$ Mpc boxes.

5.1.3 Unrelaxed haloes

Before moving to the discussion of the properties of internal structure of the haloes, and in particular the density profile, we need to introduce and motivate a second criterion of selection for our halo sample, related to the degree of *relaxation* of the halo. An additional check is necessary since only a fraction of the structures identified in our catalogues completely satisfies the virial condition. In unvirialized structures, infalling matter and merger phenomena may occur, heavily affecting the halo shape and thus making the determination of radial density profiles and concentrations unreliable. In fact, unrelaxed haloes are most likely to differ from an idealized spherical or ellipsoidal shape since they have a highly asymmetric matter distribution, which in turn makes the determination of the halo centre an ill-defined problem, as discussed by Macciò et al. (2007) and Muñoz-Cuartas et al. (2011). Our halo finder AHF does not directly discriminate between virialized and unvirialized structures, giving catalogues containing both types of objects; however, it provides kinetic K and potential energy U for every halo identified, thus making the computation of the viral ratio $2K/|U|$ straightforward. Following one of the criteria used by Prada et al. (2011), we will consider as relaxed all the haloes satisfying the condition

$$\frac{2K}{|U|} - 1 < 0.5, \tag{25}$$

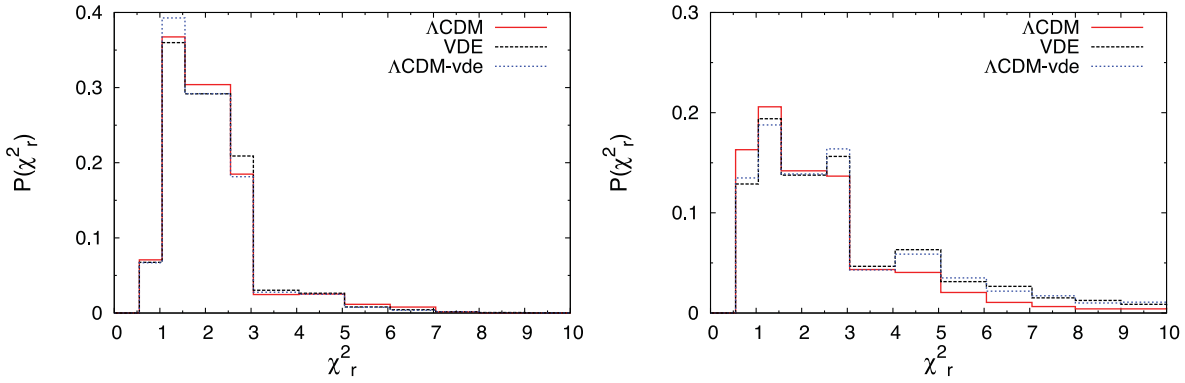

Figure 16. Reduced χ^2 distribution for the best fit to an NFW profile. On the vertical axis we plot the total fraction of haloes whose reduced χ^2 falls within the horizontal axis bin value. This is shown for relaxed haloes above the $5 \times 10^{13}\,h^{-1}\,\mathrm{M}_\odot$ threshold belonging to the VDE-0.5, ΛCDM-vde-0.5 and ΛCDM-0.5 simulations (left-hand panel) as well as for those above the $3 \times 10^{14}\,h^{-1}\,\mathrm{M}_\odot$ threshold belonging to VDE-1, ΛCDM-vde-1 and ΛCDM-1 (right-hand panel). The distributions show no particular difference among the three cosmologies; however, in the three $1\,h^{-1}$ Gpc simulations we note how lower resolution affects the χ^2 distribution, resulting in a thicker tail at higher values compared to the $500\,h^{-1}$ Mpc case, meaning that the fit to an NFW is on average worse.

without introducing additional parameters. Alternative ways of identifying unrelaxed structures can be found throughout the literature (e.g. Bett et al. 2007; Macciò et al. 2007; Neto et al. 2007; Knebe & Power 2008; Muñoz-Cuartas et al. 2011; Prada et al. 2011; Power, Knebe & Knollmann 2012), but since the results they give are qualitatively similar for reasons of computational speed and simplicity, we will not make use of them. The total number of haloes satisfying the relaxation condition is shown for every cosmology in Table 2.

5.1.4 *Density profiles*

N-body simulations have shown that dark matter haloes can be described by a Navarro–Frenk–White (NFW) profile (Navarro, Frenk & White 1996), which is given by

$$\rho(r) = \frac{\rho_0}{\frac{r}{r_\mathrm{s}}(1+\frac{r}{r_\mathrm{s}})^2}\,, \tag{26}$$

where the r_s, the so-called scale radius, and the ρ_0 are in principle two free parameters that depend on the particular halo structure. However, ρ_0 can be written as a function of the critical density as $\rho_0 = \delta_\mathrm{c}\rho_\mathrm{c}$, where

$$\delta_\mathrm{c} = \frac{200}{3}\,\frac{c^3}{\log(1+c) - \frac{c}{1+c}}\,,$$

and $c = r_\mathrm{vir}/r_\mathrm{s}$ is the *concentration* of the halo relating the virial radius $r_\mathrm{v}(=r_{200}$ in our case) to the scale radius r_s, which will be discussed in detail in the following subsection. This description is generally valid for ΛCDM, but simulations of ever increased resolution have actually revealed that the very central regions are not following the slope advocated by the NFW formula but rather follow a Sérsic or Einasto profile (cf. Navarro et al. 2004; Stadel et al. 2009).

Here we want to check to which degree the modified cosmological background affects the distribution of matter inside dark matter haloes, i.e. its density profile. All our (relaxed) objects in all the simulations have been fitted to equation (26), and to estimate the goodness of this fit we compute for each halo its corresponding χ^2, defined in the usual way:

$$\chi^2 = \sum_i \frac{\left(\rho_i^{(\mathrm{th})} - \rho_i^{(\mathrm{num})}\right)^2}{\Delta\rho_i^{(\mathrm{num})}}\,, \tag{27}$$

where the ρ_i are the numerical and theoretical overdensities in units of the critical density ρ_c at the ith radial bin and $\Delta\rho_i$ is the numerical Poissonian error on the numerical estimate. Since different halo profiles will be in general described by a different number of radial bins,[4] to make our comparison between different simulations and haloes consistent we need to use the reduced χ^2:

$$\chi^2_\mathrm{red} = \frac{\chi^2}{N_\mathrm{pts} - N_\mathrm{dof} - 1}\,, \tag{28}$$

where N_pts is the total number of points used (i.e. total number of radial bins) and N_dof is the number of degrees of freedom (free parameters).

The comparison of the distributions of the reduced χ^2 values for ΛCDM-vde, ΛCDM and VDE haloes belonging to the two set of $500\,h^{-1}$ Mpc and $1\,h^{-1}$ Gpc simulations, shown in Fig. 16, allows us to determine again that no substantial difference is induced by the VDE picture, for the same reasons discussed in the case of spin, shape and triaxiality distributions. The standard description of dark matter structures is thus not affected by the presence of a VDE.

5.1.5 *Halo concentrations*

In the last step of the analysis of the general properties of haloes, we will turn to concentrations, which characterize the halo inner density compared to the outer part. This parameter is usually defined as

$$c = \frac{r_\mathrm{vir}}{r_\mathrm{s}}\,, \tag{29}$$

where r_s is the previously introduced scale radius, obtained through the best-fitting procedure of the density distribution to an NFW profile. We would like to remind that concentrations are correlated to the formation time of the halo, since structures that collapsed earlier tend to have a more compact centre due to the fact that it has more time to accrete matter from the outer parts. Dynamical DE cosmologies generically imply larger c values as a consequence of earlier structure formation, as found in works like those by Dolag et al. (2004), Bartelmann, Doran & Wetterich (2006) and Grossi & Springel (2009). In fact, since the presence of early DE usually

[4] Note that our halo finder AHF uses logarithmically spaced radial bins whose number depends on the halo mass, i.e. more massive haloes will be covered with more bins.

suppresses structure growth, in order to reproduce current observations we need to trigger an earlier start of the formation process, which on average yields a higher value for the halo concentrations. However, this result does not hold in the case of coupled DE, where the increased clustering strength induced by a fifth force sets a later start of structure formation, as discussed in Baldi et al. (2010).

In the hierarchical picture of structure formation, concentrations are usually inversely correlated to the halo mass as more massive objects form later; *N*-body simulations (Dolag et al. 2004; Muñoz-Cuartas et al. 2011; Prada et al. 2011) and observations (Comerford & Natarajan 2007; Okabe et al. 2010; Sereno & Zitrin 2012) have in fact shown that the relation between the two quantities can be written as a power law of the form

$$\log c = a(z) \log \left(\frac{M_{200}}{h^{-1}\,\mathrm{M}_\odot} \right) + b(z)\,, \tag{30}$$

where $a(z)$ and $b(z)$ can have explicit parametrizations as functions of redshift and cosmology (see e.g. Neto et al. 2007; Muñoz-Cuartas et al. 2011; Prada et al. 2011). We can use our selected halo samples at $z = 0$ from the $500\,h^{-1}$ Mpc and $1\,h^{-1}$ Gpc simulations to obtain the $a(z = 0)$ and $b(z = 0)$ values for the ΛCDM, ΛCDM-vde and VDE cosmologies; the results of the best-fitting procedure to equation (30) are shown in Table 3.

These values are in good agreement with the ones found, for instance, by Dolag et al. (2004), Macciò et al. (2008) and Muñoz-Cuartas et al. (2011) [who quote for ΛCDM values of $a(z = 0) \approx -0.097$ and $b \approx 2.01$]; the ∼10 per cent discrepancy observed with their results is due to the fact that our results are obtained over a smaller mass range, 5×10^{13}–$2 \times 10^{15}\,h^{-1}\,\mathrm{M}_\odot$, whereas the previously cited works study it over an interval larger by more than three orders of magnitude, 10^{10}–$10^{15}\,h^{-1}\,\mathrm{M}_\odot$. Still, according to our results, the *c*–*M* relation for both the VDE and ΛCDM-vde cases is characterized by a shallower a exponent and a larger b. Although the magnitude of these changes is different in the two models, we can safely conclude that also in this case the results are mainly parameter driven, i.e. due to the larger value of Ω_M. Furthermore, the large error bars for $M > 10^{15}\,h^{-1}\,\mathrm{M}_\odot$ scales, due to the low statistics of massive haloes complying the relaxation requirements, make it difficult to determine to what extent the differences in the best-fitting relations among ΛCDM-vde and VDE could be eventually reduced in the presence of a larger sample.

We also need to mention that in our simulations the actual halo concentrations do not precisely follow equation (30) but rather scatter around it, as can be seen in Fig. 17, where the average c per mass bin is plotted against the corresponding best-fitting relations. This is not really surprising, since observations (Sereno & Zitrin 2012) and *N*-body simulations (Dolag et al. 2004) have shown that halo concentrations are lognormally distributed around their theoretical value calculated using equation (30). In Fig. 18, we show that this is indeed the case: the distribution of the $c(M)/c_\mathrm{fit}(M)$, where $c_\mathrm{fit}(M)$ is the theoretical concentration value for a halo of mass M, is extremely close to a lognormal one with an almost model-independent dispersion, $\sigma \approx 0.4$.

5.2 Cross-correlation

The next step in our analysis consists of studying the properties of the (most massive) cross-correlated objects found in the three models at $z = 0$. Whereas in the previous section our focus was on the distribution of halo properties, this time we aim at understanding how they change switching from one model to another.

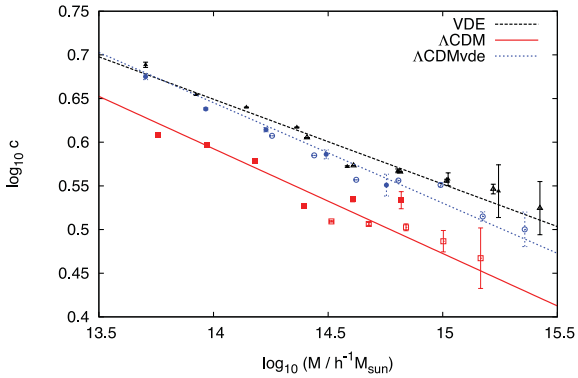

Figure 17. Best fit of the mass–concentration relation for the combined sample of relaxed haloes belonging to all the ΛCDM, ΛCDM-vde and VDE simulations. The points represent the average concentration values for the relaxed haloes in the corresponding mass bin; circles are for ΛCDM, triangles for ΛCDM-vde and squares for VDE. Empty dots stand for bins determined using haloes belonging to the $1\,h^{-1}$ Gpc simulations, while filled ones refer to the $500\,h^{-1}$ Mpc ones. The Poissonian error bars are computed using the number of selected haloes within each mass bin.

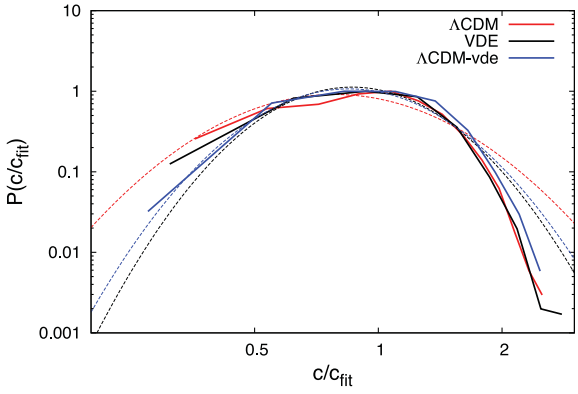

Figure 18. Distribution of the ratio between the actual concentration and the expected one (cf. equation 30) and its fit to a lognormal distribution.

The identification of 'sister haloes' among the different cosmologies can be done using the AHF tool `MergerTree`, which determines correlated structures by matching individual particles IDs in different simulation snapshots. For a more elaborate discussion of its mode of operation, we refer the reader to section 2.4 in Libeskind et al. (2010), where it has been described in greater detail. This time we decided to restrict our halo sample further by only picking the first 1000 most massive (ΛCDM) haloes. The criterion of halo relaxation has of course also been taken into account when dealing with profiles and concentrations.

5.2.1 *Mass and spin parameter*

In the two upper panels of Fig. 19, we show the ratios of the masses M and spin parameter λ for all the cross-correlated sets of simulations; in each panel we show the ratios for the $500\,h^{-1}$ Mpc simulation boxes and the $1\,h^{-1}$ Gpc ones. Both VDE and ΛCDM-vde show average mass and spin values scattered around values larger than 1 when compared to ΛCDM, whereas the cross-comparison of VDE to ΛCDM-vde shows average ratios close to unity at all mass scales. This substantial increase in the ratios is due to the earlier beginning of structure formation, triggered by the larger Ω_M and σ_8, as the comparison VDE/ΛCDM-vde shows. As we already did in

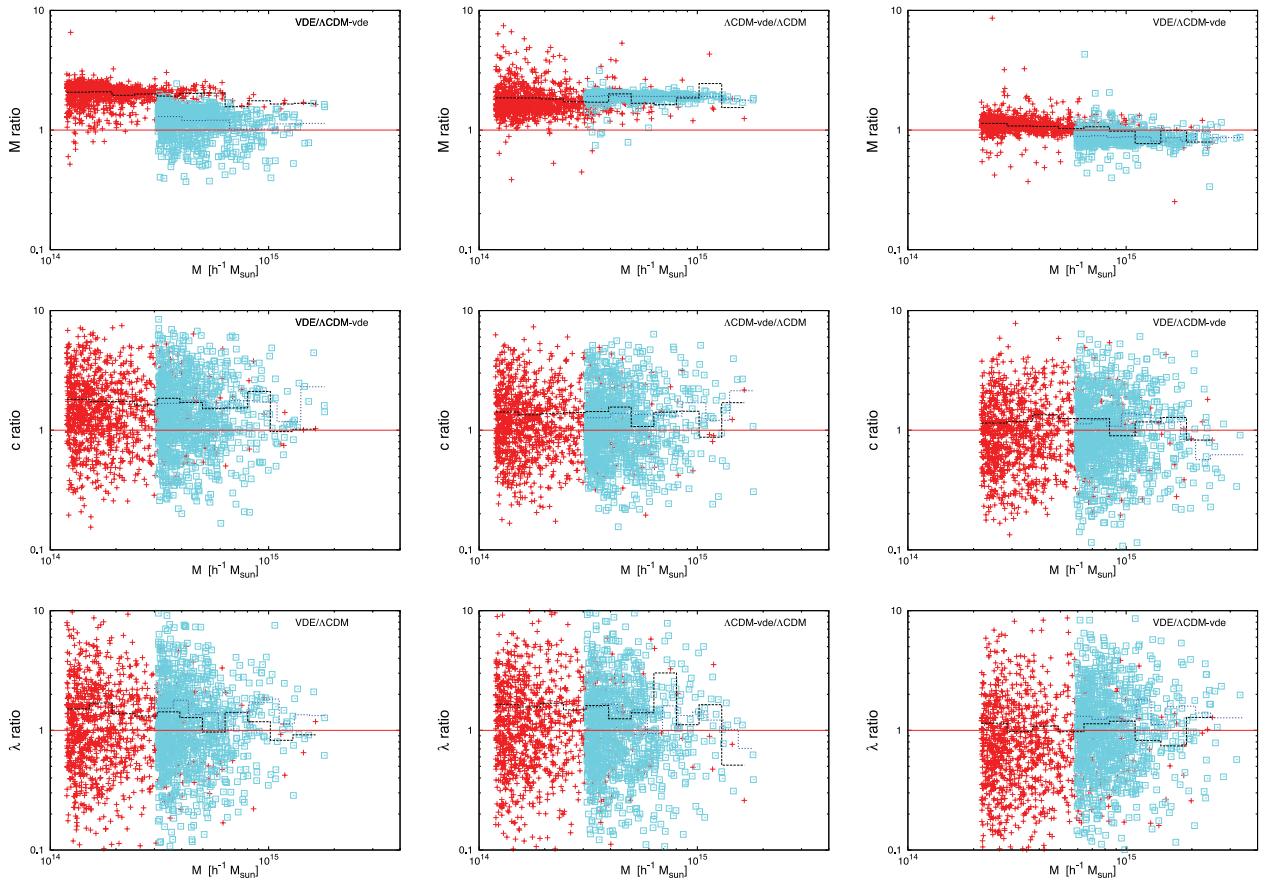

Figure 19. Mass and spin parameter correlation ratios for the first 1000 (relaxed and possibly unrelaxed) haloes. Panels on the left show the VDE/ΛCDM results and the ones in the centre show the ΛCDM-vde/ΛCDM results, while on the right the ratio VDE/ΛCDM-vde is plotted. Cross-identified objects are characterized by larger masses in VDE and ΛCDM-vde as a consequence of the higher $\Omega_{\rm M}$ and σ_8 normalization value.

Section 5.1 when looking at the halo properties in general, we also conclude that when observing the same halo evolved under different cosmologies, the main effects are determined exclusively by the set of cosmological parameters chosen, the imprint of the cosmological background evolution being substantially negligible in this case. This makes the identification of a cosmic vector through the determination of halo properties impossible, since the background dynamics, which distinguishes VDE from any other non-interacting dynamical DE model, does not leave any observable imprint on these scales.

5.2.2 *Halo concentrations and internal structure*

As done in the previous section, in the determination of halo profiles and concentrations properties we discard unrelaxed haloes, but this time in a way so that our halo sample will still be composed of the first 1000 haloes satisfying condition given by equation (25). This same halo sample has also been used in the study of the $M_{\rm vir}$–$z_{\rm form}$, in order to be able to compare these results with the those obtained from concentrations consistently – although in principle formation redshifts are well defined even for unrelaxed haloes. Again, our procedure consists in fitting all the selected structure to an NFW profile, from which we will be able to derive the concentration parameter c and a measure for the quality of the fit χ^2; we will then compare these results in each cross-identified objects to see how a given halo structure changes when evolved under a different cosmology. Although not shown here, no particular trend in the differences among ΛCDM, ΛCDM-vde and VDE pictures has been found for either NFW χ^2, shape or triaxiality, since in all the cases the ratios of these properties among cross-correlated haloes are centred around unity. Not surprisingly, we also find again a generally higher average value for the concentrations in VDE and ΛCDM-vde with respect to ΛCDM (see Fig. 19), a result which again can be explained by the larger value of $\Omega_{\rm M}$ and σ_8. Similar concentrations for VDE and ΛCDM-vde haloes, shown in the upper right-hand panel of Fig. 19, can also be understood as a consequences of the similar masses of the haloes examined and the similar *c*–*M* relations found for the two cosmologies. However, even if from ΛCDM-vde cosmology we conclude that the different choice of $\Omega_{\rm M}$ can explain in this case higher halo concentration, we need to remind that such a result is also a general feature of the dynamical nature of the DE fluid, as already found by Dolag et al. (2004), Bartelmann et al. (2006) and Grossi & Springel (2009).

6 CONCLUSIONS

In this work, we presented an in-depth analysis of the results of a series of *N*-body dark matter only simulations of the VDE cosmology proposed by Beltrán Jiménez & Maroto (2008). The main emphasis has been on the comparison to the standard ΛCDM paradigm, using a mirror simulation with identical number of particles, random seed for the initial conditions, box size and starting redshift. An additional series of simulations for a ΛCDM-vde cosmology has also been run using the VDE values for $\Omega_{\rm M}$ and σ_8 within a standard

ΛCDM picture, to disentangle the effects of the parameter-induced modifications from the dynamical ones coming directly from the VDE model.

The use of a modified version of the GADGET-2 code required us to check the results with particular care. A consistency check of our simulations was performed by comparing the numerical results for the evolution of the growth factor to the analytical calculations, finding an excellent agreement between the two. We further had to adapt the halo-finding procedure, due to the fact that the critical density as a function of redshift $\rho_c(z)$, entering the definition of the halo edges, takes different values in VDE. Once halo catalogues had been obtained, we carried out our analysis at two different levels, namely

(i) we studied the very large-scale clustering pattern through the computation of matter power spectra, mass, void and two-point correlation functions and

(ii) we analysed halo structure, comparing statistical distributions and averages of spin parameters, concentrations, masses and shapes.

In the first point, making use of the full set of simulations, our analysis covered the whole masse range 10^{12}–$10^{15}\,h^{-1}\,\mathrm{M}_\odot$ as well as different redshifts, so that we could make specific VDE model predictions for the number density evolution $n(>M, z)$ and growth index $\gamma(z)$. A distinctive behaviour, very far from the standard ΛCDM results, has been found for $\gamma(z)$ and, in particular, for the mass function that in VDE cosmology can be up to 10 times larger than the standard ΛCDM one. The latter result is due to the earlier onset of structure formation, and we have mentioned how it can be used to address current ΛCDM observational tensions with large clusters at $z > 1$ and possibly with early reionization epoch (cf. also Carlesi et al. 2011). At $z = 0$, we have shown that VDE cosmology requires the standard set of parameters entering the Tinker mass function to be modified; however, since the investigation of the linear perturbation theory is still ongoing, we lack the instruments to shed more light on this aspect.

Computing the cumulative mass function at different redshifts and making use of the ΛCDM-vde simulations, we have also observed how the condition $H_{\mathrm{VDE}}(z) > H_{\Lambda\mathrm{CDM}}(z)$, holding up to $z \approx 1$, induces a relative suppression of structure growth in this cosmological model, an effect that clashes with the increased matter density and σ_8. In fact, while on the one hand higher values of these parameters enhance the formation of a larger number of objects, on the other hand background dynamics suppresses clustering and growth. The interplay and relative size of these effects have been studied using the ΛCDM-vde simulations, showing that, for example, faster expansion in the past determines for VDE an expectation of clusters with $M > 10^{14}\,h^{-1}\,\mathrm{M}_\odot$ up to approximately five times smaller than what a simple increase in σ_8 and Ω_M would determine. This effect has been also seen in the void distribution, where suppression of clustering prevents small structures to merge into larger one and to rather spread in the field, so that underdense regions happen to be smaller and rarer than in ΛCDM and ΛCDM-vde. In these latter cosmologies, in fact, a higher contrast between populated and less populated regions is observed both in the power spectrum and in the colour-coded matter density.

In the second part of our work, we have focused on the study of internal halo structure. We found that VDE cosmology does not induce deviations in the functional form of the dark matter halo density profiles, which are still well described by an NFW (Navarro et al. 1996) profile, nor in the distributions for the concentrations and spin parameters, which are of the lognormal type as in ΛCDM. Shape and triaxiality are also unaffected: the distributions for the relative parameters are identical and peaked at the same values in all the three cosmologies. The above results are a direct consequence of the fact that dark matter haloes, once detached from the general background evolution driven by the cosmic vector, evolve by means of gravitational attraction only, which is unaffected by the specific nature of DE. A net effect can be seen in masses, whose average values tend to be larger than in the ΛCDM case by a factor of $\approx$2, a straightforward consequence of the larger Ω_M and σ_8, as can be shown by a direct comparison of VDE to ΛCDM-vde results, which turn out extremely close in these cases. On the other hand, the different background evolution seems to affect *c–M* relations only slightly, changing the power-law index $a(z)$ and normalization $b(z)$ by 15 per cent. In this case, we have also found that these values in general agree with previous results from early DE studies such as those by Dolag et al. (2004), even though in this case it would certainly be necessary to test the relation down to smaller mass scales, where a better tuning of the parameter would also be possible, and with a larger statistics on the higher scales. However, in general, most of the halo-level effects which seem to characterize VDE can be simply explained in terms of the different cosmological parameters, as we did comparing these results to the outcomes of ΛCDM-vde simulations. For the first time then, through the results of the series of *N*-body simulations, we have shown that VDE cosmology provides a viable environment for structure formation, also alleviating some observational tensions emerging with ΛCDM. We have seen how the peculiar dynamics of this model leaves its imprint on structure formation and growth, and in particular how it affects predictions for large-scale clustering and halo properties. However, a close comparison of the deep non-linear regime results with different sets of observational data still needs to be performed, challenging us to improve the accuracy of our simulations and at the same time devise new and reliable tests which may shed some light not only on VDE but also on the nature of DE in general.

ACKNOWLEDGMENTS

We would like to thank Juan García-Bellido for his interesting suggestions and discussions. EC is supported by the MareNostrum project funded by the Spanish Ministerio de Ciencia e Innovacion (MICINN) under grant no. AYA2009-13875-C03-02 and MultiDark Consolider project under grant CSD2009-00064. AK acknowledges support by the MICINN's Ramon y Cajal programme as well as the grants AYA 2009-13875-C03-02, AYA2009-12792-C03-03, CSD2009-00064 and CAM S2009/ESP-1496. GY would like to thank the MICINN for financial support under grants AYA 2009-13875-C03 and FPA 2009-08958, and the SyeC Consolider project CSD2007-00050. JBJ is supported by the Ministerio de Educación under the postdoctoral contract EX2009-0305 and also wishes to acknowledge support from the Norwegian Research Council under the YGGDRASIL programme 2009–2010 and the NILS mobility project grant UCM-EEA-ABEL-03-2010. We also acknowledge support from MICINN (Spain) project numbers FIS 2008-01323, FPA 2008-00592, CAM/UCM 910309 and FIS2011-23000. The simulations used in this work were performed in the MareNostrum supercomputer at Barcelona Supercomputing Center (BSC).

REFERENCES

Abazajian K. N. et al., 2009, ApJS, 182, 543

Alimi J.-M., Füzfa A., Boucher V., Rasera Y., Courtin J., Corasaniti P.-S., 2010, MNRAS, 401, 775

Allgood B., Flores R. A., Primack J. R., Kravtsov A. V., Wechsler R. H., Faltenbacher A., Bullock J. S., 2006, MNRAS, 367, 1781
Baldi M., 2012, MNRAS, 420, 430
Baldi M., Pettorino V., 2011, MNRAS, 412, L1
Baldi M., Pettorino V., Robbers G., Springel V., 2010, MNRAS, 403, 1684
Barnes J., Efstathiou G., 1987, ApJ, 319, 575
Bartelmann M., Doran M., Wetterich C., 2006, A&A, 454, 27
Basilakos S., 2012, preprint (arXiv:1202.1637)
Beltrán Jiménez J., Maroto A. L., 2008, Phys. Rev. D, 78, 063005
Beltrán Jiménez J., Lazkoz R., Maroto A. L., 2009, Phys. Rev. D, 80, 023004
Bett P., Eke V., Frenk C. S., Jenkins A., Helly J., Navarro J., 2007, MNRAS, 376, 215
Beutler F. et al., 2011, MNRAS, 416, 3017
Brodwin M. et al., 2010, ApJ, 721, 90
Bueno Belloso A., García-Bellido J., Sapone D., 2011, J. Cosmol. Astropart. Phys., 10, 10
Bullock J. S., Dekel A., Kolatt T. S., Kravtsov A. V., Klypin A. A., Porciani C., Primack J. R., 2001, ApJ, 555, 240
Burenin R. A., Vikhlinin A. A., 2012, preprint (arXiv:1202.2889)
Carlesi E., Knebe A., Yepes G., Gottlöber S., Jiménez J. B., Maroto A. L., 2011, MNRAS, 418, 2715
Colberg J. M. et al., 2008, MNRAS, 387, 933
Cole S., Lacey C., 1996, MNRAS, 281, 716
Comerford J. M., Natarajan P., 2007, MNRAS, 379, 190
Dolag K., Bartelmann M., Moscardini L., Perrotta F., Baccigalupi C., Meneghetti M., Tormen G., 2004, Modern Phys. Lett. A, 19, 1079
Enqvist K., Hotchkiss S., Taanila O., 2011, J. Cosmol. Astropart. Phys., 4, 17
Foley R. et al., 2011, ApJ, 731, 86
Gardner J. P., 2001, ApJ, 557, 616
Gill S. P. D., Knebe A., Gibson B. K., 2004, MNRAS, 351, 399
Grossi M., Springel V., 2009, MNRAS, 394, 1559
Guy J. et al., 2010, A&A, 523, A7
Hoyle B., Jimenez R., Verde L., 2011, Phys. Rev. D, 83, 103502
Huterer D., 2010, Gen. Relativ. Gravitation, 42, 2177
Jee M. et al., 2009, ApJ, 704, 672
Jimenez J. B., Maroto A. L., 2009, in AIP Conf. Proc. Vol. 1122, Physics and Mathematics of Gravitation. Am. Inst. Phys., New York, p. 107
Jing Y. P., Suto Y., 2002, ApJ, 574, 538
Knebe A., Power C., 2008, ApJ, 678, 621
Knebe A. et al., 2011, MNRAS, 415, 2293
Knollmann S. R., Knebe A., 2009, ApJS, 182, 608
Larson D. et al., 2011, ApJS, 192, 16
Laureijs R. et al., 2011, preprint (arXiv:1110.3193)
Lewis A., Challinor A., Lasenby A., 2000, ApJ, 538, 473
Li B., Barrow J. D., 2011, MNRAS, 413, 262
Li B., Mota D. F., Barrow J. D., 2011, ApJ, 728, 109
Libeskind N. I., Yepes G., Knebe A., Gottlöber S., Hoffman Y., Knollmann S. R., 2010, MNRAS, 401, 1889
Macciò A. V., Dutton A. A., van den Bosch F. C., Moore B., Potter D., Stadel J., 2007, MNRAS, 378, 55
Macciò A. V., Dutton A. A., van den Bosch F. C., 2008, MNRAS, 391, 1940
Muñoz-Cuartas J. C., Macciò A. V., Gottlöber S., Dutton A. A., 2011, MNRAS, 411, 584
Navarro J. F., Frenk C. S., White S. D. M., 1996, ApJ, 462, 563
Navarro J. F. et al., 2004, MNRAS, 349, 1039
Nesseris S., Perivolaropoulos L., 2008, Phys. Rev. D, 77, 023504
Neto A. F. et al., 2007, MNRAS, 381, 1450
Okabe N., Takada M., Umetsu K., Futamase T., Smith G. P., 2010, PASJ, 62, 811
Perlmutter S. et al., 1999, ApJ, 517, 565
Power C., Knebe A., Knollmann S. R., 2012, MNRAS, 419, 1576
Prada F., Klypin A. A., Cuesta A. J., Betancort-Rijo J. E., Primack J., 2011, preprint (arXiv:1104.5130)
Raičević M., Theuns T., Lacey C., 2011, MNRAS, 410, 775
Riess A. G. et al., 1998, AJ, 116, 1009
Sereno M., Zitrin A., 2012, MNRAS, 419, 3280
Sherwin B. D. et al., 2011, Phys. Rev. Lett., 107, 021302
Springel V., 2005, MNRAS, 364, 1105
Stadel J., Potter D., Moore B., Diemand J., Madau P., Zemp M., Kuhlen M., Quilis V., 2009, MNRAS, 398, L21
Tinker J., Kravtsov A. V., Klypin A., Abazajian K., Warren M., Yepes G., Gottlöber S., Holz D. E., 2008, ApJ, 688, 709
Vikhlinin A. et al., 2009, ApJ, 692, 1060
Warren M. S., Quinn P. J., Salmon J. K., Zurek W. H., 1992, ApJ, 399, 405
Wen Z. L., Han J. L., Liu F. S., 2010, MNRAS, 407, 533
Zeldovich Y. B., 1970, A&A, 5, 84

This paper has been typeset from a TEX/LATEX file prepared by the author.

Hydrodynamical simulations of coupled and uncoupled quintessence models I: Halo properties and the cosmic web

Edoardo Carlesi,[1] ⋆ Alexander Knebe,[1] Geraint F. Lewis,[2] Scott Wales,[2,3] Gustavo Yepes[1]
[1]*Departamento de Física Teórica, Universidad Autónoma de Madrid, 28049, Cantoblanco, Madrid, Spain*
[2]*Sydney Institute for Astronomy, School of Physics, A28, The University of Sydney, NSW 2006, Australia*
[3]*ARC Centre of Excellence for Climate System Science, School of Earth Sciences, The University of Melbourne, Australia 3010*

Accepted 2014 January 20. Received 2014 January 17; in original form 2013 September 18

ABSTRACT

We present the results of a series of adiabatic hydrodynamical simulations of several quintessence models (both with a free and an interacting scalar field) in comparison to a standard ΛCDM cosmology. For each we use 2×1024^3 particles in a $250h^{-1}\,\mathrm{Mpc}$ periodic box assuming WMAP7 cosmology. In this work we focus on the properties of haloes in the cosmic web at $z = 0$. The web is classified into *voids*, *sheets*, *filaments* and *knots* depending on the eigenvalues of the velocity shear tensor, which are an excellent proxy for the underlying overdensity distribution. We find that the properties of objects classified according to their surrounding environment shows a substantial dependence on the underlying cosmology; for example, while V_{max} shows average deviations of ≈ 5 per cent across the different models when considering the full halo sample, comparing objects classified according to their environment, the size of the deviation can be as large as 20 per cent.

We also find that halo spin parameters are positively correlated to the coupling, whereas halo concentrations show the opposite behaviour. Furthermore, when studying the concentration-mass relation in different environments, we find that in all cosmologies underdense regions have a larger normalization and a shallower slope. While this behaviour is found to characterize all the models, differences in the best-fit relations are enhanced in (coupled) dark energy models, thus providing a clearer prediction for this class of models.

Key words: methods:N-body simulations – galaxies: haloes – cosmology: theory – dark matter

1 INTRODUCTION

Over more than 15 years, since observations of high-redshift Supernovae of type Ia (see Riess et al. 1998; Perlmutter et al. 1999) first indicated that the Universe is undergoing an accelerated expansion, a large number of cosmological probes, including cosmic microwave background (CMB) anisotropies (Larson et al. 2011; Sherwin et al. 2011), weak lensing (Huterer 2010), baryon acoustic oscillations (BAO) (Beutler et al. 2011) and large scale structure (LSS) surveys (Abazajian et al. 2009), have confirmed this startling claim and shown that the Universe is spatially flat. To explain these diverse observation, cosmology requires the presence of a fluid, called dark energy (DE), which permeates the whole Universe and exerts a negative pressure, eventually overcoming the gravitational pull that would otherwise dominate. The standard model of cosmology, referred to as ΛCDM, provides the simplest possible explanation for DE, assuming that DE is played by a constant called Λ which possesses a constant equation of state, such that $p_\Lambda = -\rho_\Lambda$. However, despite its simplicity and observational viability, ΛCDM still lacks of appeal from a purely theoretical point of view, due to *fine tuning* and *coincidence* problems; the first refers to the fact that, if we assume that Λ is the zero-point energy of a fundamental quantum field, to be compatible with the aforementioned cosmological constraints its density requires an unnatural fine-tuning of several tens of orders of magnitude. The second problem arises from the difficulty in explaining in a satisfactory way the fact that matter and dark energy densities *today* have comparable values, although throughout most of the cosmic history their evolutions have followed completely different patterns.

It is thus natural to explore the possibility that dark energy does not take the form of a cosmological constant, Λ, but is instead a dynamical component of the universe, whose energy density evolves with time, eventually dominating in the present epoch. In this sense, a large number of different models, such as Chaplygin gas (Kamenshchik et al. 2001), vector dark energy (Beltrán Jiménez & Maroto 2008; Carlesi et al. 2012), κ-essence (Armendariz-Picon et al. 2000) and quintessence (Wetterich 1995; Caldwell et al. 1998; Copeland et al. 1998; Zlatev et al. 1999) have been proposed to overcome the perceived theoretical shortcomings of the standard cosmology. In particular, quintessence (or scalar field) models are

⋆ E-mail: edoardo.carlesi@uam.es

viable and likely candidates for dynamical dark energy (see Tsujikawa 2013), as they can reproduce current observational data without being plagued by the fine-tuning problem of ΛCDM, since their expansion history - at least for a set of different potentials - is almost insensitive to the particular choice of the field's initial conditions. An interesting subset of quintessence theories is represented by coupled models, where it is assumed that the scalar field has a non-negligible interaction to the dark matter sector (Amendola 2000) and is thus expected to leave a strong imprint on structure formation.

While both classes of quintessence models have been already studied numerically by means of N-body simulations (see for instance Klypin et al. (2003), De Boni et al. (2011) for free and Baldi et al. (2010), Li & Barrow (2011b) for coupled models), in the present work we aim at investigating and highlighting the differences arising among coupled and uncoupled scalar fields with the same potential, and compare our results to a benchmark ΛCDM cosmology. Our aim is to disentangle the effects due to the *fifth force* acting on dark matter particles from those caused to the dynamical nature of dark energy, when considering the deeply non-linear regime of the models. This way we will discern strategies to observationally distinguish between coupled and uncoupled forms of quintessence and thus to provide new tools for model selection.

Using a suitably modified version of the publicly available SPH/N-body code GADGET-2 (Springel 2005) we undertake a series of simulations of different quintessence models with a Ratra-Peebles (Ratra & Peebles 1988) potential and several values of the coupling parameter allowed by current observational constraints. The box size ($250h^{-1}\,\mathrm{Mpc}$), the number of particles (2×1024^3) and the use of adiabatic smoothed particle hydrodynamics allow us to analyse a large amount of different properties with a good resolution and statistics. In this first of a series of papers, we will consider large-scale structures (LSS) and its environment, with the physics of galaxy clusters presented in a follow-up paper (Paper II). In the present work, we analyze in particular the structure of the cosmic web and the correlations between the environment, dark matter haloes and gas across these different cosmological models.

The paper is organized as follows; in Section 2, we briefly recall the general features of the quintessence models considered in this work as well as of the recipes necessary for their simulation using N-body techniques. In Section 3, we discuss the settings of our particular simulations as well as those of the halo finder, together with the classification of the cosmic web. In Section 4 we present LSS properties of the modified frameworks, Section 5 is dedicated to the general features of the cosmic web while in Section 6 we describe the results of the correlation of haloes to their environment. A summary of the results obtained and a discussion on their implications is then presented in section Section 7.

2 PREREQUISITES

Here, we will briefly recall the basic properties of quintessence models and their implementation into a cosmological N-body algorithm. We refer the reader to the works of Wetterich (1995); Amendola (2000); Amendola & Quercellini (2003); Pettorino et al. (2012); Chiba et al. (2013) for discussions on the theoretical and observational properties of (coupled) quintessence models, and to Macciò et al. (2004); Baldi et al. (2010); Li & Barrow (2011a) for a thorough description of the numerical approaches.

Table 1. Values of the coupling and potential used for the uDEand cDE models.

Model	V_0	α	β
uDE	10^{-7}	0.143	–
cDE033	10^{-7}	0.143	0.033
cDE066	10^{-7}	0.143	0.066
cDE099	10^{-7}	0.143	0.099

2.1 The models

In quintessence models the role of dark energy is played by a cosmological scalar field ϕ whose Lagrangian can be generally written as:

$$L = \int d^4x\sqrt{-g}\left(-\frac{1}{2}\partial_\mu\partial^\mu\phi + V(\phi) + m(\phi)\psi_m\bar{\psi}_m\right) \quad (1)$$

where in principle ϕ can interact with the dark matter field ψ_m through its mass term, meaning that, in general, dark matter particles will have a time-varying mass. With a suitable choice of the potential $V(\phi)$, quintessence cosmologies can account for the late time accelerated expansion of the universe both in the interacting and non interacting case. In the present work we have focused on the so called Ratra-Peebles (see Ratra & Peebles 1988) self interaction potential:

$$V(\phi) = V_0\left(\frac{\phi}{M_p}\right)^{-\alpha} \quad (2)$$

where M_p is the Planck mass, while V_0 and α are two constants whose values can be fixed by fitting the model to observational data (see Wang et al. 2012; Chiba et al. 2013).

In Eq. (1), we allowed for the scalar field to interact with matter through the mass term $m(\phi)\psi\bar{\psi}$; a popular choice (Pettorino et al. 2012, see) for the function $m(\phi)$ is:

$$m(\phi) = m_0\exp\left(-\beta(\phi)\frac{\phi}{M_p}\right) \quad (3)$$

which is also the one assumed in this *paper*.

In the following, we have taken into account a constant interaction term $\beta(\phi) = \beta_0$, which from Eq. (3) implies an energy flow from the dark matter to the dark energy sector and thus a diminishing mass for dark matter particles. In Table 1 we list the values for V_0, α and β of Eq. (2) and Eq. (3) as used in the four non-standard cosmologies under investigation - an uncoupled Dark Energy (uDE) model and three coupled Dark Energy (cDE) ones. The latter differ only by the choice of the coupling and have been named accordingly. The particular values used in all the implementations have been selected according to the Cosmic Microwave Background (CMB) constraints discussed in Pettorino et al. (2012), to ensure the cosmologies under investigation to be compatible with the WMAP7 dataset (Komatsu et al. 2011). However, more recent results obtained using Planck data (see Pettorino 2013), provide even tighter constraints on the free parameters of these models, which shall be the object of subsequent investigation.

2.2 Numerical implementation

The first simulations of interacting dark energy models were performed by Macciò et al. (2004), who described the basic steps for implementing interacting quintessence into the ART code. In our

Table 2. Cosmological parameters at $z = 0$ used in the ΛCDM, uDE, cDE033, cDE066 and cDE099 simulations.

Parameter	Value
h	0.7
n	0.951
Ω_{dm}	0.224
Ω_b	0.046
σ_8	0.8

case, we built our implementation on P-GADGET2, a modified version of the publicly available code GADGET2 (Springel et al. 2001; Springel 2005). This version has first been developed to simulate vector dark energy models (see Carlesi et al. 2011, 2012) and was then extended to generic dynamical dark energy as well as coupled dark energy cosmologies. The algorithm used is based on the standard Tree-PM solver with some modifications added to take into account the additional long-range interactions due to the coupled scalar field which effectively act as a rescaling of the gravitational constant. For the implementation of these features non-standard models we followed closely the recipe described in Baldi et al. (2010), to which the reader is referred.

This approach requires that a number of quantities, namely:

- the full evolution of the scalar field ϕ and its derivative $\dot{\phi}$,
- the variation mass of cold dark matter particles $\Delta m(z)$, and
- the background expansion $H(z)$.

have to be computed in advance and then interpolated at run time. We therefore implemented background and first order Newtonian perturbation equations into the publicly available Boltzmann code CMBEASY (Doran 2005) to generate the tables containing the aforementioned quantities. The starting background densities were chosen in order to ensure the same values at $z = 0$ for the cosmological parameters listed in Table 2; linear perturbations have been solved assuming adiabatic initial conditions.

Finally, in the case of non-standard cosmologies it is necessary to properly generate the initial conditions of the N-body simulations taking into account not only the different matter power spectra but also the altered growth factors and logarithmic growth rates, respectively. These are in fact the necessary ingredients to compute the initial particles' displacements and velocities on a uniform Cartesian grid using the first order Zel'dovich approximation (Zel'dovich 1970). We implemented these changes into the publicly available N-Genic[1] MPI code, which is suitable for generating GADGET format initial conditions. Again, the matter power spectra, growth factors $D(t)$ and logarithmic growth rates $f = d\ln D(t)/d\ln a$ have been computed for the four non-standard cosmologies using the modified CMBEASY package.

All the above changes have been carefully tested against theoretical predictions and the previous results existing in the literature to ensure the consistency and reliability of our modifications.

Table 3. N-body settings and cosmological parameters used for the three simulations.

Parameter	Value
L_{box}	$250h^{-1}\,\mathrm{Mpc}$
N_{dm}	1024^3
N_{gas}	1024^3
m_{dm}	$9.04 \times 10^8 h^{-1}\mathrm{M}_\odot$
m_b	$1.85 \times 10^8 h^{-1}\mathrm{M}_\odot$
z_{start}	60

3 THE SIMULATIONS

3.1 Settings

Our set of N-body simulation has been devised in order to allow us to compare and quantitatively study the peculiarities of the different models in the physics of galaxy clusters and the properties of the cosmic web. To do this, we have chosen a box of side length $250h^{-1}\,\mathrm{Mpc}$ (comoving) where we expect to be able to analyze with adequate resolution a statistically significant (> 100) number of galaxy clusters ($M > 10^{14}h^{-1}\mathrm{M}_\odot$) as well as the properties of the different cosmic environments, classified as voids, sheets, filaments and knots. The parameters chosen to set up the simulations, which are common to all the six models under investigation, are listed in Table 3.

In this series of simulations we implemented adiabatic SPH only, thus neglecting the effects of all sources of radiative effects (Monaghan 1992; Springel 2010) This way we are able to establish a clear basis for the differences induced on baryons by the different cosmologies, without the need to take into account the additional layer of complexity introduced of radiative physics, which in itself requires a substantial degree of modeling. The publicly available version of GADGET-2 performs a Lagrangian sampling of the continuous fluid quantities using a set of discrete tracer particles. Gas dynamics equations are then solved using the SPH entropy conservation scheme described in Springel (2005). In our case, continuous fluid quantities are computed using a number of smoothing neighbours $N_{sph} = 40$. Gas pressure and density are related through the relation $P \propto \rho^\gamma$, where $\gamma = \frac{5}{3}$ under the adiabatic assumption.

In addition to the four quintessence models (whose parameters have been given in Table 1) we simulated a ΛCDM cosmology, which we use as a benchmark to pinpoint deviations from the standard paradigm. The initial conditions for all the simulations have been generated using the same random phase realization for the Gaussian fluctuations, which enables us to consistently cross-correlate properties enforcing the same values at present time for Ω_m and σ_8 (cf. Table 2), across different simulations.

3.2 Halo identification

We identified haloes in our simulation using the open source halo finder AHF[2] described in Knollmann & Knebe (2009); this code improves the MHF halo finder (Gill et al. 2004) and has been widely compared to a large number of alternative halo finding methods (Knebe et al. 2011; Onions et al. 2012; Knebe et al. 2013). AHF computes the density field and locates the prospective halo centres

[1] http://www.mpa-garching.mpg.de/gadget/

[2] AHF stands for Amiga Halo Finder, which can be downloaded freely from http://www.popia.ft.uam.es/AHF

at the local overdensities. For each of these density peaks, it determines the gravitationally bound particles, retaining only peaks with at least 20 of them, which are then considered as haloes and further analyzed.

The mass is computed via the equation

$$M_\Delta = \Delta \times \rho_c(z) \times \frac{4\pi}{3} R_\Delta^3. \quad (4)$$

so that $M(R)$ is defined as the total mass contained within a radius R at which the halo matter overdensity reaches Δ times the critical value ρ_c. Since the critical density of the universe is a function of redshift, we must be careful when considering its definition, which reads

$$\rho_c(z) = \frac{3H^2(z)}{8\pi G} \quad (5)$$

as the evolution of the Hubble parameter, $H(z)$ differs at all redshifts in the five models. In the latest version of AHF this problem is solved reading the $H(z)$ for the cDE and uDE models in from a precomputed table, which then allows to compute the $\rho_c(z)$ consistently in each case. For all models we assume $\Delta = 200$.

3.3 Classification of the cosmic web

As we intend to correlate halo properties with the environment, it is necessary to introduce the algorithm used for the classification of the cosmic web into voids, sheets, filaments and knots. Using the term cosmic web (Bond et al. 1996) we refer to the complex visual appearance of the large scale structure of the universe, characterized by thin linear filaments and compact knots crossing regions of very low density (Massey et al. 2007; Kitaura et al. 2009; Jasche et al. 2010).

The exact mathematical formulation for describing the visual impression of the web is highly non-trivial and can be implemented using two different approaches, the geometric one and the dynamic one. The first one relies on the spatial distribution of haloes in simulations (Novikov et al. 2006; Aragón-Calvo et al. 2007) disregarding the dynamical context. The second approach starts with the classification of Hahn et al. (2007), where they identified the type of environment using the eigenvalues of the tidal tensor (i.e. the Hessian of the gravitational potential), rather than studying the matter density distribution.

However, these particular approaches are unable to resolve the web on scales smaller than a few megaparsecs (Forero-Romero et al. 2009). While retaining the original idea of dynamical classification, Hoffman et al. (2012) proposed to replace the tidal tensor with the velocity shear, showing that this approach has a much finer resolution on the smaller scales while reproducing the large scale results of the other approach. Defining the velocity shear tensor as

$$\Sigma_{\alpha\beta} = -\frac{1}{2H_0}\left(\frac{\partial v_\alpha}{\partial r_\beta} - \frac{\partial v_\beta}{\partial r_\alpha}\right) \quad (6)$$

and diagonalizing it, we obtain the eigenvalues λ_1, λ_2 and λ_3. Taking the trace of $\Sigma_{\alpha\beta}$ we obtain

$$Tr(\Sigma_{\alpha\beta}) = \sum_i \lambda_i = -\overrightarrow{\nabla} \cdot \overrightarrow{V} \propto \delta_m \quad (7)$$

from which we see that there is indeed a direct relationship between the eigenvalues of the velocity shear tensor and the matter overdensity. In practice the eigenvalue λ_i is related to the intensity of the inflow (outflow) of matter along the i-th axis in the base where $\Sigma_{\alpha\beta}$ is diagonal.

We therefore proceed to classify the cosmic web ordering the eigenvalues $\lambda_1 > \lambda_2 > \lambda_3$ and defining the different points on the web as (Hoffman et al. 2012; Libeskind et al. 2012, 2013):

- *voids*, if $\lambda_1 < \lambda_{th}$
- *sheets*, if $\lambda_1 > \lambda_{th} > \lambda_2$
- *filaments*, if $\lambda_2 > \lambda_{th} > \lambda_3$
- *knots*, if $\lambda_3 > \lambda_{th}$

where λ_{th} is a free threshold parameter (to be specified below).

The computation of the eigenvalues has been performed on a regular 256^3 grid, corresponding to a cell size of $0.97h^{-1}\,\mathrm{Mpc}$. We use a triangular-shaped cloud (TSC) prescription for the assignment of the particles (Hockney & Eastwood 1988) and then compute the overdensity and the eigenvalues of the velocity shear tensor for every grid cell. Using the AHF catalogues, we assign every halo to the nearest grid point hence providing us with a measure of environment for every object.

At this stage we still have not explicitly classified the cosmic web, as we lack a clear theoretical prescription for the value of λ_{th}. In our case, we have fixed λ_{th} to the highest value which ensures that no halo with $M > 10^{14}h^{-1}\mathrm{M}_\odot$ belongs to a void in any simulation. At a first glance, this kind of constraint might seem redundant, as it would be implied in any standard definition of void as an underdense region. However, we must recall here that our definition of the cosmic web relies solely on the dynamical properties of the matter distribution (being related to the magnitude of its inflow or outflow in a given node) and may in principle overlook its net density content. It is thus necessary to enforce this principle explicitly tuning our free parameter to $\lambda_{th} = 0.1$, which is the value which in this case satisfies the aforementioned condition and has been used in Section 5. For a more elaborate discussion of λ_{th} we refer the reader to Hoffman et al. (2012); we only note that our choice is close to their proposed value.

4 LARGE SCALE CLUSTERING AND GENERAL PROPERTIES

Before presenting the results relative to the properties of the cosmic web and the correlation of halo properties to the environment, we will describe some aspects of large scale structure (LSS) and general halo properties in our simulations. This should give a more traditional overview of the effects of (coupled) dark energy models.

4.1 Halo mass function

The halo mass function (HMF) in coupled dark energy cosmologies has already been studied by Macciò et al. (2004); Nusser et al. (2005); Baldi et al. (2010); Li & Barrow (2011b); Cui et al. (2012) so that we will only briefly comment on the topic. Our results reproduce the earlier findings of Baldi's in the overlapping regions of mass and k-space, thus providing an additional proof of the correct functioning of our modified implementation.

In Fig. 1 we show the cumulative mass (left) and velocity functions (right) as well as the ratio to ΛCDM for the four quintessence models. Singling out the region from 10^{10} to 10^{14} $h^{-1}\mathrm{M}_\odot$, and neglecting the higher mass end, where the statistics is unreliable due to the low number of objects, we can see that the largest difference in number counts amounts to $\approx 7\%$ for the strongest coupled models, gradually decreasing for smaller couplings. In the velocity

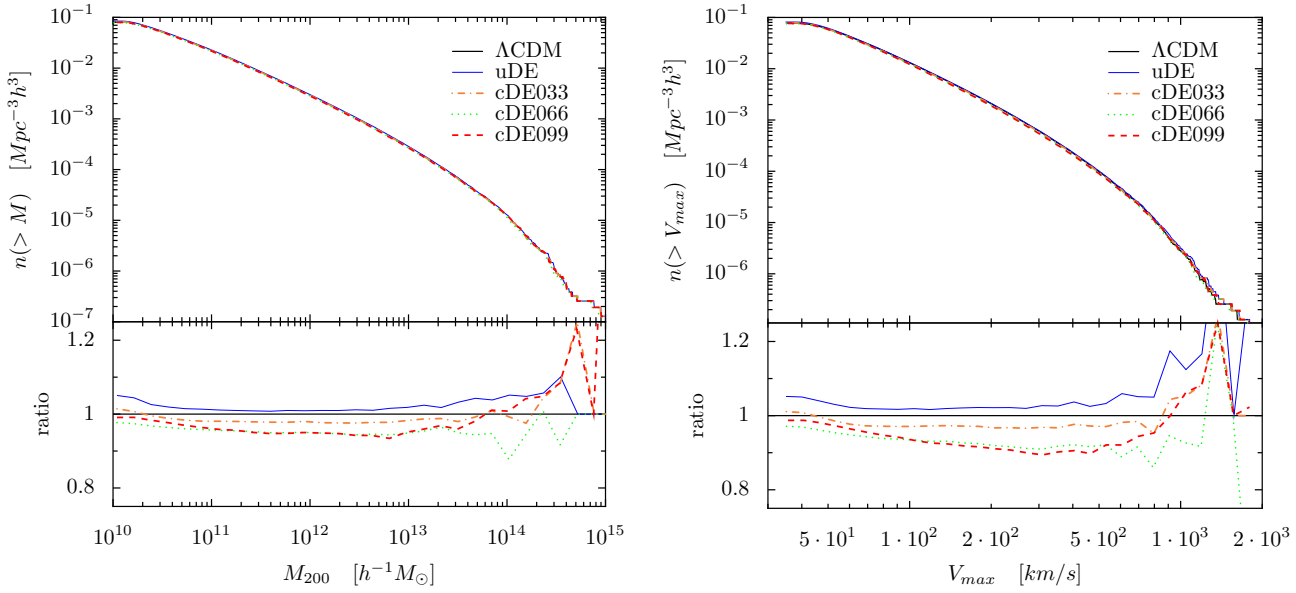

Figure 1. Cumulative halo density number counts as a function of mass (left panel) and V_{max} (right panel). Compared to ΛCDM, a slight suppression of the number of objects produced at redshift $z = 0$ is predicted for cDE models while the opposite is true for uDE. Albeit small, the effect is enhanced in the velocity function, where the strongest coupled model differs up to 10% from ΛCDM (neglecting the higher mass ends, which are affected by a very low statistics).

function, this suppression reaches 10%, thus slightly enhancing the magnitude of the effect.

We can compare our results for the HMF with those of Cui et al. (2012), who modeled the Jenkins et al. (2001) and Tinker et al. (2008) mass functions for a series of similar coupled dark energy models, using Friends-of-Friends (FoF) and Spherical Overdensity (SO) algorithms to build up their halo catalogues. Even though in their simulations they used different σ_8 normalizations, fitting the analytical HMFs to the numerical results they were able to extend the predictions for cDE cosmology to arbitrary σ_8 values. Using the same ΛCDM σ_8 normalization, then, they also found a $5 - 10\%$ suppression of the HMF of cDE, in perfect agreement with our results.

Although not shown here, we have also verified that these $z = 0$ results match the analytical prediction of the Tinker mass function (Tinker et al. 2008), provided the correct input power spectra and normalizations are used. We can safely conclude that the presence of coupled and uncoupled quintessence of the kind described here is expected to produce differences from ΛCDM predictions up to a factor 10% in present day's HMF. Remarkably, this estimate is qualitatively independent of the algorithm used for the halo identification as we have seen comparing our results to the work of Cui et al. (2012).

4.2 Halo properties

To study internal halo properties (such as spin parameter and concentration) we first need to define a statistically sound sample of objects, in order to reduce the impact of spurious effects on the results. This means that we need to constrain our analysis to structures which satisfy some conditions on both *resolution* and *relaxation*.

The first condition means that we have to restrict our analysis to objects with a number of particles above a given threshold, taking into account the existing trade-off between the quality and the size of the halo sample. The second criterion needs to be applied as we want to focus on structures as close as possible to a state of dynamical equilibrium. In fact, many phenomena, such as infalling matter and major mergers, may take place, driving the structure out of equilibrium. In this case, then, the determination of quantities such as density profiles and concentrations becomes unreliable (see for instance Macciò et al. (2007) and Muñoz-Cuartas et al. (2011)).

Following Prada et al. (2012), we will define as relaxed only the haloes that obey to the condition

$$\frac{2K}{|U|} - 1 < 0.5 \tag{8}$$

without introducing other selection parameters; for alternative ways of identifying unrelaxed objects we refer for instance to Macciò et al. (2007); Bett et al. (2007); Neto et al. (2007); Knebe & Power (2008); Prada et al. (2012); Muñoz-Cuartas et al. (2011); Power et al. (2012). For the moment, we neglect the impact of uDE and cDE on the definition of the virial ratio since this effect is of just a few percent (Abdalla et al. 2010; Pace et al. 2010) and is thus subleading in our case, where we are removing objects off by more than 50% from the standard relation.

Now that we have established the rules that will shape our halo sample, we proceed to study some internal properties of dark matter haloes, namely, spin and concentration – as a function of halo mass – enforcing one additional criterion for the halo selection: the number of particles in it. When studying the spin parameter, we will restrict ourselves to haloes with $M_{200} > 3 \times 10^{11} h^{-1}\mathrm{M}_\odot$, i.e. composed of at least ≈ 600 baryon and dark matter particles, following the choices of Bett et al. (2007), Macciò et al. (2007), Muñoz-Cuartas et al. (2011) and Prada et al. (2012). In the case of halo concentrations, we applied a stricter criterion, using $M_{200} > 1 \times 10^{12} h^{-1}\mathrm{M}_\odot$(or ≈ 2000 particles), due to the fact that the computation of halo concentration requires a better resolution

Table 4. Total number of haloes found in each simulation corresponding to our applied mass cuts of $M > 3 \times 10^{11} h^{-1}\mathrm{M}_{\odot}$ and the $M > 10^{12} h^{-1}\mathrm{M}_{\odot}$, respectively.

Mass cut	ΛCDM	uDE	cDE033	cDE066	cDE099
$M > 3 \times 10^{11} h^{-1}\mathrm{M}_{\odot}$	138211	139288	135613	130877	130812
$M > 10^{12} h^{-1}\mathrm{M}_{\odot}$	46196	46179	44943	44363	43749

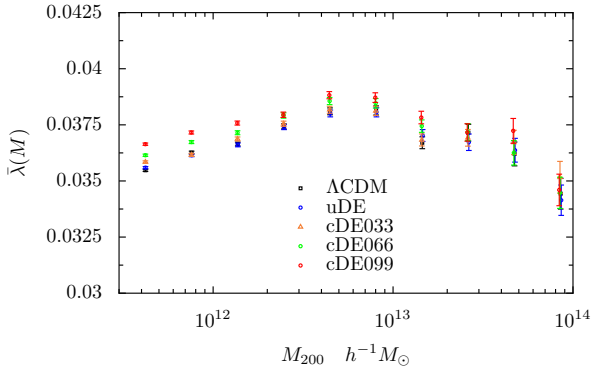

Figure 2. Average value of the spin parameter per mass bin. We can see that the spin parameter has a weak positive correlation to the mass until $\approx 8 \times 10^{12} h^{-1}\mathrm{M}_{\odot}$ and a negative one after that threshold. Further, haloes in coupled dark energy models have an average value which is slightly larger than uncoupled ones.

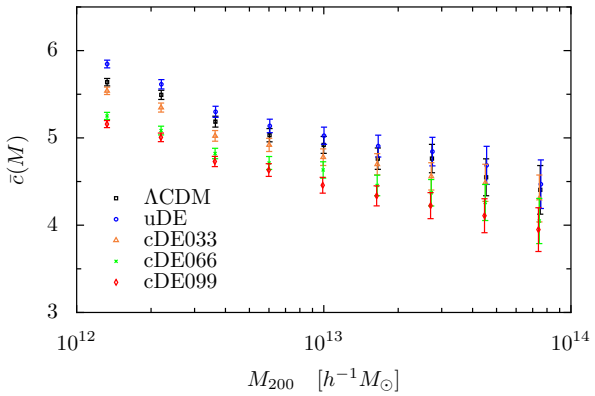

Figure 3. Halo mass concentration relation at $z = 0$, where the median concentration per mass bin is plotted. Compared to ΛCDM, cDE cosmologies show a systematically lower value of c for all mass bins, whereas for uDE it is larger.

of the central regions, as we will discuss in the dedicated subsection.

4.2.1 *Spin parameter*

We can study the rotational properties of haloes introducing the so-called spin parameter λ (e.g. Barnes & Efstathiou 1987; Warren et al. 1992), a dimensionless number that measures the degree of rotational support of the halo. Following Bullock et al. (2001), we define it as

$$\lambda = \frac{L_{200}}{\sqrt{2} M_{200} V_{200} R_{200}} \tag{9}$$

where the quantities the total angular momentum L, the total mass M, the circular velocity V, and the radius R are all taken as defined by Eq. (4), with $\Delta = 200$; in cosmological simulations, the distribution of this parameter is found to be described as lognormal (e.g. Barnes & Efstathiou 1987; Warren et al. 1992; Cole & Lacey 1996; Gardner 2001; Bullock et al. 2001; Macciò et al. 2007, 2008; Muñoz-Cuartas et al. 2011)

$$P(\lambda) = \frac{1}{\lambda \sigma_0^2 \sqrt{2\pi}} \exp\left[-\frac{\ln^2(\lambda/\lambda_0)}{2\sigma_0^2}\right], \tag{10}$$

even though some authors (e.g. Bett et al. 2007) claim that this should be slightly modified.

Due to the non-Gaussian nature of this distribution, instead of the average value we plot in Fig. 2 the median value of the spin parameter λ as a function of halo mass. A weak negative correlation of spin to the halo mass can be observed here for haloes above $8 \times 10^{12} h^{-1}\mathrm{M}_{\odot}$, (as noted for instance by Macciò et al. (2007) and Knebe & Power (2011)) while the relation is positive below that threshold. However, cDE models have on average a higher value (per mass bin) compared to uDE and ΛCDM. Albeit small, this increase in λ is clearly a coupling related effect, the magnitude of which is directly proportional to the value of β. Given the small error bars (due to the large number of objects used in this analysis) we are confident that this is a real effect. Moreover, a similar result has been found by Hellwing et al. (2011), that also claimed to have observed a link between fifth force and larger λs.

A deeper investigation of the physical link between the coupling and increased rotational support is left to an upcoming work (Carlesi et al., in prep.) where the *evolution* of different parameters under different cosmologies will be analyzed. For the moment it is important to note that there appears to be some evidence of a link between the coupling strength of the fifth force and the corresponding degree of rotational support in dark matter haloes.

4.2.2 *Concentration*

Dark matter density profiles can be described by a Navarro-Frenk-White (NFW) profile (Navarro et al. 1996), of the form

$$\rho(r) = \frac{\rho_0}{\frac{r}{r_s}\left(1 + \frac{r}{r_s}\right)^2} \tag{11}$$

where the r_s, the so called scale radius, and the density ρ_0 are in principle two free parameters that depend on the particular halo structure. Using Eq. (11) we can define

$$c = \frac{r_{200}}{r_s} \tag{12}$$

which is the *concentration* of the halo, relating the radius r_{200} to the scale radius r_s. Fitting Eq. (11) to our halo sample we observe that no substantial difference can be seen in the different simulations, that is, the NFW formula describes (on average) equally well dark

Table 5. Best fit values for the mass concentration relation for haloes with $M > 10^{12}h^{-1}\mathrm{M}_{\odot}$.

Model	ΛCDM	uDE	cDE033	cDE066	cDE099
c_0	4.31 ± 0.06	4.48 ± 0.07	4.18 ± 0.06	3.98 ± 0.08	3.86 ± 0.06
γ	-0.088 ± 0.007	-0.093 ± 0.009	-0.083 ± 0.009	-0.084 ± 0.009	-0.079 ± 0.008

matter halo profiles in ΛCDM as in the other (coupled) dark energy models. While this is in contrast with the early findings of Macciò et al. (2004), it is however in good agreement with the subsequent works of Baldi et al. (2010) and Li & Barrow (2011b), who also found the NFW profile to be a valid description of DM haloes in interacting cosmologies. Thus, defining concentrations using Eq. (12) will not pose any problems nor introduce any systematic effect due to the fact that the NFW profile might only be valid for ΛCDM dark matter haloes.

In Fig. 3 we now show the median concentration for objects in a certain mass bin: cDE cosmologies have a smaller concentration than ΛCDM i.e. the larger the β the smaller the c; whereas the opposite is true for the uDE model. This can partly be explained by the fact that concentrations are related to the formation time of the halo, since structures that collapsed earlier tend to have a more compact centre due to the fact that it has more time to accrete matter from the outer parts. Dynamical dark energy cosmologies generically imply larger c values as a consequence of earlier structure formation, as found in works like those by Dolag et al. (2004), Bartelmann et al. (2006) and Grossi & Springel (2009). In fact, since the presence of early dark energy usually suppresses structure growth, in order to reproduce current observations we need to trigger an earlier start of the formation process, which on average yields a higher value for the halo concentrations. However, as explained in Baldi et al. (2010), smaller concentrations in cDE models are not related to the formation time of dark matter halos, but to the fact that one of the effects of coupled quintessence is to effectively act as a positive friction term. This means that dark matter particles have an increased kinetic energy, which moves the system out of virial equilibrium and causes a slight expansion, resulting in a lowering of the concentration.

In the hierarchical picture of structure formation, concentrations are usually inversely correlated to the halo mass as more massive objects form later; N-body simulations (Dolag et al. 2004; Muñoz-Cuartas et al. 2011; Prada et al. 2012) and observations (Comerford & Natarajan 2007; Okabe et al. 2010; Sereno & Zitrin 2012) have in fact shown that the relation between the two quantities can be written as a power law of the form

$$c(M) = c_0 \left(\frac{M_{200}}{10^{14} M_{\odot} h^{-1}} \right)^{\gamma} \tag{13}$$

where γ and c_0 can have explicit parametrizations as functions of redshift and cosmology (see Neto et al. 2007; Muñoz-Cuartas et al. 2011; Prada et al. 2012). When we fit our halo sample to this relation using c_0 and γ as free parameters we obtain the best-fit values as shown in Table 5. Our values are qualitatively in good agreement with the ones found by, for instance, Macciò et al. (2008) and Muñoz-Cuartas et al. (2011) for ΛCDM; but we do find some tension with the findings of Prada et al. (2012). However, since they use a different algorithm for the determination of c (which, according to them, leads to higher concentration values) and a different σ_8 normalizations we cannot directly compare our results to theirs. On the other hand, uDE values are generally in agreement with Dolag et al. (2004), De Boni et al. (2013) although in both cases there are again some discrepancies in the c_0 best-fit result, most probably due to the much different σ_8 used in their simulations. For cDE we cannot directly compare our concentration-mass relation to the one obtained by Baldi et al. (2010) since they do not provide any fit to Eq. (13).

Table 6. Fraction of total dark matter mass for different node type in each simulation.

cell type	ΛCDM	cDE	cDE033	cDE066	cDE099
void	0.103	0.103	0.102	0.103	0.102
sheet	0.343	0.343	0.344	0.344	0.343
filament	0.437	0.438	0.443	0.442	0.443
knot	0.116	0.115	0.109	0.111	0.118

Table 7. Fraction of total gas mass for different node type in each simulation.

cell type	ΛCDM	cDE	cDE033	cDE066	cDE099
void	0.103	0.103	0.103	0.104	0.102
sheet	0.349	0.348	0.348	0.347	0.346
filament	0.449	0.450	0.450	0.449	0.453
knot	0.097	0.097	0.097	0.098	0.098

Table 8. Volume filling fractions of different cell types for all the simulation set.

cell type	ΛCDM	cDE	cDE033	cDE066	cDE099
void	0.337	0.338	0.338	0.337	0.334
sheet	0.460	0.456	0.460	0.460	0.461
filament	0.185	0.184	0.185	0.185	0.186
knot	0.017	0.017	0.017	0.017	0.018

5 PROPERTIES OF THE COSMIC WEB

We now turn to the study of the cosmic web, as defined in Section 3.3, in ΛCDM, uDE, cDE033, cDE066 and cDE099. In Fig. 4 and Fig. 5 we give a visual impression of the web classification (left) and the underlying dark matter density field (right) for a slice of thickness one cell (i.e. $0.97h^{-1}\,\mathrm{Mpc}$) using a logarithmic colouring scheme for the density. From Figs. 4 & 5 it is evident that there is, in general, a very close correspondence between $\delta > 1$ and filamentary and knot-like regions; just like between $\delta < 1$ and void and sheet-like ones, so that the kinetic classification does provide in general a faithful description of the underlying density distribution – as shown in Hoffman et al. (2012). Nonetheless, a minor number of cells do indeed violate this principle. In fact, as also noted by Hoffman et al. (2012), in a very limited number of cases it happens

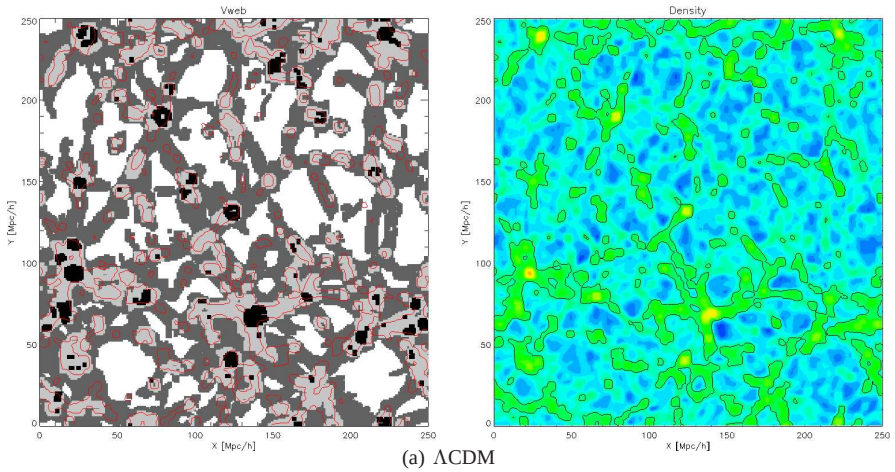

(a) ΛCDM

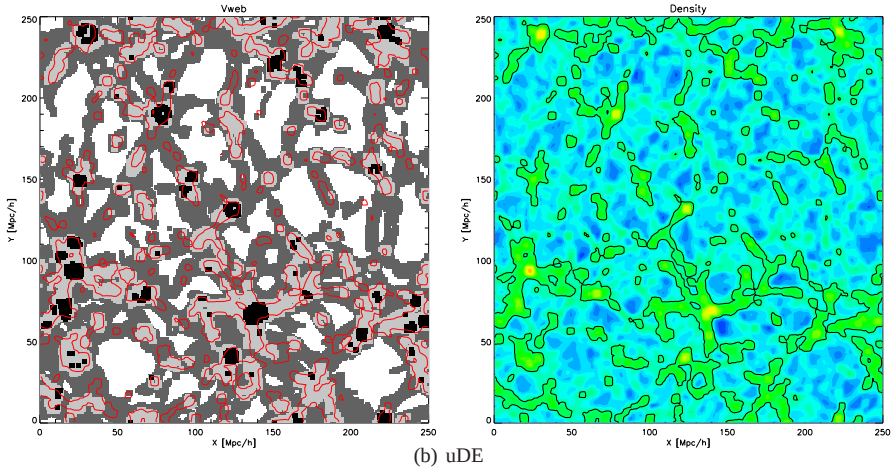

(b) uDE

Figure 4. Cosmic web and matter density field plots for ΛCDM (upper panel) and uDE(lower panel). In the left panels of each pair we plot voids (white points), sheets (dark grey), filaments (light grey) and knots (black), while on top of them we depict red contours enclosing the regions where $\delta > 1$. The right panel of each pair show the colour coded logarithmic matter density, the black solid contours again encompass overdense regions. We notice that there's a very good overlap of overdense regions with filaments and knots, while underdense ones can be identified with voids and sheets.

that, for cells placed in the interior of a of a large dark matter halo, the velocity field will be determined by the motion of its virialized particles and not reflecting the cosmic web, respectively. On top of that, we must not forget that the freedom in the choice of the threshold λ_{th}, and the fixed spacing of the grid account for the fact that on scales smaller than $0.97h^{-1}\,\mathrm{Mpc}$ we cannot properly resolve the complex shape of the web, which would probably require a more flexible grid implementation (Platen et al. 2011). However, all these shortcomings do not seriously invalidate this description, as the number of such cells is generally small (for example, points defined as voids with $\delta > 1$ sum up to less than 1% of the total in all simulation, and independent of the simulation). In fact, the latter is the most important condition that we need to ensure, so that the existence of small biases disappears when considering ratios to ΛCDM, which is at the core of the analysis we are carrying.

In Tabs. 6, 7 & 8 we show the mass and volume filling fractions as a function of cell type and cosmologies. These values are estimated simply summing all masses and volumes contained in cells belonging to the same kind of environment. What is clear by looking at these results is that the general structure of the cosmic web is almost left unchanged across models. In fact, discrepancies among different cosmologies are much less than 1% in this regard, thus making it hard to detect deviations from ΛCDM by simply considering the volume and the mass associated to the various kinds of environment. The same conclusion can be drawn if we look at Fig. 6, which shows the distributions of the three $\lambda_{1,2,3}$ eigenvalues of $\Sigma_{\alpha\beta}$, that appear to be identical and thus provide no leverage to distinguish the models under investigation here.

The gas distribution through the different node types seems also to be largely unaffected by the different cosmology: As we can see from Table 7, the mass fractions of gas are substantially identical throughout all the models, without any significant discrepancy. Comparing to the distribution of dark matter, we do notice a slight increase in the fraction of gas belonging to sheets and filaments paralleled by its reduction on knots, a pattern which is observable in all the models to the same extent.

We remark that our results for uDE agree with Bos et al. (2012), who also found that quintessence cosmologies with Ratra-Peebles potentials do not lead to significant changes in the general properties of the cosmic web. We also emphasize that our findings relative to void regions are largely independent of the choice of λ. Using different threshold values we have been able to test this and

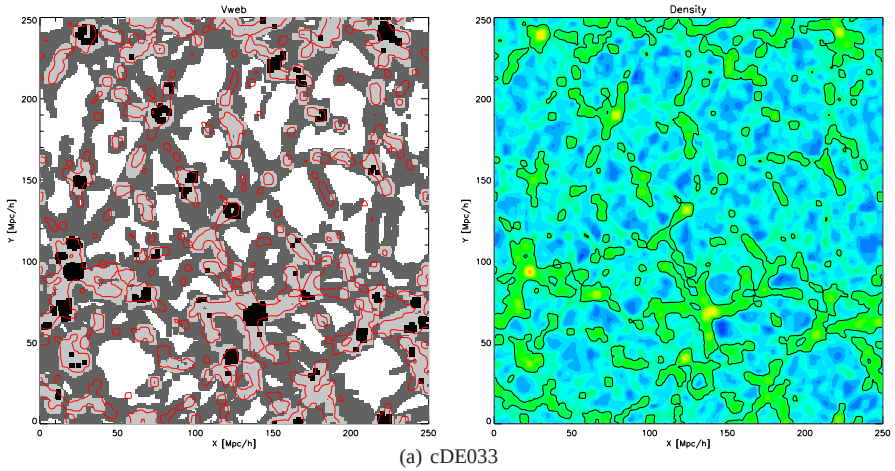

(a) cDE033

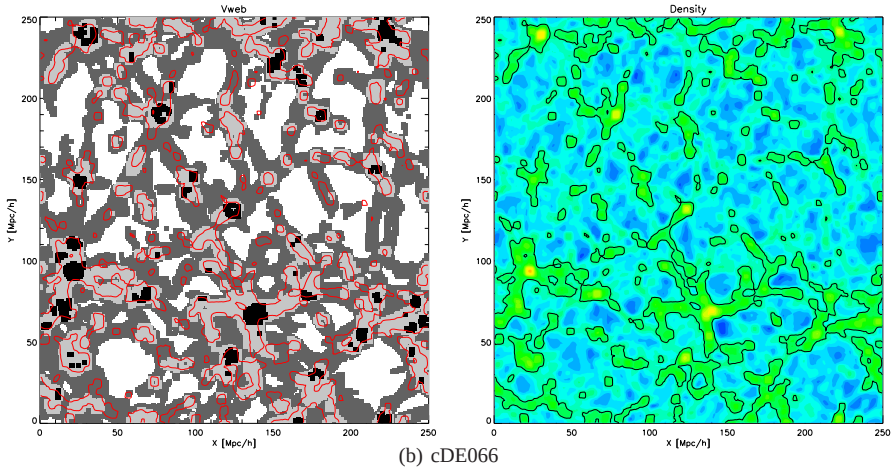

(b) cDE066

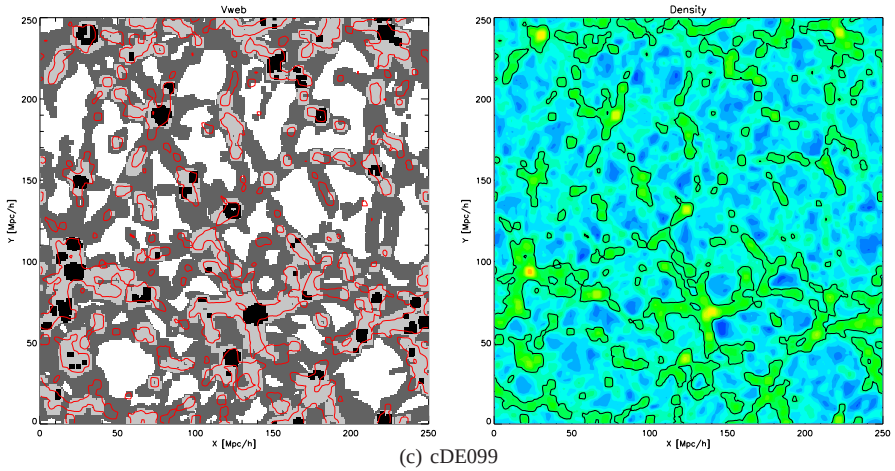

(c) cDE099

Figure 5. Same as Fig. 4 for cDE033 (upper panel), cDE066 (middle panel) and cDE099 (lower panel).

see that void distributions are affected to the same degree in all the different models, confirming this particular result does not depend on our λ_{th}.

6 HALO PROPERTIES IN DIFFERENT ENVIRONMENTS

We now turn to the study of halo properties classified according to their environment; this kind of analysis has already been done for ΛCDM using both geometrical (e.g. Avila-Reese et al. 2005; Macciò et al. 2007) and dynamical (e.g. Hahn et al. 2007; Libe-

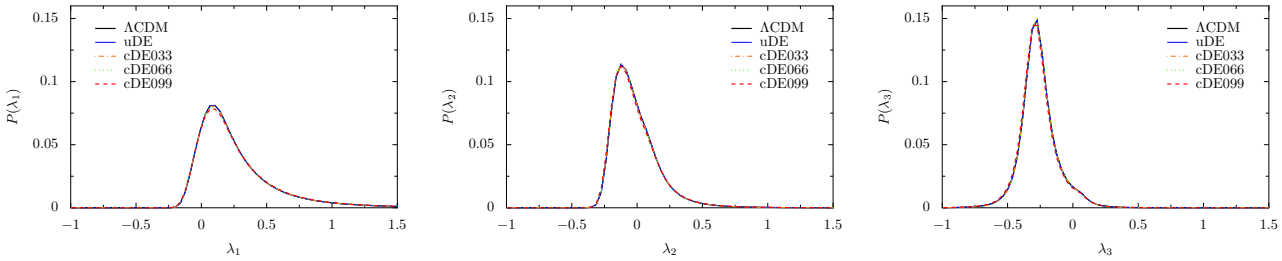

Figure 6. Probability distributions for the eigenvalues of the velocity shear tensor at all nodes. At every node we assume $\lambda_1 > \lambda_2 > \lambda_3$. The distributions are almost identical for all simulations and eigenvalues, except for a progressively lower peak of $P(\lambda_1$ (left panel) for coupled models.

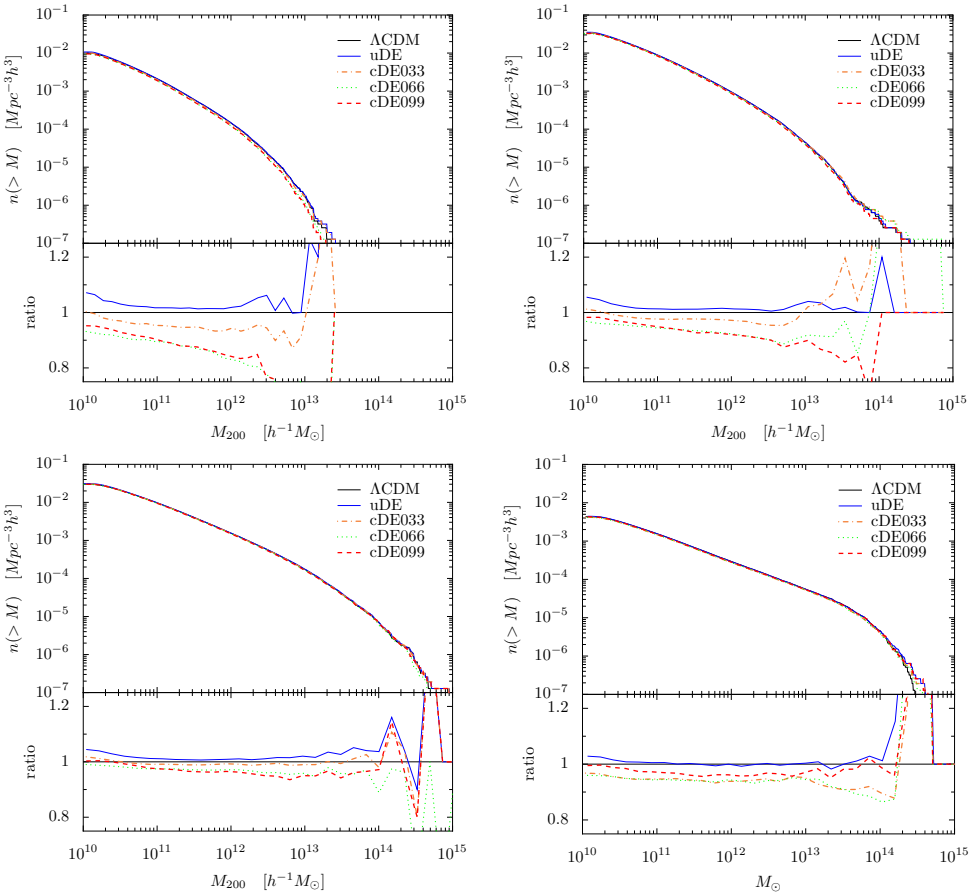

Figure 7. Upper panels: halo mass function in voids (left) and sheets (right). Lower panels: halo mass function in filaments (left) and knots (right).

skind et al. 2012, 2013) web classifications, finding in general a correlation between halo properties such as spin and shape to its surrounding environment.

Using the information from the halo catalogues we proceed to assign each halo to the nearest grid point and build up four different halo samples, one for each cell type. Then we repeat the analysis presented in Section 4 for the halo counts (velocity and mass), spin and concentrations. We will see that this kind of separation of haloes enhances some of the differences already seen in general among different cosmological models and is therefore of great importance when trying to constrain more effectively coupled and uncoupled scalar field cosmologies.

Voids and sheets are readily identified with underdense regions, as has also been confirmed by the analysis presented in the previous Section 5. And the fact that for these cells at most one eigenvalue of the shear tensor has a value above λ_{th} means that in two or more spatial directions there is a net outflow of matter, which is in turn associated with a matter density below the average. For overdense regions (i.e. filaments and knots) there is a net inflow of matter towards the center of the cell from at least two directions. Following this we partition the subsequent study into underdense regions on the one hand (using voids and sheets) and overdense regions (i.e. filaments and knots) on the other.

Underdense regions in ΛCDM are usually associated with lower spins and slightly larger halo concentrations (Macciò et al.

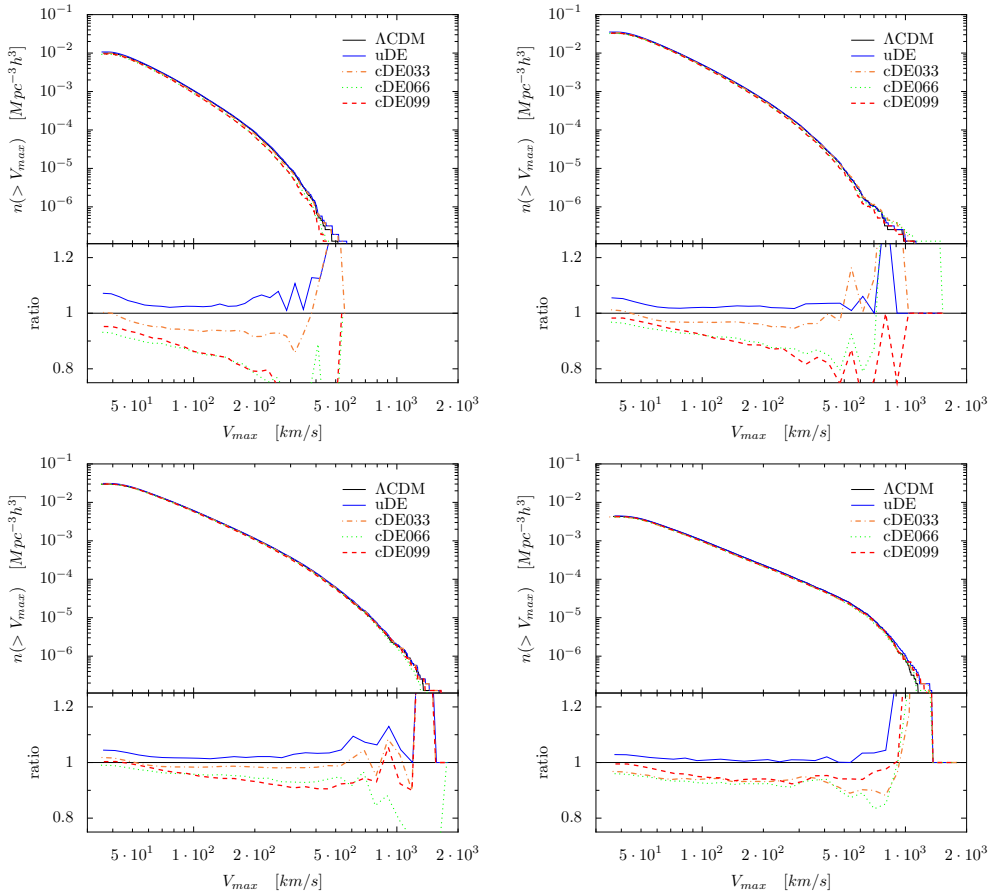

Figure 8. Upper panels: halo velocity function in voids (left) and sheets (right). Lower panels: halo velocity function in filaments (left) and knots (right).

Table 9. Fraction of haloes above $10^{10}h^{-1}\mathrm{M}_{\odot}$ per environment type, in each cosmological model.

Environment	ΛCDM	uDE	cDE033	cDE066	cDE099
void	0.128	0.131	0.127	0.123	0.124
sheet	0.431	0.432	0.431	0.429	0.428
filament	0.384	0.382	0.387	0.392	0.391
knot	0.055	0.054	0.053	0.055	0.056

2007), raising the question whether this still holds for (coupled) dark energy cosmologies.

6.1 Halo number counts

Even though, by definition, underdense regions are less populated, non-negligible fractions of the total halo count can be still found in voids and sheets, as shown in Table 9, ensuring that the samples used are reasonably large, and allow us to draw credible conclusions.

6.1.1 Underdense regions: voids and sheets

We notice that in underdense regions (i.e. voids and sheets, shown in the upper two plots) the trend persists that the number of objects is smaller for cDE models than for ΛCDM, something also observed for the general halo sample. However, it is important to remark that singling out and counting the objects belonging to the underdense parts only, we end up observing larger differences among the models. This effect also appears to be much stronger in cDE than in uDE. In fact, whereas the differences in number counts of objects does not exceed 7%, when restricting halo counts to void regions only, we can see that cDE models' underprediction is much larger and peaks at 20% (ignoring the higher mass ends, where only a small number of objects is found). It is also clear from Fig. 8 that while the sign of the effect is very similar in both voids and sheets, its strength is slightly reduced in the latter type of web, suggesting that there exists at least a mild dependence of this phenomenon on the specific kind of environment. Although we are not showing it here, we have also carefully checked that this result is substantially independent from the kind of λ_{th} chosen. In fact, repeating our

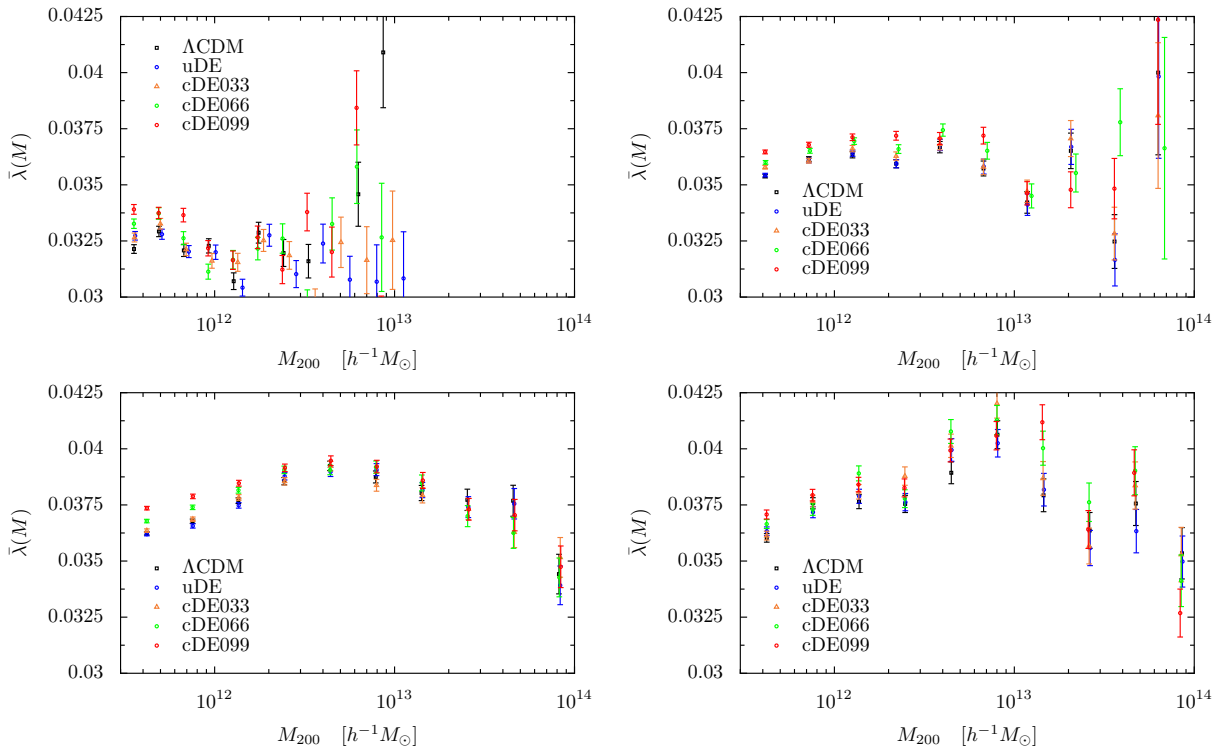

Figure 9. Median of the spin parameter for haloes located in voids (upper left panel), sheets (upper right panel) filaments (lower left panel) and knots (lower right panel).

computation using higher threshold values, we see that the magnitude of the effect does not change substantially. The physical mechanism behind this effect is understood and provides a consistent framework for interpreting our results. In fact, as first explained by Keselman et al. (2010) and subsequently confirmed by Li & Barrow (2011b), fifth forces enhance the gravitational pull towards the overdense regions, quickly evacuating matter from underdense regions. This causes these environments to have less structures, so that in the end the number of haloes left in voids will be comparatively smaller than in the non-interacting cases, as found in our simulations.

However, we need to make an additional remark on this result before proceeding to the next section. In fact, we note that our choice of the σ_8 normalization, which is taken to be the same at $z = 0$, plays an important role in the result just described. It is in fact known (see e.g. Baldi & Pettorino 2011) that using a different normalization prescription (for instance, at the redshift of the CMB for the matter density fluctuations), coupled models end up predicting (in total) more objects than ΛCDM. Hence, at this stage we cannot completely disentangle the influence of our choice of the normalization of the initial conditions from the genuine influence of the additional interaction.

6.1.2 *Overdense regions: filaments and knots*

Like in the case of underdensities, we notice for overdense regions (shown in the lower two plots) that the trend of suppression which characterizes the general halo counting still holds, even though now the strength of this effect is slightly smaller across all cosmologies. This is not unexpected, since the effect seen in the HMF discussed in Section 4 has to be obtained from a combination of both underdense and overdense structures, and should therefore result in an intermediate value for cDE halo underproduction. Again, we have checked that the chosen threshold for the eigenvalues of the velocity shear tensor does not substantially affect this conclusion.

We can therefore state that there is a progression towards smoothing out the differences among different cosmologies while moving to increasingly higher density regions. *This is a very important result that indicates that underdense regions should be the target of choice when searching for the effects of additional long range gravitational-like forces*.

This result is in line with what has been already found for other fifth-force cosmologies (see Martino & Sheth 2009; Keselman et al. 2010; Li et al. 2012; Winther et al. 2012), where the environmental dependence and in particular the properties of voids were stressed as powerful tests for additional interactions and modifications of standard Newtonian gravity. It is in fact well known that void properties are extremely sensitive to cosmology (Lee & Park 2009; Lavaux & Wandelt 2010; Bos et al. 2012; Sutter et al. 2012) and hence provide a powerful probe of alternative models. In particular, when the extra coupling in the dark sector is weak (as in the cases analyzed here) the complex evolution and phenomena that characterize the overdense regions may conceal its imprints, while void regions, whose dynamics is comparatively simpler, are expected to be more directly linked to the underlying cosmology.

6.2 Spin and concentration

We now turn to the non-dimensional spin parameter, λ, and dark matter halo concentrations, investigating how they will change

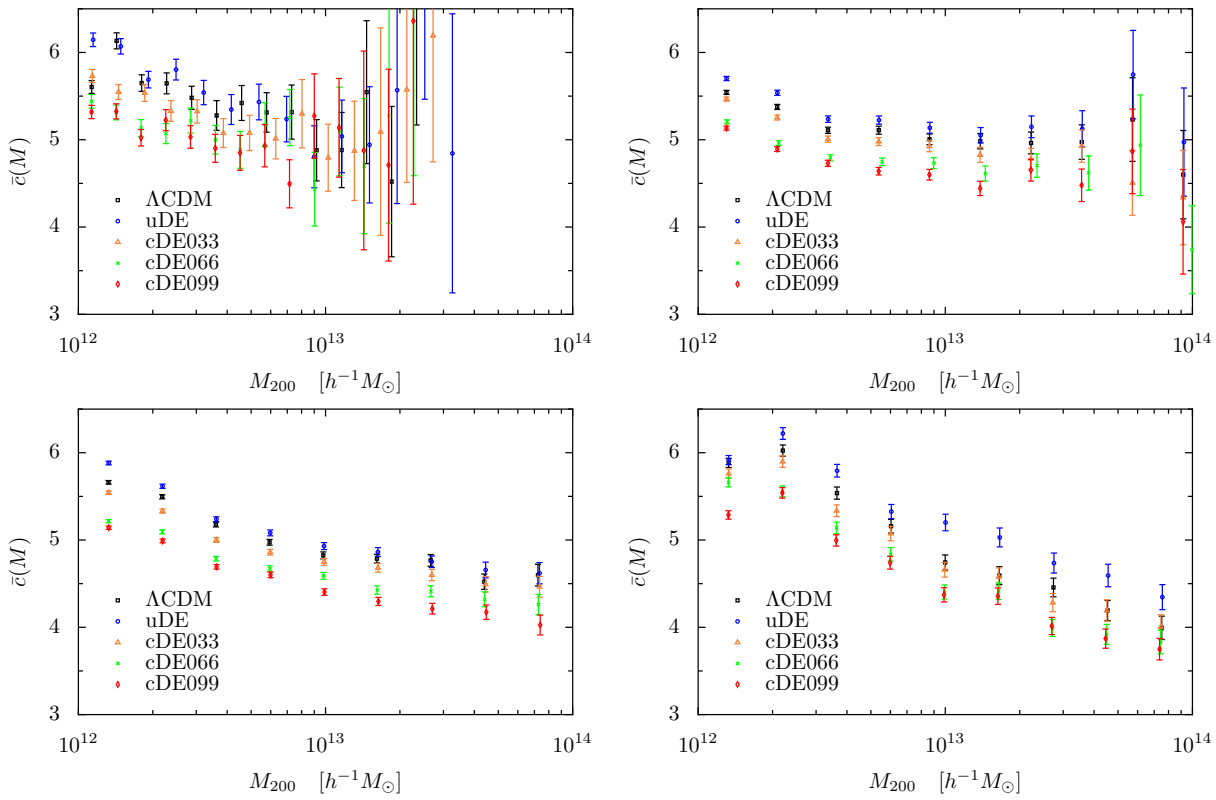

Figure 10. Average concentration for haloes located in voids (upper left panel), sheets (upper right panel), filaments (lower left panel) and knots (lower right panel).

Table 10. Best fit values for the concentration-mass Eq. (13) relation for haloes belonging to voids (v) sheets (s) filaments(f) and knots (k).

Parameter	ΛCDM	cDE	cDE033	cDE066	cDE099
c_0(v)	5.1 ± 0.5	5.36 ± 0.5	4.5 ± 0.2	4.5 ± 0.3	4.3 ± 0.3
γ(v)	-0.03 ± 0.01	-0.03 ± 0.01	-0.04 ± 0.01	-0.04 ± 0.01	-0.03 ± 0.01
c_0(s)	4.8 ± 0.1	5.1 ± 0.2	4.5 ± 0.1	4.3 ± 0.2	4.2 ± 0.1
γ(s)	-0.034 ± 0.007	-0.037 ± 0.009	-0.04 ± 0.01	-0.04 ± 0.01	-0.036 ± 0.008
c_0(f)	4.41 ± 0.05	4.42 ± 0.03	4.26 ± 0.05	4.15 ± 0.04	3.98 ± 0.05
γ(f)	-0.052 ± 0.01	-0.059 ± 0.006	-0.07 ± 0.01	-0.064 ± 0.008	-0.058 ± 0.005
c_0(k)	4.06 ± 0.07	4.38 ± 0.08	4.02 ± 0.06	3.74 ± 0.06	3.67 ± 0.07
γ(k)	-0.087 ± 0.009	-0.093 ± 0.008	-0.085 ± 0.005	-0.093 ± 0.009	-0.092 ± 0.007

across different environments and cosmologies. In the latter case, we will also pay particular attention to the environment-related changes to the $c - M$ relation of Eq. (13). In both cases we refer to the definitions introduced in Section 4.

6.2.1 *Underdense regions: voids and sheets*

Looking at the median spin parameters shown in the upper panel of Fig. 9 we can again draw the conclusion that, just like in the general case, cDE cosmologies lead to larger spins and that this increase is proportional to the coupling parameter β. On the other hand, the value of $\bar{\lambda}$ for haloes in uDE cosmologies is, on average, indistinguishable from ΛCDM. We can therefore confirm the observation that underdense region contain haloes with lower spins, just as found by Macciò et al. (2007). However, the reduction in the median value is of the same order in all models, so that combining the information of the environment does not put tight constraints on the parameters of the model.

Concentrations, too, show a remarkable behaviour for haloes belonging to underdense regions. In Table 10 we show the results of fitting the median concentration per mass bin to a power law, i.e. Eq. (13). The first thing we observe is that the correlation between c and M (as measured by the power-law index γ) is weaker than what we observed in the general case. This, combined with the fact that in the lower mass bins median concentration do not change with respect to the general case, in turn leads to observed larger values for c_0, although the errors are also large due to the small number statistics. However, some care must be taken when considering this

relation for void haloes since the fit is based upon a small mass range only and also gives more weight to lower mass objects (Prada et al. 2012; De Boni et al. 2013).

6.2.2 *Overdense regions: filaments and knots*

In the bottom panels of Fig. 9 and Fig. 10 we plot the spin and concentration-mass relation; the best-fit values to Eq. (13) are again provided in Table 10.

In the case of spins, we find that dark matter haloes in coupled cosmologies tend to be characterized by larger values of λ. However, haloes located in filamentary structures show, at least in the lower mass bins, sharper differences between cDE models and ΛCDM than what is revealed by knots. This is also due to the smaller number of low mass haloes living in knots, which visibly affects the statistics of the parameter.

Concentrations instead show two slightly different patterns in filaments and in knots. In the former environment, all cosmologies seem to be characterized by a flatter slope, which averages around -0.06 and seems not to be connected to the underlying model. In the latter environment, a steeper correlation is found, with $\gamma \approx -0.09$ – much closer to the general case discussed in Section 4. Not only the slope but also the normalization c_0 of Eq. (13) changes when considering filamentary or knot-like environments: in the former case we find that this parameter is substantially larger than in the latter.

Our results therefore indicate that the concentration-mass relation is not only affected by the cosmological model but also by the environment the haloes under consideration live in: γ gets flatter while c_0 increases for decreasing densities. However, at odds with what we found for halo number counts, we find here that environment does not play a role in strengthening the magnitude of model-dependent properties of haloes. While the effect of dark energy can still be clearly seen in the higher spins and lower concentrations of dark matter haloes, these cDE-induced characteristics are not enhanced by the environment. In fact, whereas the halo content of the different regions depends on the model and reinforces the trends observed in Section 4.2, the properties of the haloes themselves, while still being correlated to the underlying cosmology, seem to be shifted by the same amount as ΛCDM. This suggests that environmental effects, in these cases, influence to the same extent both quintessential and standard models, and do not provide a stronger model-specific kind of prediction.

7 CONCLUSIONS

In the present work – which forms part of a series of studies of (coupled) dark energy models – we have discussed the properties of large-scale structures and the cosmic web as they emerge in a series of different quintessence models, systematically comparing the results of a coupled scalar field to those obtained for a free field and the standard ΛCDM cosmology.

We performed the following three-fold analysis:

- we studied halo mass function and general halo properties (mass, spin and concentrations),
- we investigated the general properties of the cosmic web, using a kinetic classification algorithm,
- we correlated halo properties to the environment.

First, we have studied several aspects of cDE and uDE cosmologies looking at the full halo sample. At this stage, our results proved to be in line with those of Baldi et al. (2010); Li & Barrow (2011b); Cui et al. (2012), finding that the analytical formulae for the halo mass functions and dark matter profiles are valid also in this class of models.

Examining concentrations we found that, while uDE cosmology is characterized by haloes with higher values for c, for cDE models the opposite is in general the case – in accordance with the results of Baldi et al. (2010) and De Boni et al. (2013). Interestingly, in the case of spin parameters we observe a weak dependence on the coupling, since we can see that their value is mildly enhanced by larger values of β, as was also noted by Hellwing et al. (2011) in the context of other fifth force cosmological models.

The cosmic web investigated as part of this study is characterized by the eigenvalues of the velocity shear tensor, a novel method recently proposed by Hoffman et al. (2012) and successfully applied to various simulations by Libeskind et al. (2012). Computing the fraction of total mass and volume belonging to each type of environment in our cosmologies, we find that the structure of the cosmic web itself does not reveal any particular difference among the models. The same conclusion can be drawn when investigating the global distribution of the shear tensor eigenvalues.

This notwithstanding, the classification of the cosmic web can be extremely useful when married with the halo catalogue. Combining the two, in fact, we were able to show that many of the differences observed in some halo properties when studying a global sample of relaxed structures above a threshold mass are in fact due to objects belonging to a certain type of environment. This happens in particular in voids and sheets, where the differences among cDE and ΛCDM are up to three times as large as they are in the general case. We have been able to verify how the magnitude of this effect is closely dependent on the coupling: while cDE cosmologies' underproduction of haloes in these regions is largely amplified, the overproduction that characterizes the uDE model investigated here is only weakly enhanced. This means that;

- one should focus on voids and sheets (underdense regions) when looking for signatures of (coupled) dark energy, and
- the magnitude of the deviations from ΛCDM allows us to place constraints on cDE cosmologies, or even detect them.

We have also seen how the standard concentration-mass relation is substantially affected when fitted for halo samples classified according to the environment they are located in. While the standard functional form of Eq. (13) still holds in underdense regions for all the models, it does so with a much steeper slope (the change is from an average of -0.9 to -0.4) and a substantial increase in the average concentration. In addition to this, we note again an amplification of the difference between the c_0 values in cDE and ΛCDM obtained when fitting Eq. (13) in voids and sheets (up to 15%) with respect to the global one (≈ 7 per cent).

The fact that these results are mostly visible when restricting the halo sample to underdense environments tells us the importance of the relative weights to be attached when performing global analyses. Indeed, when referring to halo properties in general, we do in fact hide a large number of peculiar features which can be seen only in a narrower subset. In the particular case of cDE we have seen how structures in voids play a major role, in the same direction of Li & Barrow (2011b), who also highlighted the importance of underdense regions in the context of similar cosmological models.

As a concluding remark, we would like to emphasize that a great amount of effects observed here still deserve a more in-depth study. In particular, the analysis of the temporal evolution of halo

parameters, will shed more light on the mechanisms that result in the previously discussed differences at $z = 0$ and increase the observational features that can be used to constrain quintessence models. We shall turn to these in future contributions in this series.

ACKNOWLEDGEMENTS

EC is supported by the *Spanish Ministerio de Economía y Competitividad* (MINECO) under grant no. AYA2012-31101, and MultiDark Consolider project under grant CSD2009-00064. He further thanks Georg Robbers for providing an updated, non-public version of `CMBEASY`.

This work was undertaken as part of the Survey Simulation Pipeline (SSimPL: ssimpluniverse.tk) and GFL acknowledges support from ARC/DP 130100117

AK is supported by the *Spanish Ministerio de Ciencia e Innovación* (MICINN) in Spain through the Ramón y Cajal programme as well as the grants AYA 2009-13875-C03-02, CSD2009-00064, CAM S2009/ESP-1496 (from the ASTROMADRID network) and the *Ministerio de Economía y Competitividad* (MINECO) through grant AYA2012-31101. He further thanks Emily for reflect on rye.

GY acknowledges support from MINECO under research grants AYA2012-31101, FPA2012-34694, Consolider Ingenio SyeC CSD2007-0050 and from Comunidad de Madrid under ASTROMADRID project (S2009/ESP-1496).

The authors thankfully acknowledge the computer resources, technical expertise and assistance provided by the Red Española de Supercomputación.

We further acknowledge partial support from the European Union FP7 ITN INVISIBLES (Marie Curie Actions, PITN-GA-2011-289442).

All the simulations used in this work were performed in the Marenostrum supercomputer at Barcelona Supercomputing Center (BSC).

REFERENCES

Abazajian K. N., et al., 2009, ApJS, 182, 543
Abdalla E., Abramo L. R., de Souza J. C. C., 2010, Phys. Rev. D, 82, 023508
Amendola L., 2000, Phys. Rev. D, 62, 043511
Amendola L., Quercellini C., 2003, Phys. Rev. D, 68, 023514
Aragón-Calvo M. A., van de Weygaert R., Jones B. J. T., van der Hulst J. M., 2007, ApJ, 655, L5
Armendariz-Picon C., Mukhanov V., Steinhardt P. J., 2000, Phys. Rev. Lett., 85, 4438
Avila-Reese V., Colín P., Gottlöber S., Firmani C., Maulbetsch C., 2005, ApJ, 634, 51
Baldi M., Pettorino V., 2011, MNRAS, 412, L1
Baldi M., Pettorino V., Robbers G., Springel V., 2010, MNRAS, 403, 1684
Barnes J., Efstathiou G., 1987, ApJ, 319, 575
Bartelmann M., Doran M., Wetterich C., 2006, A&A, 454, 27
Beltrán Jiménez J., Maroto A. L., 2008, Phys. Rev. D, 78, 063005
Bett P., Eke V., Frenk C. S., Jenkins A., Helly J., Navarro J., 2007, MNRAS, 376, 215
Beutler F., Blake C., Colless M., Jones D. H., Staveley-Smith L., Campbell L., Parker Q., Saunders W., Watson F., 2011, MNRAS, 416, 3017
Bond J. R., Kofman L., Pogosyan D., 1996, Nature, 380, 603
Bos E. G. P., van de Weygaert R., Dolag K., Pettorino V., 2012, MNRAS, 426, 440
Bullock J. S., Dekel A., Kolatt T. S., Kravtsov A. V., Klypin A. A., Porciani C., Primack J. R., 2001, ApJ, 555, 240
Caldwell R. R., Dave R., Steinhardt P. J., 1998, Physical Review Letters, 80, 1582
Carlesi E., Knebe A., Yepes G., Gottlöber S., Jiménez J. B., Maroto A. L., 2011, MNRAS, 418, 2715
Carlesi E., Knebe A., Yepes G., Gottlöber S., Jiménez J. B., Maroto A. L., 2012, MNRAS, 424, 699
Chiba T., De Felice A., Tsujikawa S., 2013, Phys. Rev. D, 87, 083505
Cole S., Lacey C., 1996, MNRAS, 281, 716
Comerford J. M., Natarajan P., 2007, MNRAS, 379, 190
Copeland E. J., Liddle A. R., Wands D., 1998, Phys. Rev. D, 57, 4686
Cui W., Baldi M., Borgani S., 2012, MNRAS, 424, 993
De Boni C., Dolag K., Ettori S., Moscardini L., Pettorino V., Baccigalupi C., 2011, MNRAS, 415, 2758
De Boni C., Ettori S., Dolag K., Moscardini L., 2013, MNRAS, 428, 2921
Dolag K., Bartelmann M., Moscardini L., Perrotta F., Baccigalupi C., Meneghetti M., Tormen G., 2004, Modern Physics Letters A, 19, 1079
Doran M., 2005, JCAP, 10, 11
Forero-Romero J. E., Hoffman Y., Gottlöber S., Klypin A., Yepes G., 2009, MNRAS, 396, 1815
Gardner J. P., 2001, ApJ, 557, 616
Gill S. P. D., Knebe A., Gibson B. K., 2004, MNRAS, 351, 399
Grossi M., Springel V., 2009, MNRAS, 394, 1559
Hahn O., Carollo C. M., Porciani C., Dekel A., 2007, MNRAS, 381, 41
Hellwing W. A., Cautun M., Knebe A., Knollmann S., Juszkiewicz R., 2011, ArXiv e-prints
Hockney R. W., Eastwood J. W., 1988, Computer simulation using particles
Hoffman Y., Metuki O., Yepes G., Gottlöber S., Forero-Romero J. E., Libeskind N. I., Knebe A., 2012, MNRAS, 425, 2049
Huterer D., 2010, General Relativity and Gravitation, 42, 2177
Jasche J., Kitaura F. S., Li C., Enßlin T. A., 2010, MNRAS, 409, 355
Jenkins A., Frenk C. S., White S. D. M., Colberg J. M., Cole S., Evrard A. E., Couchman H. M. P., Yoshida N., 2001, MNRAS, 321, 372
Kamenshchik A., Moschella U., Pasquier V., 2001, Physics Letters B, 511, 265
Keselman J. A., Nusser A., Peebles P. J. E., 2010, Phys. Rev. D, 81, 063521
Kitaura F. S., Jasche J., Li C., Enßlin T. A., Metcalf R. B., Wandelt B. D., Lemson G., White S. D. M., 2009, MNRAS, 400, 183
Klypin A., Macciò A. V., Mainini R., Bonometto S. A., 2003, ApJ, 599, 31
Knebe A., et al., 2013, ArXiv e-prints
Knebe A., Knollmann S. R., Muldrew S. I., Pearce F. R., et al., 2011, MNRAS, 415, 2293
Knebe A., Power C., 2008, ArXiv:0801.4453
Knebe A., Power C., 2011, in Wozniak H., Hensler G., eds, EAS Publications Series Vol. 44 of EAS Publications Series, A correlation between spin parameter and dark matter halo mass. pp 53–56
Knollmann S. R., Knebe A., 2009, ApJS, 182, 608
Komatsu E., et al., 2011, ApJS, 192, 18

Larson D., et al., 2011, ApJS, 192, 16
Lavaux G., Wandelt B. D., 2010, Mon.Not.Roy.Astron.Soc., 403, 1392
Lee J., Park D., 2009, Astrophys.J., 696, L10
Li B., Barrow J. D., 2011a, Phys. Rev. D, 83, 024007
Li B., Barrow J. D., 2011b, MNRAS, 413, 262
Li B., Zhao G.-B., Koyama K., 2012, MNRAS, 421, 3481
Libeskind N. I., Hoffman Y., Knebe A., Steinmetz M., Gottlöber S., Metuki O., Yepes G., 2012, MNRAS, 421, L137
Libeskind N. I., Hoffman Y., Steinmetz M., Gottlöber S., Knebe A., Hess S., 2013, ApJ, 766, L15
Macciò A. V., Dutton A. A., van den Bosch F. C., 2008, MNRAS, 391, 1940
Macciò A. V., Dutton A. A., van den Bosch F. C., Moore B., Potter D., Stadel J., 2007, MNRAS, 378, 55
Macciò A. V., Quercellini C., Mainini R., Amendola L., Bonometto S. A., 2004, Phys. Rev. D, 69, 123516
Martino M. C., Sheth R. K., 2009
Massey R., et al., 2007, Nature, 445, 286
Monaghan J. J., 1992, ARA&A, 30, 543
Muñoz-Cuartas J. C., Macciò A. V., Gottlöber S., Dutton A. A., 2011, MNRAS, 411, 584
Navarro J. F., Frenk C. S., White S. D. M., 1996, ApJ, 462, 563
Neto A. F., et al., 2007, MNRAS, 381, 1450
Novikov D., Colombi S., Doré O., 2006, MNRAS, 366, 1201
Nusser A., Gubser S. S., Peebles P., 2005, Phys.Rev., D71, 083505
Okabe N., Takada M., Umetsu K., Futamase T., Smith G. P., 2010, PASJ, 62, 811
Onions J., Knebe A., Pearce F. R., Muldrew S. I., Lux H., Knollmann S. R., Ascasibar Y., Behroozi P., Elahi P., Han J., Maciejewski M., Merchán M. E., Neyrinck M., Ruiz A. N., Sgró M. A., Springel V., Tweed D., 2012, MNRAS, 423, 1200
Pace F., Waizmann J., Bartelmann M., 2010, MNRAS, 406, 1865
Perlmutter S., et al., 1999, ApJ, 517, 565
Pettorino V., 2013, Phys. Rev. D, 88, 063519
Pettorino V., Amendola L., Baccigalupi C., Quercellini C., 2012, Phys. Rev. D, 86, 103507
Platen E., van de Weygaert R., Jones B. J. T., Vegter G., Calvo M. A. A., 2011, MNRAS, 416, 2494
Power C., Knebe A., Knollmann S. R., 2012, MNRAS, 419, 1576
Prada F., Klypin A. A., Cuesta A. J., Betancort-Rijo J. E., Primack J., 2012, MNRAS, 423, 3018
Ratra B., Peebles P. J. E., 1988, Phys. Rev. D, 37, 3406
Riess A. G., et al., 1998, AJ, 116, 1009
Sereno M., Zitrin A., 2012, MNRAS, 419, 3280
Sherwin B. D., et al., 2011, Physical Review Letters, 107, 021302
Springel V., 2005, MNRAS, 364, 1105
Springel V., 2010, ARA&A, 48, 391
Springel V., Yoshida N., White S. D. M., 2001, NewA, 6, 79
Sutter P. M., Lavaux G., Wandelt B. D., Weinberg D. H., 2012, ApJ, 761, 187
Tinker J., Kravtsov A. V., Klypin A., Abazajian K., Warren M., Yepes G., Gottlöber S., Holz D. E., 2008, ApJ, 688, 709
Tsujikawa S., 2013, ArXiv e-prints
Wang P.-Y., Chen C.-W., Chen P., 2012, JCAP, 2, 16
Warren M. S., Quinn P. J., Salmon J. K., Zurek W. H., 1992, ApJ, 399, 405
Wetterich C., 1995, A&A, 301, 321
Winther H. A., Mota D. F., Li B., 2012, ApJ, 756, 166
Zel'dovich Y. B., 1970, A&A, 5, 84
Zlatev I., Wang L., Steinhardt P. J., 1999, Physical Review Letters, 82, 896

This paper has been typeset from a TEX/ LATEX file prepared by the author.

Hydrodynamical simulations of coupled and uncoupled quintessence models II: Galaxy clusters

Edoardo Carlesi,[1] ⋆ Alexander Knebe,[1] Geraint F. Lewis,[2] Gustavo Yepes[1]
[1]*Departamento de Física Teórica, Universidad Autónoma de Madrid, 28049, Cantoblanco, Madrid, Spain*
[2]*Sydney Institute for Astronomy, School of Physics, The University of Sydney, NSW 2006, Australia*

Accepted 2014 January 20. Received 2014 January 17; in original form 2013 September 18

ABSTRACT
We study the $z = 0$ properties of clusters (and large groups) of galaxies within the context of interacting and non-interacting quintessence cosmological models, using a series of adiabatic SPH simulations. Initially, we examine the average properties of groups and clusters, quantifying their differences in ΛCDM, uncoupled Dark Energy (uDE) and coupled Dark Energy (cDE) cosmologies. In particular, we focus upon radial profiles of the gas density, temperature and pressure, and we also investigate how the standard hydrodynamic equilibrium hypothesis holds in quintessence cosmologies. While we are able to confirm previous results about the distribution of baryons, we also find that the main discrepancy (with differences up to 20%) can be seen in cluster pressure profiles. We then switch attention to individual structures, mapping each halo in quintessence cosmology to its ΛCDM counterpart. We are able to identify a series of small correlations between the coupling in the dark sector and halo spin, triaxiality and virialization ratio. When looking at spin and virialization of dark matter haloes, we find a weak (5%) but systematic deviation in fifth force scenarios from ΛCDM.

Key words: methods:N-body simulations – galaxies: haloes – cosmology: theory – dark matter

1 INTRODUCTION

Galaxy clusters are the largest bound objects in the Universe, with properties arising from the complex interplay between large scale gravitational dynamics and gas physics. For this reason, they provide a unique laboratory for probing cosmological models on astrophysical scales, and hence to constrain the nature of dark energy (see e.g. Samushia & Ratra 2008; Abdalla et al. 2010; Carlesi et al. 2011; De Boni et al. 2011; Baldi 2012; Allen et al. 2011; Bisnovatyi-Kogan & Chernin 2012). Due to the intrinsic complexity of the processes involved, to gain theoretical insight into the formation and evolution of galaxy clusters, we have to employ computationally expensive hydrodynamical N-body simulations (see Kravtsov & Borgani 2012, for a comprehensive review), and in recent years this approach has been successfully used to describe a large number of observational properties such as X-ray temperatures, gas fractions, Sunyaev-Zel'dovich effect and pressure profiles (Nagai et al. 2007; Croston et al. 2008; Arnaud et al. 2010; Sembolini et al. 2013).

In an initial study Carlesi et al. (2013) (hereafter Paper I) we studied the relation between haloes and their environment, in this work we turn to basic properties of galaxy clusters in the framework of interacting and non-interacting quintessence cosmologies; such cosmologies have been developed to solve the fine-tuning problems of ΛCDM (see Wetterich 1995; Caldwell et al. 1998; Zlatev et al. 1999; Amendola 2000; Mangano et al. 2003) and their observational properties have been constrained in the background and linear regime (Amendola & Quercellini 2003; Pettorino et al. 2012; Chiba et al. 2013), as well as in the highly non-linear regime by means of N-body simulations (Macciò et al. 2004; Nusser et al. 2005; Baldi & Pettorino 2011; Baldi 2012; Li & Barrow 2011; Baldi & Salucci 2012; Carlesi et al. 2012). In this paper, we will further examine our cosmological simulations, including standard ΛCDM, a free quintessence model with a Ratra-Peebles (Ratra & Peebles 1988) self interaction potential (uDE, uncoupled Dark Energy) and three quintessence models interacting with the dark matter sector (coupled Dark Energy, cDE033, cDE066 and cDE099). The latter set of cDE models all implements a Ratra-Peebles scalar field potential and differ in the value of the coupling parameter β_c only.

Our aim is to establish links between this class of models and a set of observable properties of galaxy clusters, firstly grouping the clusters of galaxies in each simulation into homogeneous samples and link their properties to the cosmological framework. We also focus on individual structures, cross-correlating them across the different simulations and understanding how these dark energy models influence their properties on an object-by-object basis. In practice, this will reveal how structures forming from the same initial conditions, and hence in similar environments, are affected by the global cosmological model.

⋆ E-mail: edoardo.carlesi@uam.es

Table 1. Values of the coupling and potential used for the uDEand cDE models.

Model	V_0	α	β_c
uDE	10^{-7}	0.143	–
cDE033	10^{-7}	0.143	0.033
cDE066	10^{-7}	0.143	0.066
cDE099	10^{-7}	0.143	0.099

The paper is structured as follows: In Section 2 we will briefly introduce the physics of the models as well as their implementation in an N-body code. Section 3 discusses some of the most important features characterizing galaxy clusters in uDE and cDE scenarios, while in Section 4 we cross correlate them. In Section 5 we present a summary of our most important findings and outline the future directions of our work.

2 MODELS AND SIMULATIONS

Here, we briefly review some of the general mathematical features of the models studied and their numerical implementation. We refer the reader to Paper I and references therein for a more detailed discussion.

2.1 Cosmological models

Quintessence is a form of dark energy based on a cosmological scalar field, ϕ, with a Lagrangian that takes the form:

$$L = \int d^4x\sqrt{-g}\left(-\frac{1}{2}\partial_\mu\partial^\mu\phi + V(\phi) + m(\phi)\psi_m\bar{\psi}_m\right) \quad (1)$$

where we allow ϕ to interact with the matter field ψ_m through the dark matter particles' mass term, $m(\phi)\psi\bar{\psi}$.

The focus of this present study are interacting and non-interacting quintessence models with a so called Ratra-Peebles (see Ratra & Peebles 1988) self interaction potential:

$$V(\phi) = V_0\left(\frac{\phi}{M_p}\right)^{-\alpha} \quad (2)$$

where M_p is the Planck mass while V_0 and α are two constants whose values can be fixed by fitting the model to observational data (see Wang et al. 2012; Chiba et al. 2013). While in uDE the mass term in Eq. (1) is $m(\phi) = m_0$, with no interaction taking place in the dark sector; in the latter class of models we assume that the masses of dark matter particles evolve according to:

$$m(\phi) = m_0\exp\left(-\beta_c(\phi)\frac{\phi}{M_p}\right) \quad (3)$$

causing an energy transfer from DM to DE due to the minus sign in front of the coupling. In our simulations we have assumed a constant interaction term $\beta_c(\phi) = \beta_{c0}$.

2.2 N-body settings

Implementing quintessence into a standard N-body solver requires a series of modifications that depend on the nature of the specific model. Under the assumption of a very light scalar field, dark energy clustering can be neglected, so that quintessence only acts at the background level, leading to a different rate of expansion with respect to the standard ΛCDM case. While accounting for the changes in $H(z)$ is sufficient to properly simulate uDE cosmology, cDE models require a few additional modifications to be introduced, to take into account fifth force effects on the dark matter sector.

Table 2. Cosmological parameters at $z = 0$ used in the ΛCDM, uDE, cDE033, cDE066 and cDE099 simulations.

Parameter	Value
h	0.7
n	0.951
Ω_{dm}	0.224
Ω_b	0.046
σ_8	0.8

We implemented these features into the Tree-PM code `GADGET-2` (Springel 2005) following the algorithm of Baldi et al. (2010). To improve computational efficiency, $H(z)$, $m(z)$ and $\phi(z)$ are being read from a series of user provided tables and not calculated "on the fly", generating them using a customized version of the Boltzmann solver, `CMBEASY` (Doran 2005). Proper initial conditions that take into account modified power spectra and growth factors have been generated suitably modifying the `N-GenIC` code, for 2×1024^3 gas and dark matter particles in a $250h^{-1}\,\mathrm{Mpc}$ box. Gas physics has been simulated using the publicly available SPH solver of `GADGET-2`, smoothing over $N_{sph} = 40$ nearest neighbours to obtain the continuous fluid quantities and assuming a standard adiabatic relation $P \propto \rho^\gamma$ with $\gamma = \frac{5}{3}$, thus neglecting radiative effects. All of the non-standard implementations have been carefully tested, to ensure that the new numerical techniques do not introduce systematic errors.

2.3 Halo catalogues

Bound structures in our simulations have been identified using `AHF` [1](Gill et al. 2004; Knollmann & Knebe 2009), which has been modified to take into account the influence of the different cosmologies. We use the equation

$$M_\Delta = \Delta\times\rho_c(z)\times\frac{4\pi}{3}R_\Delta^3. \quad (4)$$

to define M_Δ as the total mass enclosed within a radius containing an average overdensity of Δ times the critical density of the universe (which needs to be properly taken into account in each different cosmological model).

From the sample of haloes identified this way we restricted our analysis to the virialized structures satisfying

$$\frac{2K}{|U|} - 1 < 0.5 \quad (5)$$

where K is the kinetic and U the potential energy (Prada et al. 2012). We therefore ensure that unrelaxed structures (probably undergoing major mergers) do not bias our analysis. Even though this can be used in combination with other criteria (Macciò et al. 2007; Prada et al. 2012), we checked that their implementation would not affect our sample and thus adopted exclusively this one. We also mention here that we do not expect the above condition to introduce any systematic bias into our object samples drawn from the

[1] `http://www.popia.ft.uam.es/AHF`

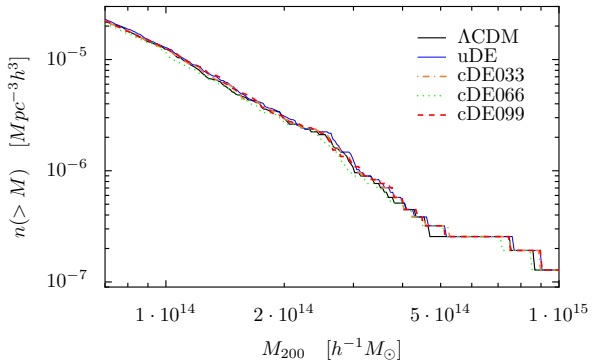

Figure 1. Cluster mass function for ΛCDM, uDE, cDE033, cDE066 and cDE099. Although the statistics in this mass regime is small, abundances are very similar for all the models.

Table 3. Number of (relaxed) galaxy clusters and large groups at $z = 0$ for different mass thresholds, found in the ΛCDM, uDE, cDE033, cDE066 and cDE099 simulations.

Model	$N(> 7 \times 10^{13} h^{-1}\mathrm{M}_\odot)$	$N(> 10^{14} h^{-1}\mathrm{M}_\odot)$
ΛCDM	338	190
uDE	350	198
cDE033	334	193
cDE066	321	178
cDE099	340	193

cDE simulations: even though – as we will be discussed in Section 4.1 – additional couplings in the dark sector introduce a shift into the standard virial relation, this effect is of the order $\approx 5\%$ and thus negligible with respect to the size of the deviations removed using Eq. (5).

3 GENERAL PROPERTIES OF GALAXY CLUSTERS

We first study properties of structures with mass $M > 7 \times 10^{13} h^{-1}\mathrm{M}_\odot$, which in our simulations are composed of more than 10^5 dark matter and gas particles. This sample includes both clusters and large groups, and we will either use the whole set or a smaller subset of it depending on the kind of properties to be analyzed. In fact, due to the sharp decline of the upper end of the cumulative halo mass function (shown in Fig. 1), a 30% reduction in the mass threshold leads to a twofold increase in the cumulative number of objects, which can be useful for statistical purposes. Complementary to the cumulative mass function (Fig. 1) we also list the total number of clusters and large groups in each cosmology in Table 3. It is evident that different models deliver very similar results (as discussed in Paper I), although we probably need a larger computational volume for a proper quantification of the magnitude of this effect, minimizing the impact of cosmic variance.

3.1 $T_X - M$ relation

Cluster X-ray temperatures are an extremely important observational proxy for halo mass (Ettori et al. 2004; Muanwong et al. 2006; Nagai et al. 2007) to which they are related via a scaling relation of the form

$$M(T_X) = M_0 \left(\frac{T_X}{3keV}\right)^\alpha \tag{6}$$

where theoretical models (Kaiser 1986; Navarro et al. 1995) predict $\alpha \approx \frac{3}{2}$. We can estimate X-ray temperatures for our simulated objects using three different definitions of T, namely, the mass-weighted temperature T_{mw}, the emission-weighted temperature T_{ew} and the spectroscopic-like temperature (Mazzotta et al. 2004) T_{sl} which reads:

$$T_{mw} = \frac{\sum_i m_i T_i}{\sum_i m_i} \tag{7}$$

$$T_{ew} = \frac{\sum_i m_i \rho_i T_i \Lambda(T_i)}{\sum_i m_i \rho_i \Lambda(T_i)} \tag{8}$$

$$T_{sl} = \frac{\sum_i m_i \rho_i T_i^{1/4}}{\sum_i m_i \rho_i T_i^{-3/4}} \tag{9}$$

where T_i, ρ_i and m_i are the i^{th} gas particle temperature, mass and density, while $\Lambda(T_i)$ is the cooling function, which we assumed to be $\propto T^{1/2}$ (thermal Bremsstrahlung). Only particles of $T > 0.5keV$ are included in the computation of the cluster temperatures, to remove the effect of cold flows. In Fig. 2 we show the temperature mass relations for objects larger than $7\times10^{13}h^{-1}\mathrm{M}_\odot$, from which we can see that all the models, regardless of the temperature definition, closely follow the same $M-T$ relation of Eq. (6). This equation has been fitted using M_{500} (which is closely related to the observations Sembolini et al. (2013)) and the three different definitions of T introduced before. In the case of ΛCDM these values are compatible with the findings of Allen et al. (2001); Ettori et al. (2002); Nagai et al. (2007) and Ventimiglia et al. (2008). It is quite clear that the impact of quintessence on this relation is completely negligible. Although, as we will discuss later, cDE models have different effects on the properties and distribution of baryons inside galaxy clusters, it is evident that the scaling of the X-ray temperature with the mass is not affected in the class of quintessence theories under investigation here. This might be due to the integrated nature of the relation, which conceals the details of the underlying matter distribution of each object.

3.2 Radial dark matter profiles

As reported by Baldi et al. (2010); Li & Barrow (2011), the Navarro Frenk White (NFW) profile (Navarro et al. 1996);

$$\rho(r) = \frac{\rho_0}{\frac{r}{r_s}\left(1+\frac{r}{r_s}\right)^2} \tag{10}$$

provides a good description of the distribution of dark matter inside virialized haloes also in the framework of cDE cosmologies. While in Paper I we already presented an analysis of density profiles for a large number of low mass haloes, our focus here lies with the internal structure of a few, well resolved objects. We fit each (relaxed) halo using the radial density profiles computed by AHF, which provides dark matter density for logarithmically spaced bins assuming a spherically symmetrical distribution. We then compute for each halo the corresponding goodness-of-fit Δ^2 (Springel et al. 2008), defined as

$$\Delta^2 = \frac{1}{N_{bins}} \sum_{i=1}^{N_{bins}} (\log_{10}(\rho_i^{(\mathrm{th})}) - \log_{10}(\rho_i^{(\mathrm{num})}))^2 \tag{11}$$

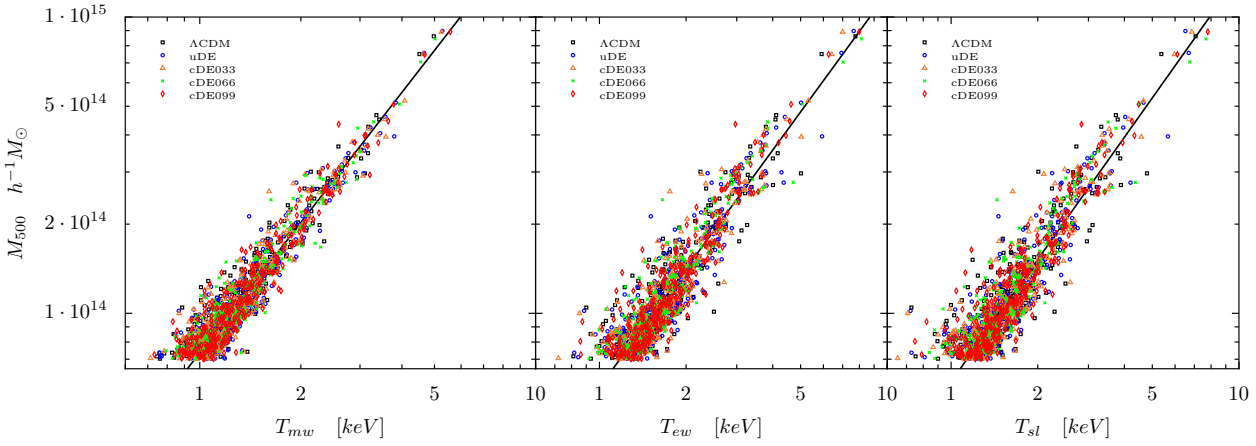

Figure 2. Mass weighted, emission weighted and spectroscopic like temperatures versus M_{500} for objects above $7 \times 10^{13} h^{-1}\mathrm{M}_\odot$in all simulations. The solid black lines represents the best fit $M - T$ power law relation for ΛCDM, which closely followed by all cosmological models.

Table 4. Best-fit values to the $M - T_X$, obtained fitting Eq. (6) using M_{500} versus the three temperature definitions T_{mw}, T_{ew} and T_{sl} definitions. The M_0s are given in units of $10^{13} h^{-1}\mathrm{M}_\odot$. All the models follow closely ΛCDM, making this kind of relation a poor proxy for quintessence detection.

Model	M_0^{mw}	α^{mw}	M_0^{ew}	α^{ew}	M_0^{sl}	α^{sl}
ΛCDM	6.31 ± 0.08	1.46 ± 0.03	4.89 ± 0.09	1.33 ± 0.03	5.09 ± 0.09	1.37 ± 0.04
uDE	6.21 ± 0.09	1.47 ± 0.03	4.85 ± 0.07	1.33 ± 0.03	5.05 ± 0.07	1.38 ± 0.03
cDE033	6.29 ± 0.09	1.46 ± 0.03	4.81 ± 0.07	1.36 ± 0.03	4.95 ± 0.08	1.37 ± 0.04
cDE066	6.31 ± 0.08	1.46 ± 0.03	4.96 ± 0.09	1.34 ± 0.03	5.19 ± 0.09	1.38 ± 0.04
cDE099	6.27 ± 0.07	1.45 ± 0.03	4.80 ± 0.09	1.37 ± 0.03	5.03 ± 0.07	1.41 ± 0.03

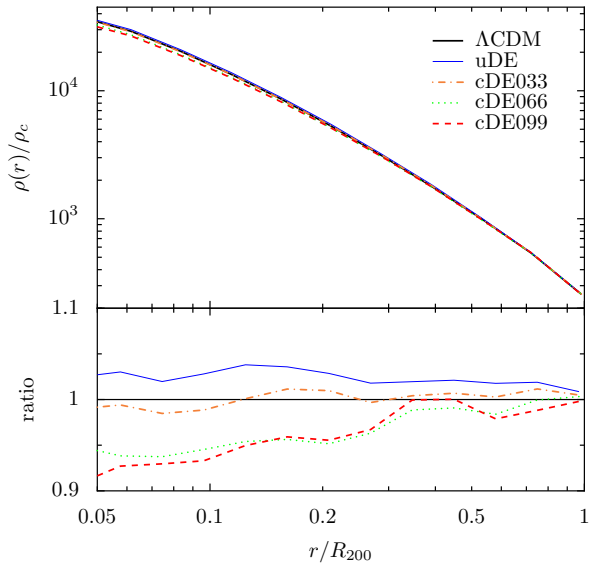

Figure 3. Average dark matter density profile for virialized clusters above 10^{14} as a function of radius. The additional interaction tends to reduce densities towards the halo center, as we can clearly see in cDE099 and cDE066.

where the ρ_i's are the numerical and theoretical densities in units of the critical density ρ_c at the i^{th} radial bin.

From the distribution of Δ^2 (not shown here) we can deduce that no substantial difference can be seen in the different cosmologies, that is, the NFW formula of Eq. (10) describes (on average) equally well dark matter halo profiles in ΛCDM as in the other (coupled) dark energy models – something already presented in Paper I, but now extended to larger masses.

We complement this finding with Fig. 3 where we show $\rho(r)/\rho_c$ averaged over all our objects with $M > 10^{14} h^{-1}\mathrm{M}_\odot$ as a function of distance to the halo centre in units of R_{200}: there, however, it is evident that the innermost regions of the largest cDE clusters are associated with densities $\approx 10\%$ lower than the ΛCDM value. This phenomenon has also been observed and explained – in a different mass range – by Baldi et al. (2010), who attributed it to the extra friction caused by the interaction of dark energy and dark matter, which adds up to the particles' velocities causing a small relative expansion of the halo.

3.3 Radial gas profiles

Due to their large size, galaxy clusters are considered to be a "fair sample" of the Universe, and thus should contain a fraction of baryons close to the cosmic baryon fraction given by Ω_b/Ω_m, where Ω_b measures the total baryonic and Ω_m the total non-relativistic matter content. Acting on the cosmic expansion and thus indirectly on the collapse and formation of large structures, we can expect quintessence to leave an imprint in the gas distribution within them. The relation between dynamical dark energy and the baryon content of clusters has been studied by Samushia & Ratra (2008) where they obtained constrains on the slope of the Ratra-Peebles potential (cf. Eq. (2)). Gas dynamics and abundance in coupled dark energy cosmologies have also been studied on slightly

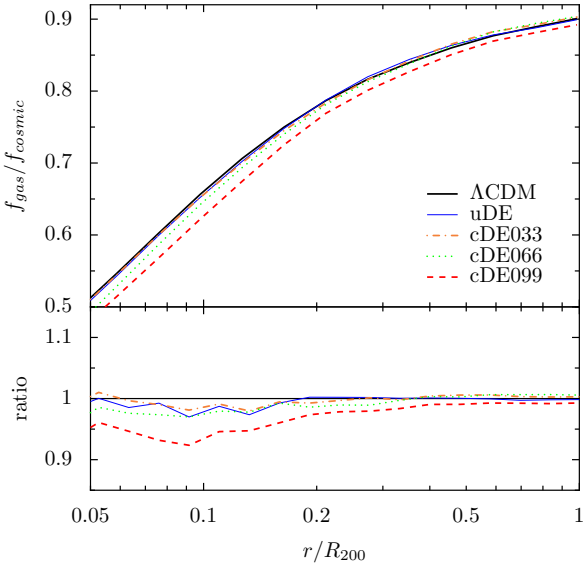

Figure 4. Gas fraction in units of the cosmic baryon fraction as a function of radius averaged for clusters above $10^{14}h^{-1}\mathrm{M}_{\odot}$. We observe that the suppression in the value of the gas fraction is stronger towards the central regions and increases with β_c. However, weakly interacting cDE033 and uncoupled uDE are substantially indistinguishable from the standard cosmological model.

different cosmological scales by Baldi et al. (2010); Baldi & Viel (2010); Baldi (2011), finding a correlation between baryon fractions and scalar field coupling to DM.

Here we add to these studies by analyzing the radial distribution of gas and its properties like density, temperature and pressure, focusing on structures with $M_{200} > 10^{14}h^{-1}\mathrm{M}_{\odot}$ again, which are composed of more than 3×10^5 gas and DM particles and hence allow us to adequately resolve their internal structure.

Gas fractions In Fig. 4 we show

$$f_{gas} = \frac{M_{gas}(< r)}{M_{tot}(< r)} \tag{12}$$

in units of the cosmic baryonic fraction and averaged over the ≈ 180 most massive galaxy cluster in each simulation. Our ΛCDM results are in agreement with e.g. Sembolini et al. (2013), who found identical results for the shape of $f_{gas}(r)$ in a set of adiabatic ΛCDM clusters. However we clearly observe that the net effect of the coupling is to reduce the baryon content of the cluster in proportion to the value of β_c. The suppression is stronger towards the central regions of the cluster, where the average suppression is $\approx 7\%$ for cDE099 and $\approx 5\%$ in cDE066, while cDE033 and uDE follow closely the values of ΛCDM. At larger radii all results tend to converge to the ΛCDM value of f_{gas}, which is slightly below the value of the cosmic baryon fraction $\Omega_b/\Omega_m = 0.17$. However, we must stress again that due to the absence of radiative cooling these profiles are useful only as far as they allow us to provide a first estimate of the impact of coupling in the dark sector on the (radial distribution of the) gas content of galaxy clusters. And in that regards, our results are in qualitative agreement with the findings of Baldi et al. (2010); Baldi (2011), who also established a link between fifth force and lower baryon fractions for various classes of interacting models, including non-constant coupling models and with different types of self-interaction potentials.

Table 5. Best-fit values to Eq. (14) for the gas density profile averaged over galaxy clusters of $M_{200} > 10^{14}h^{-1}\mathrm{M}_{\odot}$. The core radii r_c and r_s are given in units of R_{200}.

Model	β	r_c	r_s	ϵ
ΛCDM	0.43 ± 0.01	0.058 ± 0.002	0.40 ± 0.05	0.41 ± 0.05
uDE	0.41 ± 0.01	0.056 ± 0.002	0.34 ± 0.07	0.38 ± 0.05
cDE033	0.41 ± 0.02	0.053 ± 0.002	0.33 ± 0.07	0.36 ± 0.08
cDE066	0.39 ± 0.01	0.053 ± 0.003	0.33 ± 0.05	0.36 ± 0.05
cDE099	0.42 ± 0.02	0.064 ± 0.004	0.36 ± 0.05	0.35 ± 0.04

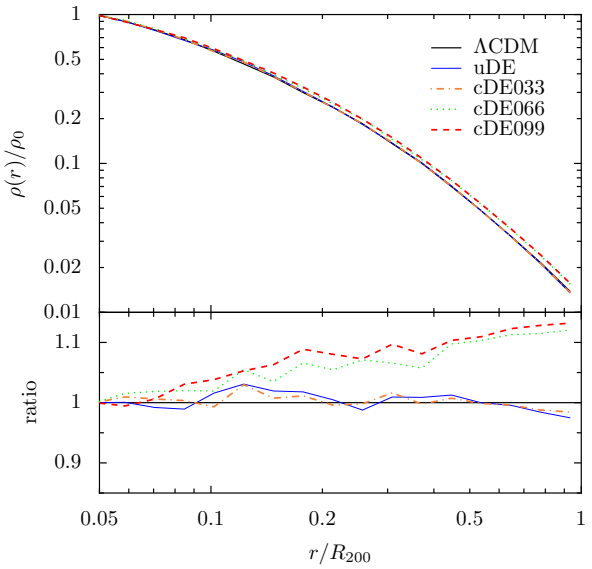

Figure 5. Radial distribution of gas density averaged for clusters above $10^{14}h^{-1}\mathrm{M}_{\odot}$, normalized to the central density ρ_0.

This effect, called baryon segregation, was first analyzed and described in detail in the works of Mainini (2005) and Mainini & Bonometto (2006), where it was explained in terms of the different species' infall velocity towards the centre of the potential well in a spherical top-hat fluctuation. In fact, this happens to be faster for DM than for baryons, since the coupling adds to the gravitational pull in that drives the collapse of the dark matter overdensity. Therefore, gas particles will be relatively less abundant around the central parts of the halo, where they are to be accreted at a slower pace, while their presence in the outer layers is only negligibly affected by this phenomenon.

Density profile After studying how the baryon fraction (which is a combination of gas and dark matter properties) is affected we consider whether the coupling also induces sizeable effects in the gas density profile alone. Under the assumption of hydrostatic equilibrium (which holds to the same degree in both quintessence models and ΛCDM – as we will see in Section 3.5 below) we can derive a simple functional form for the gas density profile (Cavaliere &

Fusco-Femiano 1976), the so called β^2 model:

$$\rho(r) = \rho_0 \left(1 + \left(\frac{r}{r_c}\right)^2\right)^{-\frac{3}{2}\beta} \quad (13)$$

where r_c is the core radius and ρ_0 is the inner cluster density, which is defined as $\rho(r = 0.05 \times R_{200})$. Observations (Vikhlinin et al. 1999) and simulations (Rasia et al. 2004) have shown that Eq. (13) does not simultaneously reproduce both the inner and outer parts of density distribution of galaxy clusters, even though this model can still be used as a valuable theoretical tool that captures the main characteristics of the intra-cluster medium (ICM) (Arnaud 2009). Hence, for a quantitative comparison of the results for radial distribution of gas densities in the different cosmologies we refer here to a model proposed by Mroczkowski et al. (2009). This was developed for the observational description of X-ray cluster profiles, and is based on the formula proposed in (Vikhlinin et al. 2006), which in turn is an extension of the simple β model. Here we re-write Eq. (13) as:

$$\frac{\rho(r)}{\rho_0} = \frac{1}{\left(1 + \frac{r^2}{r_c^2}\right)^{\frac{3}{2}\beta}} \times \frac{1}{\left(1 + \frac{r^3}{r_s^3}\right)^{\epsilon}} \quad (14)$$

where the additional multiplicative term on the right contains a new scale radius r_s and power law ϵ, which capture the departure from the standard β model at larger radii. We then compute the average $\rho(r)/\rho_0$ per radial bin (in units of R_{200}), again using all clusters of $M_{200} > 10^{14}h^{-1}\mathrm{M}_\odot$. We check that Eq. (14) holds for all the models verifying that the corresponding goodness of fits take comparable values (analogously defined to Eq. (11)); and in Table 5 we show the best-fit parameters; note that we defer from showing the best-fit curves in Fig. 5 again to not overload the plot. The parameters do not seem to show any trend for cDE and uDE models, except for a slightly shallower outer slope ϵ in coupled cosmologies which can be also seen in Fig. 5 where we present the averaged radial gas distribution. We also notice that for our objects β is substantially lower than usually assumed (≈ 0.66), however, this can be easily explained by the fact that our model has two different slopes to account for the two different regimes: this means that, being biased by the core regions of the cluster, where the decrease in density is shallower, β will consequently be smaller.

Fig. 5 further shows clearly that – away from the center of the clusters – the cDE066 and cDE099 gas densities increasingly diverge from the other models, up to more than 10% at the outer edge. As discussed earlier, using the theoretical framework of Mainini (2005); Mainini & Bonometto (2006), these models are characterized by lower baryon fractions in the central regions of the clusters (i.e. a smaller ρ_0, according to our definition) which on the other hand converge to ΛCDM, cDE033 and uDE in the outer regions. Hence, divergences in $\rho(r)$ for $r \to R_{200}$ are explained by the small denominator ρ_0, enhancing even more the gap between the predictions of coupled quintessence cosmologies and the standard model.

Pressure profiles Having analyzed the properties of baryon density distributions, we now consider the pressure profiles, which can be modeled assuming a simple adiabatic relation of the type

$$P(r) = P_0 \rho_{gas}^{\gamma}(r) \quad (15)$$

[2] This β must not be confused with β_c, the coupling parameter

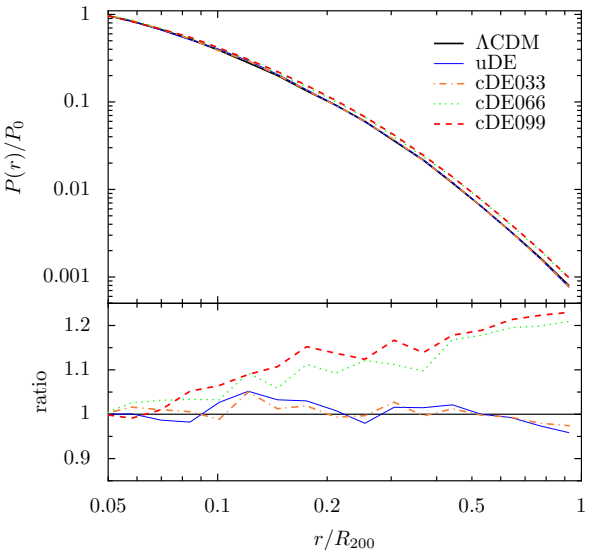

Figure 6. Pressure profiles averaged over clusters above $10^{14}h^{-1}\mathrm{M}_\odot$.

where P_0 is an arbitrary normalization constant (which we take to be equal to $P(0.05 \times R_{200})$), and $\gamma = 5/3$ for the case of an adiabatic gas – as assumed in our simulations. Using the densities computed in the previous sub-section, it is straight-forward to obtain the pressure profiles by using Eq. (15); the results are plotted in Fig. 6. It is remarkable that the differences among the models are now much larger (note the enlarged range in the ratio plot), since the discrepancies observed previously are now basically amplified by the adiabatic index γ. Again, this effect increases towards the outer halo edge, where the ratio of $\rho_{gas}(r)$ to the inner density ρ_0 is larger in cDE models due to the under-abundance of gas in the central regions.

Qualitatively, the shapes in Fig. 6 reproduce well the so-called universal pressure profile of galaxy clusters, which can be reconstructed using Sunayev-Zel'dovich effect and X-ray data (Arnaud et al. 2010; Bonamente et al. 2012; Planck Collaboration et al. 2013). However, the errors on the observational results are still larger than the spread among the different models considered here so that for the moment it is not possible to use these dataset to directly constrain quintessence. Moreover, a direct comparison to the data would probably require to relax the unrealistic assumption of completely adiabatic gas and introduce additional effects (such as radiative cooling, star formation, and AGN feedback) to properly simulate the gas physics. In any case, it is clear that gas pressure in cluster does represent an important probe for cDE cosmologies, as the non-linear relation between gas and pressure significantly magnifies the prediction of scarcer gas in the core regions characteristic of these cosmological models.

Temperature profiles Observations have shown (Markevitch et al. 1998; Vikhlinin et al. 2005, e.g.) that galaxy clusters have a declining temperature towards larger radii, in contrast with the simplest isothermal models. The same pattern is seen in our simulations, as the curves in Fig. 7 show, and is in qualitative agreement with the findings of Vikhlinin et al. (2006); Arnaud et al. (2010); Baldi et al. (2012). However, it is known that adiabatic SPH simulations fail to reproduce the inner cool core of galaxy clusters (Kravtsov & Borgani 2012) up to a value of $\approx 0.2 \times R_{200}$; this point is marked by a vertical dotted line in Fig. 7.

Table 6. Best fit values to a linear relation for the outermost values of the temperature profile. The vertical dashed line denotes the innermost excluded region, where the linear relation does not hold.

Model	A	B
ΛCDM	1.05 ± 0.01	0.61 ± 0.02
uDE	1.10 ± 0.01	0.61 ± 0.02
cDE033	1.10 ± 0.01	0.61 ± 0.02
cDE066	1.11 ± 0.02	0.59 ± 0.01
cDE099	1.11 ± 0.02	0.59 ± 0.01

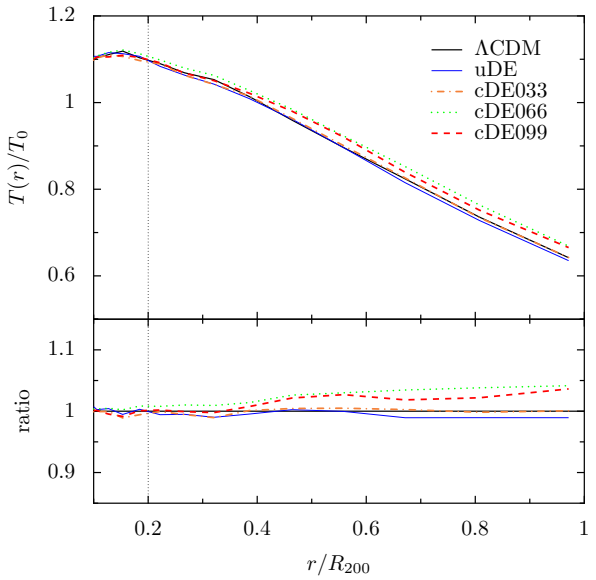

Figure 7. Temperature profiles averaged over clusters above $10^{14}h^{-1}\mathrm{M}_\odot$.

Following De Grandi & Molendi (2002) and Leccardi & Molendi (2008) we model the outer parts of galaxy clusters using a linear function

$$\frac{T(r)}{T_0} = A - B\left(\frac{r}{R_{200}} - 0.2\right) \tag{16}$$

where A and B are two free parameters and T_0 is the average temperature for each cluster. We proceed identifying all structures above $10^{14}h^{-1}\mathrm{M}_\odot$ and fitting Eq. (16) using the gas densities and temperatures for regions of $r > 0.2 \times R_{200}$. The best-fit values are presented in Table 6 while only the numerical results are plotted in Fig. 7. The five profiles are very similar and the largest differences can be seen in the strongest coupled cases of cDE066 and cDE099, where the scaled temperature at the halo edge is $\approx 5\%$ larger than in the other models. However, all the points as well as the best-fit values are still consistent within the error so that this small difference is considered to be not significant. The effect of the coupling is thus marginal in this case, and it seems unlikely that radial temperature measurements alone can provide a mean to distinguish amongst at least the models considered here.

3.4 Gas alignment to the dark matter halo

We now extend our study to the full 3D distribution of the gas inside the halo, i.e. we are considering the shape of the gas particles spatial distribution. To this extent, we utilize the inertia tensor

$$I_{ij}^{\mathrm{gas}} = \sum_{n_{\mathrm{gas}}} x_{(n),i}^{\mathrm{gas}}\ x_{(n),j}^{\mathrm{gas}} \tag{17}$$

where $x_{(n),i}^{\mathrm{gas}}$ is the position vector relative to the center of the baryon mass distribution of the n^{th} particle. In the same way we write the halo's inertia tensor

$$I_{ij}^{\mathrm{dm}} = \sum_{n_{\mathrm{dm}}} x_{(n),i}^{\mathrm{dm}}\ x_{(n),j}^{\mathrm{dm}} \tag{18}$$

which is now given by summing over dark matter particles only. We then diagonalize the two tensors using the two largest eigenvectors $\mathbf{e}_1^h$ and $\mathbf{e}_1^b$ – which are the major axes of the dark matter and baryon distribution, respectively – in what follows. To check whether quintessence has an influence on the relative spatial distribution of gas and dark matter particles we compute

$$\cos\theta = \frac{\mathbf{e}_1^h \cdot \mathbf{e}_1^b}{|e_1^h e_1^b|} \tag{19}$$

for all clusters above $10^{14}h^{-1}\mathrm{M}_\odot$ again. The probability distribution of $\cos\theta$ is shown in Fig. 8, where we can see that all cosmological models follow the same pattern of close alignment between gas and dark matter distributions, although with some scatter among the models at small angles, where $\cos\theta \to 1$. We note here that our results refer to the gas properties only, and cannot be directly compared to Lee (2010) and Baldi et al. (2011), who looked at galaxy alignment.

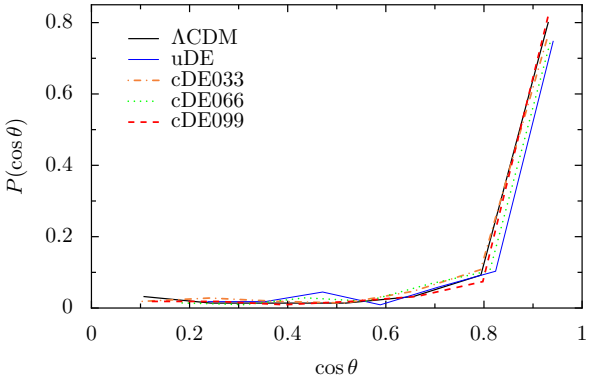

Figure 8. Average cosine of the alignment angle between the gas and dark matter major axes, averaged for objects with $M_{200} > 10^{14}h^{-1}\mathrm{M}_\odot$.

Table 7. Best fit values to a Gaussian distribution for the ΔM computed under the hypothesis of HSE. While all the models tend to produce similar results, we see that cDE099 has a narrower dispersion around the peak; yet the absence of a comparable effect in the other cDE models indicates that the correlation to the coupling is at best very weak.

Model	ΔM_0	σ
ΛCDM	0.23 ± 0.02	0.35 ± 0.03
uDE	0.24 ± 0.02	0.37 ± 0.04
cDE033	0.22 ± 0.02	0.36 ± 0.04
cDE066	0.23 ± 0.02	0.35 ± 0.03
cDE099	0.23 ± 0.02	0.28 ± 0.03

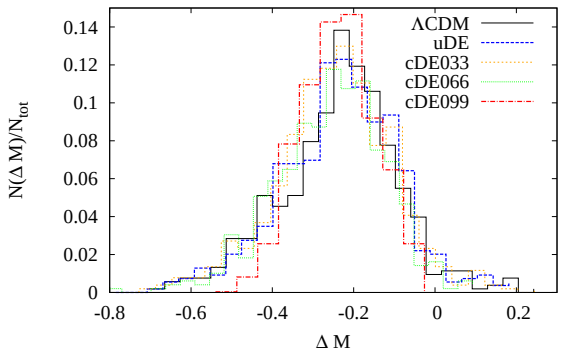

Figure 9. Distribution of $\Delta M = (M_{HSE,200} - M_{200})/M_{200}$, the difference between the cluster mass estimated using the hydrostatic equilibrium assumption and the true mass obtained in the simulations. We computed M_{HSE} for relaxed haloes of $M > 9 \times 10^{13} h^{-1}\mathrm{M}_{\odot}$. The distribution of ΔM is peaked around -0.12 for all models, showing no large deviation from the ΛCDM pattern neither in uDE nor in cDE cosmologies.

3.5 Hydrostatic equilibrium

Observations of galaxy clusters usually assume hydrostatic equilibrium (HSE) to derive their masses. Under this hypothesis, gas and galaxies are both in equilibrium with the binding cluster gravitational potential (Sarazin 1986; Evrard 1990; Bahcall & Lubin 1994). However, this assumption is not always valid and is a major source of uncertainty when deriving observational scaling relations. Many authors (e.g. Ameglio et al. 2009; Lau et al. 2009; Sembolini et al. 2013) found a systematic underestimation of cluster masses within the range $10 - 25\%$ for ΛCDM. This was explained by Lau et al. (2009) and identified as an effect driven by random gas motion that contribute to the pressure support, which in HSE is used to estimate the mass using the relation

$$M_{HSE}(< r) = -\frac{kT_{mw}r}{Gm_H\mu}\left(\frac{d\ln\rho}{d\ln r} + \frac{d\ln T}{d\ln r}\right). \qquad (20)$$

where k is the Boltzmann constant, T_{mw} is the mass weighted temperature, m_H is the hydrogen mass, μ is the hydrogen mass fraction and ρ is the gas density.

We are interested in examining the impact of alternative cosmological scenarios on the above estimation as the effective dark matter gravitational potential is affected by the presence of an additional interaction mediated by the dark energy. To accomplish this we identify relaxed clusters (as defined by Eq. (5)) of $M_{200} > \times 10^{14} h^{-1}\mathrm{M}_{\odot}$, and compute for each one of them the function $M_{HSE}(< r)$ using the temperature and pressure profiles. We can then straight-forwardly obtain an estimated total mass $M_{HSE,200}$ simply by using its value at the halo edge R_{200}, defined by Eq. (4).

The distribution of the fractional difference

$$\Delta M = \frac{M_{HSE,200} - M_{200}}{M_{200}} \qquad (21)$$

with respects to the true mass as returned by the halo finder is shown in Fig. 9, where we clearly see that this mass estimator has an average negative bias peaked around $\Delta M_0 = -0.22$ and a dispersion $\sigma = 0.34$ for all models (as shown in Table 7), except for cDE099 which shows a slightly more pronounced peak and a narrower dispersion around it. However, because of the absence of such a trend in the other cDE models and the non-negligible error bars, it appears more likely that this effect is due to a statistical fluctuation.

It is thus safe to state that uDE and cDE cosmologies are not responsible for any additional bias, even though the use of a larger halo sample containing more clusters with $M_{200} > 10^{15} h^{-1}\mathrm{M}_{\odot}$ might be needed to test whether this statement really holds at even higher mass scales.

4 CROSS-CORRELATED PROPERTIES OF GALAXY CLUSTERS

Due to our approach of using the same random phases for all models when generating the initial conditions for the simulations we are in the situation of cross-identifying the same objects in all the models. Therefore, focusing on structures forming in the same environments whose evolution is driven by different laws, we can shed more light into the effects of cosmic evolution on properties of individual objects and describe how they change when switching from one model to the other. Or put differently, while in the previous sections we primarily engaged in studying distribution functions, we are now directly testing the influence of our models onto individual objects.

The cross-correlation was performed matching every ΛCDM halo with $M_{200} > 7 \times 10^{13}$ with its counterpart, i.e. 338 haloes were sought in the other models (cf. Table 3). But this mass cut was only applied to the ΛCDM haloes and we were hence able to cross-match every of those ΛCDM haloes. To actually cross-identify objects we used a halo matching technique that correlates those ΛCDM haloes to the halo catalogue of the other models by examining the particle ID lists and maximizing the merit function $C = N_{\mathrm{shared}}^2/(N_1 N_2)$, where N_{shared} is the number of particles shared by two objects, and N_1 and N_2 are the number of particles in each object, respectively (e.g. Knebe et al. 2013).

For each pair we then compare M_{200}, virialization, spin parameter, mass weighted temperature and gas fraction. The results are all summarized in Fig. 10 and Table 8. Although most of these distribution look quite noisy and scattered about unity, theoretical considerations will give us a key to understand and interpret the (small) deviations observed – to be discussed in the following sub-sections. We only briefly note here that uDE haloes' parameter do not show, on average, any significant sign of deviation from ΛCDM.

4.1 Virialization

It is known that the degree of virialization of dark matter haloes with kinetic energy K and potential energy U, which is usually defined as

$$\left|\frac{U}{2K}\right| = 1 \qquad (22)$$

is affected by the presence of an additional coupling (Abdalla et al. 2010; He et al. 2010). In this case, due to the modification to the standard gravitational potential, the virial relation becomes

$$\left|\frac{U}{2K}\right| = \frac{1 - \xi/2}{1 - 2\xi} \qquad (23)$$

where the parameter ξ defined in Abdalla et al. (2010) can be written in terms of our definition of dark matter - dark energy coupling as:

$$\xi = \Omega_{dm}\beta_c. \qquad (24)$$

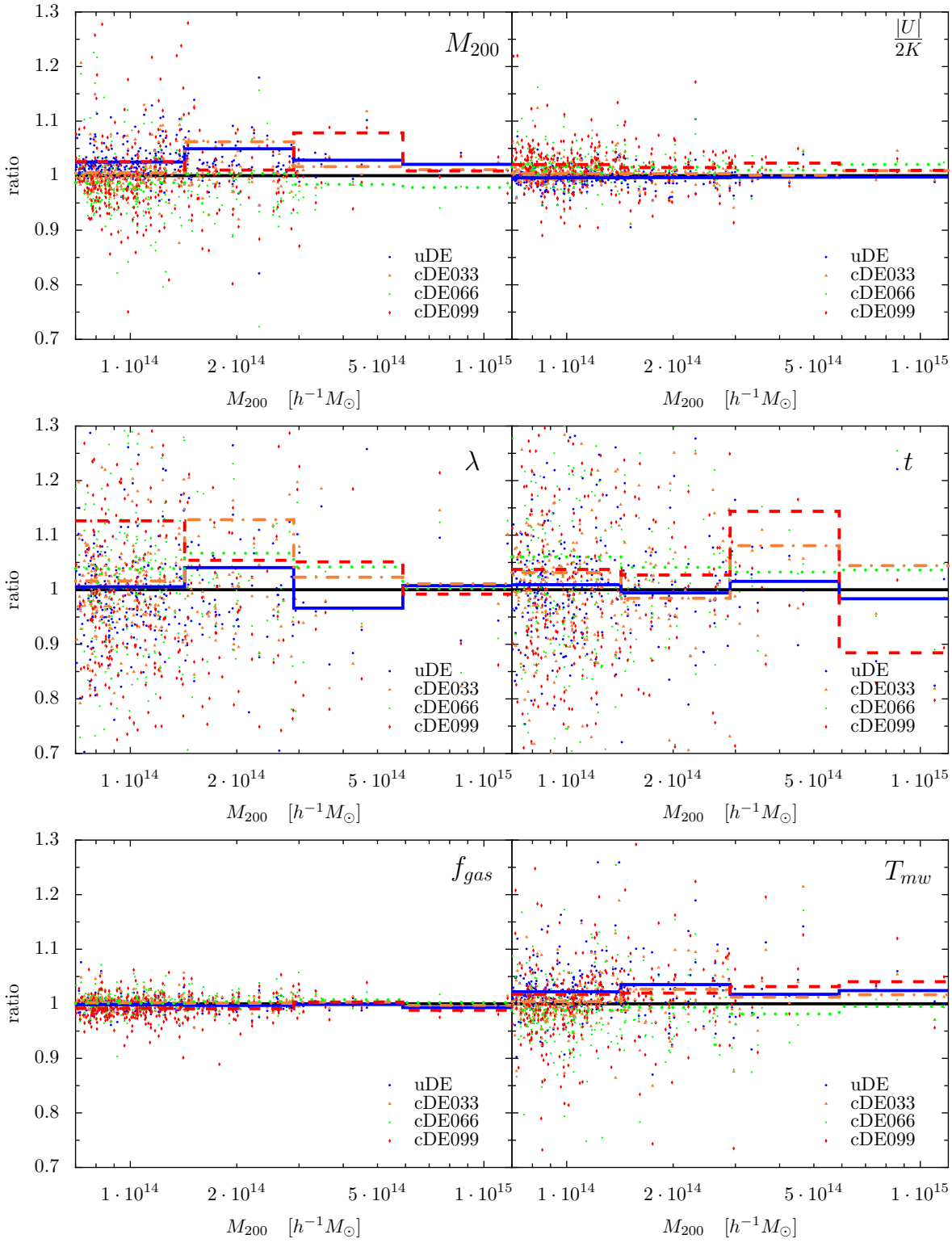

Figure 10. Halo and gas properties in quintessence models. Each dot represents the value of the ratio of the parameter in cDE or uDE to its cross correlated structures in ΛCDM. Upper panels: halo mass (left) and virialization (right). Central panel: halo spin (left) and triaxiality (right). Lower panel: gas fraction (left) and mass-weighted temperature (right).

Table 8. Average of the model to ΛCDM ratio for a series of cross correlated objects with their dispersion. M_{200} is the cross correlated halo mass, $|U|/(2K)$ the ratio of the virialization of each object, T_{mw} the mass weighted temperature, f_{gas} the gas content as a fraction of the total mass, λ the spin parameter and t the triaxiality parameter. Even though the scatter is significant, we can see a correlation of λ, t and virialization to the dark energy coupling, while the other parameters' average are largely independent of the model.

Parameter	uDE	cDE033	cDE066	cDE099
M_{200}	1.03 ± 0.01	1.03 ± 0.03	0.99 ± 0.02	1.04 ± 0.02
$\|U\|/(2K)$	0.997 ± 0.003	1.005 ± 0.005	1.015 ± 0.005	1.05 ± 0.01
T_{mw}	0.998 ± 0.002	1.015 ± 0.004	0.991 ± 0.006	1.03 ± 0.01
f_{gas}	1.029 ± 0.003	1.001 ± 0.001	1.002 ± 0.002	0.991 ± 0.006
λ	1.02 ± 0.04	1.06 ± 0.03	1.05 ± 0.03	1.10 ± 0.04
t	1.01 ± 0.04	1.03 ± 0.02	1.06 ± 0.03	1.05 ± 0.02

We can thus calculate the expected deviation from the standard relation and compare it to the results of Table 8. For cDE099, this value is 1.04, for cDE066 is 1.02 while in cDE033 the value is 1.01. The predictions for these very small deviations from the ΛCDM virial equilibrium are compatible with the average findings of the simulations presented in the upper panel of Fig. 10, although the large scatter does not allow us to draw clear conclusions on the matter. It is however remarkable that, although weak, we can find evidence of this modification.

4.2 Spin parameter

We use the spin parameter as defined by Bullock et al. (2001), i.e.

$$\lambda = \frac{L_{200}}{\sqrt{2} M_{200} V_{200} R_{200}} \tag{25}$$

where the quantities L (the total angular momentum), M (total mass), V (circular velocity) and R (radius) are computed using Eq. (4) with $\Delta = 200$. Our results (shown in the central panel of Fig. 10) indicate that this parameter is positively correlated to the coupling parameter β_c, as already found in the analysis of smaller haloes in cosmologies where dark matter feels an additional force (Hellwing et al. (2011), Paper I). For our models we find that λ in cDE haloes differs on average up to a $\approx 10\%$ from its ΛCDM cross-correlated partner, a result which is in good agreement with the findings of the aforementioned work.

4.3 Triaxiality

We know that the shape of three dimensional haloes can be modelled as an ellipsoidal distribution of particles (Jing & Suto 2002; Allgood et al. 2006), whose three axes are given by the eigenvectors of the inertia tensor defined in Eq. (18). Ordering the corresponding eigenvalues as $a \geqslant b \geqslant c$, we define the triaxiality parameter t [3] as

$$t = \frac{a^2 - b^2}{a^2 - c^2}. \tag{26}$$

In Table 8 we observe again a weak dependence of this parameter on β_c in cDE models. cDE haloes here differ to ΛCDM correlated ones by values up to 6%. This effect is not observed at lower masses (although not shown here), and – like in the previous case – the scatter is quite large so that we definitely need more statistics (i.e. simulations of larger volumes with the same mass resolution) to ensure this is a real feature of massive dark matter haloes in cDE models.

[3] We use t instead of the commonly used T to avoid any confusion with temperatures.

4.4 M_{200}, T_{mw} and f_{gas}

The last halo properties we cross-correlated are mass, gas fraction and mass weighted temperature, shown in the upper and lower panels of Fig. 10. The scatter in the first two is extremely small, with the ratios clustering around unity; T_{mw} on the other hand seem to vary more across models even though still very close to one. Moreover, no sign of dependence on the kind of quintessence or coupling seems to emerge. So, even though we observed that gas and dark matter are distributed differently, it is clear that the integral values of M_{200} and f_{gas} cannot be used as a proxy for these discrepancies. It is interesting to note how the gas fraction, which we found to be strongly correlated to the coupling parameter when projected radially, seems to be now unaffected by the interaction. However, this is not surprising, since a smaller abundance of gas in the central regions of the cluster is expected to have a negligible effect on the overall f_{gas}, due to the little relative weight of the innermost regions. In a typical cluster, the gas mass at $r = 0.1 \times R_{200}$ accounts for only a $3 - 4\%$ of the total, so that changes even as large as 10% only but slightly affect the global balance. In any case, the histories of accretion of these parameters may indeed vary, even bringing about the same results at $z = 0$, as found by Giocoli et al. (2013) in the context of other coupled quintessence models. The behaviour of this quantities at higher redshifts will be analyzed in an upcoming future work.

5 CONCLUSIONS

In this contribution we have studied the properties of clusters and large groups of galaxies using the set of hydrodynamical N-body simulations introduced an earlier work (Paper I). The models under consideration include a fiducial ΛCDM cosmology, an uncoupled Dark Energy (uDE) and three coupled Dark Energy (cDE) models. In each of them we have identified $\approx$ 330 structures with masses $M_{200} > 7 \times 10^{13} h^{-1} \mathrm{M}_{\odot}$ which we further subdivided into smaller subsets to best fit each one of our analysis purposes. The aim was to identify and possibly quantify systematic effects of interacting (cDE) and non-interacting (uDE) quintessence on properties of large and massive structures at $z = 0$, and hence providing a deeper understanding of the phenomenological consequences arising in the non-linear regime of this class of theories.

Our analysis was carried along two conceptually different lines, namely investigating general properties of the set of objects,

and then one-to-one comparisons of cross-identified haloes. The first, presented in Section 3, focused upon the determination of the average properties of structures by considering homogeneous samples of objects above a given mass cut. In this way we determined how observables generally behave in different cosmologies. While integrated properties of the clusters, such as the X-ray temperature-mass relation, tend to conceal any dependence on the model, a closer look at the internal structure reveals that cDE models tend to favour less concentrated dark matter haloes and gas fractions which are around 5% below ΛCDM in the innermost regions of the clusters. We interpret this result as a consequence of the reduction of dark matter density in the very same regions, which is also proportional to the coupling. In our case, the suppression is $\approx 10\%$, and is also related to an average increase of the same magnitude of the peak value of the scale radii distribution. This effect was described theoretically by Mainini (2005); Mainini & Bonometto (2006) and later found in N-body simulations for galaxy groups and small clusters by Baldi et al. (2010); Li & Barrow (2011).

The most remarkable findings, however, stem from the study of the radial gas density and pressure profiles. Although we have seen that the extended β model of Mroczkowski et al. (2009) and the observations of pressure profile of Arnaud et al. (2010) seem to be able to account for the numerical results to the same degree, cDE099 and cDE066 still show large differences at the outer cluster edge. In fact, since these properties are related to the ratio $\rho_{gas}(r)/\rho_0$, due to the smaller ρ_0 the ratio becomes larger when approaching R_{200}, and eventually leading to discrepancies $> 20\%$ for pressure profiles, which is so far the largest difference predicted by us and for our models, respectively.

In addition, we have checked that the standard linear relation for temperature profiles in the outskirts of the clusters holds also in the case of uDE and cDE. Even the scatter in the determination of the cluster mass under the hypothesis of hydrostatic equilibrium seems to be largely model independent. However, it remains to be confirmed whether these statements remain when taking into account a larger sample of (even) more massive haloes.

Furthermore, in Section 4 we focused upon individual structures and cross-correlated objects found in the ΛCDM model to their counterparts in the other models. This sort of exercise is strictly theoretical and is aimed at determining which properties of objects forming from comparable initial (Gaussian) conditions and ending up at $z = 0$ in similar environments are most affected and thus likely to keep trace of the cosmological history.

We established that, whereas masses, total gas fractions and mass weighted temperatures do not seem to be affected by cosmology, virialization, spin parameter and triaxiality seem to be dependent on the coupling in the dark sector, albeit only weakly. In particular, we observed that deviations from the standard virial relations are in agreement with the analytical values computed using the formula of Abdalla et al. (2010), while spins seem to follow the pattern found in Paper I at lower mass ranges.

To conclude, we have examined the impact of coupled dark energy in a series of galaxy group and cluster observables at $z = 0$. In some cases, we managed to establish a physical link between the key observational properties and the underlying modified physical laws. However, it is still necessary to study the way background quintessence and scalar field mediated interactions work at higher redshifts and on larger and more massive structures. This will be the focus of future contributions.

ACKNOWLEDGEMENTS

EC is supported by the *Spanish Ministerio de Economía y Competitividad* (MINECO) under grant no. AYA2012-31101, and Multi-Dark Consolider project under grant CSD2009-00064.

AK is supported by the *Spanish Ministerio de Ciencia e Innovación* (MICINN) in Spain through the Ramón y Cajal programme as well as the grants CSD2009-00064, CAM S2009/ESP-1496 (from the ASTROMADRID network) and the *Ministerio de Economía y Competitividad* (MINECO) through grant AYA2012-31101. He further thanks Jasmine Minks for another age.

GY acknowledges support from MINECO under research grants AYA2012-31101, FPA2012-34694, Consolider Ingenio SyeC CSD2007-0050 and from Comunidad de Madrid under ASTROMADRID project (S2009/ESP-1496).

The authors thankfully acknowledge the computer resources, technical expertise and assistance provided by the Red Española de Supercomputación.

This work was undertaken as part of the Survey Simulation Pipeline (SSimPL: ssimpluniverse.tk) and GFL acknowledges support from ARC/DP 130100117

We further acknowledge partial support from the European Union FP7 ITN INVISIBLES (Marie Curie Actions, PITN-GA-2011-289442).

All the simulations used in this work were performed in the Marenostrum supercomputer at Barcelona Supercomputing Center (BSC).

REFERENCES

Abdalla E., Abramo L. R., de Souza J. C. C., 2010, Phys. Rev. D, 82, 023508
Allen S. W., Evrard A. E., Mantz A. B., 2011, Ann.Rev.Astron.Astrophys., 49, 409
Allen S. W., Schmidt R. W., Fabian A. C., 2001, MNRAS, 328, L37
Allgood B., Flores R. A., Primack J. R., Kravtsov A. V., Wechsler R. H., Faltenbacher A., Bullock J. S., 2006, MNRAS, 367, 1781
Ameglio S., Borgani S., Pierpaoli E., Dolag K., Ettori S., Morandi A., 2009, MNRAS, 394, 479
Amendola L., 2000, Phys. Rev. D, 62, 043511
Amendola L., Quercellini C., 2003, Phys. Rev. D, 68, 023514
Arnaud M., 2009, A&A, 500, 103
Arnaud M., Pratt G. W., Piffaretti R., Böhringer H., Croston J. H., Pointecouteau E., 2010, A&A, 517, A92
Bahcall N. A., Lubin L. M., 1994, ApJ, 426, 513
Baldi A., Ettori S., Molendi S., Gastaldello F., 2012, A&A, 545, A41
Baldi M., 2011, MNRAS, 411, 1077
Baldi M., 2012, MNRAS, 420, 430
Baldi M., Lee J., Maccio A. V., 2011, Astrophys.J., 732, 112
Baldi M., Pettorino V., 2011, MNRAS, 412, L1
Baldi M., Pettorino V., Robbers G., Springel V., 2010, MNRAS, 403, 1684
Baldi M., Salucci P., 2012, JCAP, 2, 14
Baldi M., Viel M., 2010, MNRAS, 409, L89
Bisnovatyi-Kogan G. S., Chernin A. D., 2012, Ap&SS, 338, 337
Bonamente M., et al., 2012, New Journal of Physics, 14, 025010
Bullock J. S., Dekel A., Kolatt T. S., Kravtsov A. V., Klypin A. A., Porciani C., Primack J. R., 2001, ApJ, 555, 240
Caldwell R. R., Dave R., Steinhardt P. J., 1998, Physical Review Letters, 80, 1582

Carlesi E., Knebe A., Lewis G., Yepes G., Wales S., 2013
Carlesi E., Knebe A., Yepes G., Gottlöber S., Jiménez J. B., Maroto A. L., 2011, MNRAS, 418, 2715
Carlesi E., Knebe A., Yepes G., Gottlöber S., Jiménez J. B., Maroto A. L., 2012, MNRAS, 424, 699
Cavaliere A., Fusco-Femiano R., 1976, A&A, 49, 137
Chiba T., De Felice A., Tsujikawa S., 2013, Phys. Rev. D, 87, 083505
Croston J. H., Pratt G. W., Böhringer H., Arnaud M., Pointecouteau E., Ponman T. J., Sanderson A. J. R., Temple R. F., Bower R. G., Donahue M., 2008, A&A, 487, 431
De Boni C., Dolag K., Ettori S., Moscardini L., Pettorino V., Baccigalupi C., 2011, MNRAS, 415, 2758
De Grandi S., Molendi S., 2002, ApJ, 567, 163
Doran M., 2005, JCAP, 10, 11
Ettori S., De Grandi S., Molendi S., 2002, A&A, 391, 841
Ettori S., Tozzi P., Borgani S., Rosati P., 2004, A&A, 417, 13
Evrard A. E., 1990, ApJ, 363, 349
Gill S. P. D., Knebe A., Gibson B. K., 2004, MNRAS, 351, 399
Giocoli C., Marulli F., Baldi M., Moscardini L., Metcalf R. B., 2013
He J.-H., Wang B., Abdalla E., Pavon D., 2010, JCAP, 12, 22
Hellwing W. A., Cautun M., Knebe A., Knollmann S., Juszkiewicz R., 2011, ArXiv e-prints
Jing Y. P., Suto Y., 2002, ApJ, 574, 538
Kaiser N., 1986, MNRAS, 222, 323
Knebe A., et al., 2013, ArXiv e-prints
Knollmann S. R., Knebe A., 2009, ApJS, 182, 608
Kravtsov A. V., Borgani S., 2012, ARA&A, 50, 353
Lau E. T., Kravtsov A. V., Nagai D., 2009, ApJ, 705, 1129
Leccardi A., Molendi S., 2008, A&A, 486, 359
Lee J., 2010
Li B., Barrow J. D., 2011, MNRAS, 413, 262
Macciò A. V., Dutton A. A., van den Bosch F. C., Moore B., Potter D., Stadel J., 2007, MNRAS, 378, 55
Macciò A. V., Quercellini C., Mainini R., Amendola L., Bonometto S. A., 2004, Phys. Rev. D, 69, 123516
Mainini R., 2005, Phys. Rev. D, 72, 083514
Mainini R., Bonometto S., 2006, Phys. Rev. D, 74, 043504
Mangano G., Miele G., Pettorino V., 2003, Modern Physics Letters A, 18, 831
Markevitch M., Forman W. R., Sarazin C. L., Vikhlinin A., 1998, ApJ, 503, 77
Mazzotta P., Rasia E., Moscardini L., Tormen G., 2004, MNRAS, 354, 10
Mroczkowski T., et al., 2009, ApJ, 694, 1034
Muanwong O., Kay S. T., Thomas P. A., 2006, ApJ, 649, 640
Nagai D., Vikhlinin A., Kravtsov A. V., 2007, ApJ, 655, 98
Navarro J. F., Frenk C. S., White S. D. M., 1995, MNRAS, 275, 720
Navarro J. F., Frenk C. S., White S. D. M., 1996, ApJ, 462, 563
Nusser A., Gubser S. S., Peebles P., 2005, Phys.Rev., D71, 083505
Pettorino V., Amendola L., Baccigalupi C., Quercellini C., 2012, Phys. Rev. D, 86, 103507
Planck Collaboration Ade P. A. R., Aghanim N., Arnaud M., Ashdown M., Atrio-Barandela F., Aumont J., Baccigalupi C., Balbi A., Banday A. J., et al., 2013, A&A, 550, A131
Prada F., Klypin A. A., Cuesta A. J., Betancort-Rijo J. E., Primack J., 2012, MNRAS, 423, 3018
Rasia E., Tormen G., Moscardini L., 2004, MNRAS, 351, 237
Ratra B., Peebles P. J. E., 1988, Phys. Rev. D, 37, 3406
Samushia L., Ratra B., 2008, ApJ, 680, L1
Sarazin C. L., 1986, Reviews of Modern Physics, 58, 1
Sembolini F., Yepes G., De Petris M., Gottlöber S., Lamagna L., Comis B., 2013, MNRAS, 429, 323
Springel V., 2005, MNRAS, 364, 1105
Springel V., Wang J., Vogelsberger M., Ludlow A., Jenkins A., Helmi A., Navarro J. F., Frenk C. S., White S. D. M., 2008, MNRAS, 391, 1685
Ventimiglia D. A., Voit G. M., Donahue M., Ameglio S., 2008, ApJ, 685, 118
Vikhlinin A., Forman W., Jones C., 1999, ApJ, 525, 47
Vikhlinin A., Kravtsov A., Forman W., Jones C., Markevitch M., Murray S. S., Van Speybroeck L., 2006, ApJ, 640, 691
Vikhlinin A., Markevitch M., Murray S. S., Jones C., Forman W., Van Speybroeck L., 2005, ApJ, 628, 655
Wang P.-Y., Chen C.-W., Chen P., 2012, JCAP, 2, 16
Wetterich C., 1995, A&A, 301, 321
Zlatev I., Wang L., Steinhardt P. J., 1999, Physical Review Letters, 82, 896

This paper has been typeset from a TEX/ LATEX file prepared by the author.